Volume 1, Number 2, December 2017

SCIENCE & DEVELOPMENT

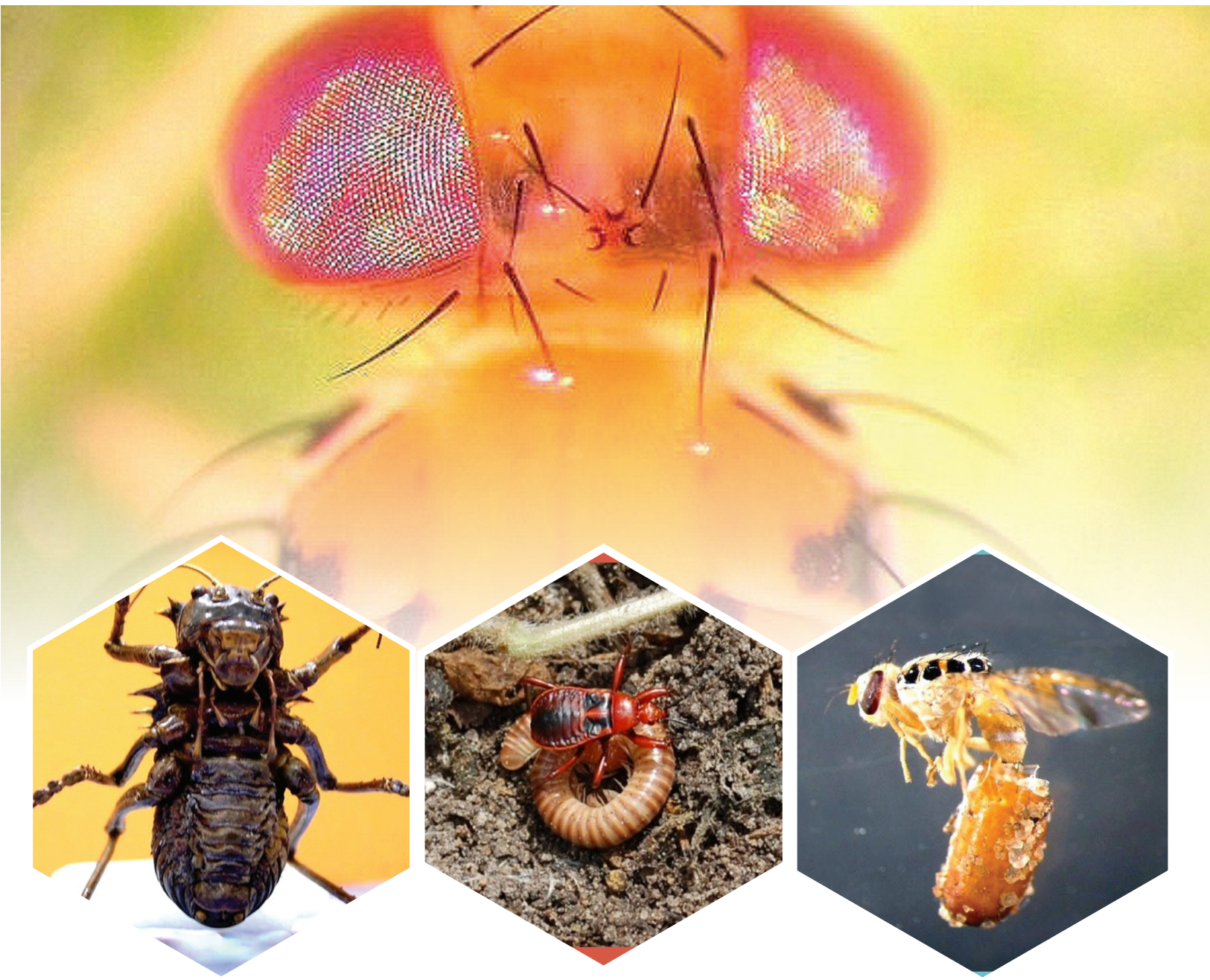

CBAS
College of Basic and Applied Sciences

A Journal of the College of Basic and Applied Sciences (CBAS), University of Ghana

Science and Development

CBAS
College of Basic and Applied Science

ISSN: 2550-3421

Email for Correspondence:

cbas-sdp@ug.edu.gh

Acknowledgement
This issue of the Science and Development Journal was produced with financial support from the Carnegie Corporation of New York through the University of Ghana Building A New Generation of Academics in Africa (BANGA-Africa) Project.

Printed by Digibooks Ghana Ltd.

Published by
College of Basic and Applied Sciences (CBAS)
University of Ghana

Morphometric Studies of the Sweet Potato Weevil, *Cylas* Species-Complex in Southern Ghana

Maxwell K. Billah[1,2*], Ayaovi Agbessenou[1], David D. Wilson[2], Wouter Dekoninck[3] and Carl Vangestel[3]

[1]African Regional Postgraduate Program in Insect Science (ARPPIS), University of Ghana, Accra, Ghana
[2]Department of Animal Biology and Conservation Science (DABCS), University of Ghana, Accra, Ghana
[3]Royal Belgian Institute for Natural Sciences, Brussels, Belgium
***Corresponding author:** mxbillah@gmail.com

ABSTRACT

The Sweet potato weevil, *Cylas* species, is a key pest of sweet potato, and widely distributed on the African continent. The management of the pest is limited because its taxonomic status is not clear. Populations of the same species occupying distinct localities experience different ecological and climatic pressures that might result in differentiation in traits. This study sought to identify and compare body sizes of *Cylas* species from four regions in southern Ghana – Central, Eastern, Greater Accra and Volta. Of the 6,686 samples collected from the four regions, two species were identified: *Cylas brunneus* Fabricius, and *Cylas puncticollis* Boheman. Twelve morphometric characters were examined and measured, of which four traits - elytra and rostrum lengths, pronotum and head widths contributed most to the variations observed. In *C. puncticollis*, individuals with the longest body were recorded in Greater Accra Region (7.084 ± 0.089 mm), while those in the Central Region had the smallest body size (6.786 ± 0.086 mm). Our findings suggest that distinct localities may influence changes in body size.

Keywords: Sweet potato, *Cylas brunneus, C. puncticollis,* morphometric studies, southern Ghana

Introduction

Sweet potato is one of the world's most important food crops in terms of human consumption, particularly in Sub-Saharan Africa, parts of Asia, and the Pacific Islands. First domesticated more than 5,000 years ago in Latin America, it is grown in more developing countries than any other root crop (Smit, 1997). In Sub-Saharan Africa, sweet potato is predominantly cultivated on small plots characterized by low fertility and drought-prone soils, producing relatively good yields with low inputs and minimal labour costs (Ewell and Mutuura, 1994). Historically, the production of roots and tubers in Africa has been restricted to assuring food security. The production of roots and tubers in developing countries is projected to increase by 58% (232 million tonnes) to 635 million tonnes between 2003 and 2020 (Bill and Melinda Gates Foundation, 2011).

The crop has recently become the focus of targeted bio-fortification for enhanced vitamin A. The Orange-fleshed varieties have been bred with 50-fold more ß-carotene than standard varieties, and these newly released varieties rank first among roots and tubers in Sub-Saharan Africa for their nutritional quality (Low *et al*., 2007; Low, 2013). Given its adaptability, low-external input requirements, nutritional quality, and improvement potential, it is not surprising that sweet potato has become a priority in crop-based strategies for enhancing food security in the tropics (Pfeiffer & McClafferty, 2007; Bill and Melinda Gates Foundation, 2011; Bouis and Islam, 2012).

Notable among the production constraints of sweet potatoes is the issue of insects, with the Sweet potato weevil as the main pest. With the different species

involved and their distribution in different habitats, the true identity of the pests needs to be ascertained, as it is of crucial essence in the development of strategies for their management. The identification process is usually exacerbated by variations in the morphology of the pest.

Variation is a natural feature of any morphological character (Plavcan, 2012). Populations of the same species inhabiting distinct localities can experience different ecological and climatic conditions, giving rise to variation in one or more traits (Bulgarella *et al.*, 2015). Size variations provide significant clues about the taxonomy, morphology, behaviour, and life history of species, yet they are also a major source of difficulty when attempting to establish species limits within a genus.

Cylas weevils are key pests of sweet potato worldwide, especially in drier agro-ecological zones. Nine species within the genus *Cylas* have been identified as pests that attack sweet potato and are placed in three species groups: *Cylas brunneus* Fabricius,1797, *Cylas puncticollis* Boheman, 1833, and *Cylas formicarius* (Fabricius, 1798) (Wolfe, 1991). The distribution of *Cylas* species varies between regions -*C. formicarius* is the most widespread, while *C. puncticollis* and *C. brunneus* are confined to Africa (Wolfe, 1991). In southern Ghana, *C. puncticollis* and *C. brunneus* co-occur geographically in sympatry, and previous studies on the genus *Cylas* revealed multiple sympatric species feeding on a single variety of *Ipomoea* (Agbessenou *et al.*, 2016). The fact that distinct species do occur in sympatry in southern Ghana is a good pointer to the potential problem of species identification in the field.

Wolfe (1991) proposed a taxonomic key to separate these three species groups. However, the most difficult systematic problems in *Cylas* involve the identification of members of each group. *Cylas puncticollis* is the most problematic species within the *C. puncticollis* species group, and some populations currently assigned to the *C. puncticollis* group may represent undescribed morphologically-similar cryptic species (Wolfe, 1991). Generally, cryptic species interfere with the recognition of taxonomic diversity and obscure levels of intra-specific variation. In addition, much attention has been focused on inter-specific patterns of variation, while intra-specific variation in *Cylas* species is unexplored. Many techniques have been used to explore intra-specific variation, with morphometrics being one of them. In this study, a within-group comparative method was applied to the taxonomy of the different populations of the genus *Cylas* sampled from different habitats, with the aim of comparing body size of adult weevils.

Methods

Field sites, sampling procedure and collection of *Cylas* spp.

The survey was conducted during the 2015 cropping season from July to December in the four leading sweet potato production regions in southern Ghana (Bidzakin *et al.*, 2014) -the Central, Eastern, Greater Accra and Volta regions (Table 1).

In the regions, potato farms of at least 0.5 acres were selected from at least two districts for the study. Sampling was carried out when crops were about three months old and ready for harvesting. This was based on the methodology reported by McSorley and Jansson (1991), with some modifications - where each field was divided into four parts (4 quadrants) and a total of 10 infested plant stands or hills selected in each quadrant. Vines and roots with signs of external feeding, oviposition punctures and damage were collected and placed in medium-sized (12 x 15 cm) grocery bags or envelopes, and transported to the laboratory.

Table 1: List of localities (with GPS coordinates) in the 4 regions where samples were collected.

Region	District	Agro-eco zone	Community	Lat	Long	Alt (m)	Weevils
Volta	Ohawu	Coastal Savannah	Bedjame	05° 39′ 17 N	00° 11′ 04 W	113	340
		Coastal Savannah	Kpotavi	06° 11′ 19 N	00° 50′ 58 E	63	1338
	Akatsi South	Coastal Savannah	Tadzevu	06° 07′ 35 N	00° 48′ 13 E	55	134
		Coastal Savannah	Awalavi	06° 07′ 35 N	00° 48′ 13 E	55	640
		Coastal Savannah	Ative	06° 07′ 35 N	00° 48′ 13 E	55	665
Central	Komenda Edna Eguafo Abirem	Coastal Savannah	Komenda	05° 04′ 14 N	00° 14′ 31 W	16	880
	Cape Coast	Coastal Savannah	Mpaesem	05° 07′ 17 N	01° 16′ 06 W	18	567
Eastern	Ayensuano	Semi-Deciduous Forest	Marfo	05° 51′ 91 N	00° 26′ 78 W	155	651
	Begoro	Semi-Deciduous Forest	Ehiamakyene	06° 23′ 29 N	00° 22′ 46 W	470	76
	Upper Manya	Semi-Deciduous Forest	Poponyafantem	06° 06′ 06 N	00° 00′ 57 W	98	310
	Kwahu East	Semi-Deciduous Forest	Akwasiho	06° 32′ 18 N	00° 45′ 19 W	260	105
Greater-Accra	Accra Municipality	Coastal Savannah	University Farm	05° 10′ 21 N	01° 17′ 49 W	76	655
	Ga-West	Coastal Savannah	Manchie	05° 45′ 57 N	00° 00′ 57 W	67	325

Sweet potato root incubation and adult collection

Field samples were incubated in rearing boxes (17 x 17 x 9.5 cm) and held till pupae and/or adult emergence in the laboratories of the African Regional Postgraduate Programme in Insect Science (ARPPIS), University of Ghana (Plate 1). Set ups were monitored for development of pupae and/or adults. Pupae were collected from rearing boxes and kept in small boxes until adults emerged. After emergence, weevils were allowed to feed for 5 days on freshly-introduced sweet potato roots for full adult development and to attain full body colouration. At maturity, weevils were killed by freezing, and samples preserved in vials containing 70% alcohol.

A)  B) 

Plate 1: Incubation set up for collecting sweet potato weevils, A = incubation boxes with samples from the field, and B = split sweet potato roots in an incubation box

Insect identification

Identification was made with a Leica EZ4 D stereo microscope based on the morphological characteristics of the collected specimens. Voucher specimens were deposited at ARPPIS-UG and the Royal Belgian Institute of Natural Sciences (RBINS) in Brussels, Belgium.

Morphometric measurements

The procedure followed the general processes of slide preparation of Billah *et al.* (2005; 2008). Field collected samples were dissected using a Leica EZ4D Stereomicroscope. Imaging of mounted specimens was done using video microscopy – the Leica EZ4D Stereomicroscope fitted with an inbuilt camera and connected to a laptop. Body parts were measured using the Leica Application Software (Version 2.1). They included body length (*bl*); elytra length (*el*); elytra width (*ew*); elytra width at base (*ewb*); elytra width at apex (*ewa*); head length (*hl*); head width (*hw*); rostrum length (*rl*); pronotum length (*pl*); pronotum width (*pw*); pronotum width at apex (*pwa*); and pronotum width at base (*pwb*) (Figure 1).

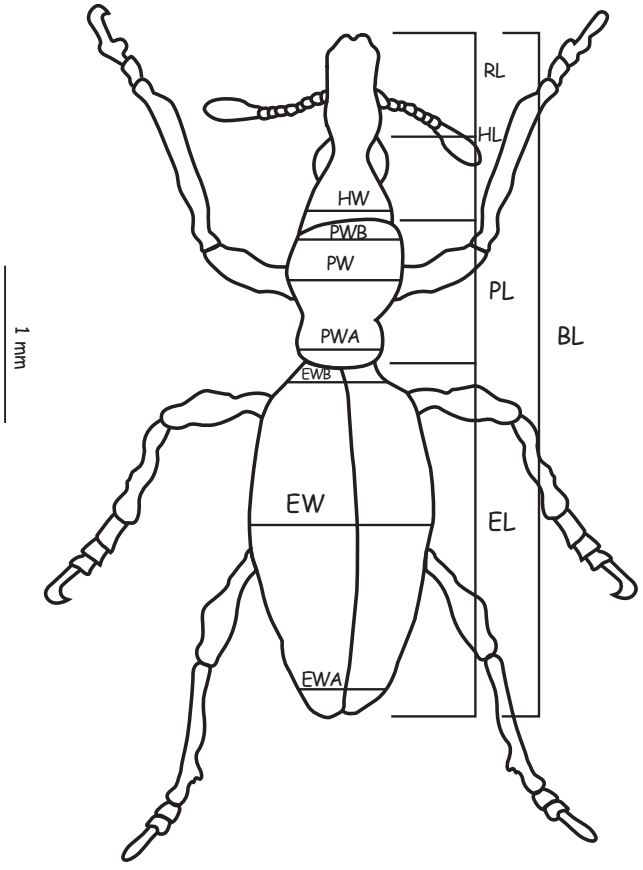

Fig. 1: Drawing of adult sweet potato weevil showing linear measurements of the 12 variables taken for morphometric analyses - body length (*bl*), elytra length (*el*), elytra width (*ew*), elytra width at base (*ewb*), elytra width at apex (*ewa*), head length (*hl*), head width (*hw*), rostrum length (*rl*), pronotum length (*pl*), pronotum width (*pw*), pronotum width at apex (*pwa*), and pronotum width at base (*pwb*)

Data analyses

All morphometric analyses were performed using Statistical Analysis System software version 8.2 (SAS Institute Inc., 2003). When ANOVAs were significant (P = 0.05), means were separated using the Student-Newman-Keuls (SNK) test. Multivariate statistical analyses, i.e. analysis of variance, principal components analysis and canonical analysis, were used to detect any possible variations (Kimani-Njoku *et al.*, 2001; Billah *et al.*, 2005; 2008). Principal Component Analysis (PCA) and Canonical Variate Analysis (CVA) were performed in the variance-covariance matrix of the 12 variables measured on the weevil populations. Mahalanobis squared distances (D^2) between the various populations were obtained as a measure of the relatedness between the populations based on means, variances and covariances.

Results

Two species were identified from the field materials – *C. puncticollis* and *C. brunneus* (Plate 2). Preliminary analyses of the data showed differences in the body sizes of male and female individuals of the same species (results not shown here), with the females being slightly bigger than the males. Based on this observation, all further analyses were conducted on same-sex basis.

Males of C. puncticollis

Table 2 shows mean linear measurements of males of *C. puncticollis* populations from the four regions. Among the measurements, elytra width at the base (*ewb*) and pronotum width at the apex (*pwa*) were two variables which showed significant differences big enough (P = 0.0002 and P < 0.0001, respectively) to separate the populations into three clusters. With *ewb*, individuals from the Central Region were shown to have the largest values, followed by those from the Eastern and Volta (which did not differ from each other), and Greater Accra had the smallest base elytra width. With pronotum width at the apex, the largest values were from the Eastern, followed by Central and Volta regions (which did not also differ from each other); the least were from Greater Accra. Five other variables, *bl, ewa, pl, pw* and *pwb,* could only separate the populations into two clusters, while the last five variables showed no significant differences in variation.

A) 

B) 

Plate 2: General habitus of adult sweet potato weevils. A) *Cylas puncticollis* (female) and B) *Cylas brunneus* (female). (Photos: Camille Locatelli, RBINS, Belgium)

Projection of the dataset of body measurements on the first two principal axes showed incomplete separation of the four populations, with the first two components accounting for 59.4% (PC1 = 36.8% + PC2 = 22.6%) of the total size variation (Fig. 2A). However, projection of the dataset on the first two canonical axes showed a much better separation trend between weevil populations, accounting for 90.2% (CV 1= 55.9% + CV 2 = 34.3%) of the variation (Fig. 2B). Clusters representing the population from the Greater-Accra, Central and Eastern regions were clearly separated, while the population from the Volta Region was only separated from that of the Central Region, but was found lying between the Greater Accra and Eastern Region populations. This separation pattern is in line with the outcome of the Mahalanobis squared distances (Table 6), where the largest separation value (D^2 = 7.28) was between populations of the Greater Accra and the Central regions, with those of the Eastern and Volta regions lying between the two. The smallest distance of D^2 = 3.00 was between populations of the Greater Accra and Volta regions (indicating the level of relatedness of the two populations), and thus corroborating the clustering seen in Fig 2B (Table 6A).

Table 2: Linear measurement (± SE) comparison of male populations of *C. puncticollis* from four regions (Central, Eastern, Greater Accra, and Volta)

Region	Mean linear measurements (mm) (± SE)											
	*bl	el	ew	ewb	ewa	hl	hw	Rl	pl	pw	pwa	pwb
Central	6.690 ± 0.082 b (10)	3.452 ± 0.036 a (10)	1.592 ± 0.019 a (10)	0.656 ± 0.016 a (10)	0.468 ± 0.019 a (10)	0.894 ± 0.017 a (10)	0.778 ± 0.008 a (10)	1.064 ± 0.023 a (10)	1.154 ± 0.015 b (10)	0.922 ± 0.012 b (10)	0.638 ± 0.014 b (10)	0.826 ± 0.009 b (10)
Eastern	6.900 ± 0.072 a (14)	3.497 ± 0.052 a (14)	1.586 ± 0.021 a (14)	0.617 ± 0.012 b (14)	0.420 ± 0.011 b (14)	0.887 ± 0.015 a (14)	0.777 ± 0.011 a (14)	1.071 ± 0.019 a (14)	1.196 ± 0.011 b (14)	0.950 ± 0.010 ab (14)	0.714 ± 0.010 a (14)	0.854 ± 0.009 a (14)
Greater Accra	6.929 ± 0.089 a (7)	3.571 ± 0.063 a (7)	1.583 ± 0.029 a (7)	0.554 ± 0.016 c (7)	0.400 ± 0.000 b (7)	0.886 ± 0.010 a (7)	0.783 ± 0.013 a (7)	1.079 ± 0.023 a (7)	1.263 ± 0.018 a (7)	0.966 ± 0.011 a (7)	0.589 ± 0.011 c (7)	0.857 ± 0.013 a (7)
Volta	6.664 ± 0.056 b (14)	3.411 ± 0.034 a (14)	1.537 ± 0.012 a (14)	0.600 ± 0.007 b (14)	0.397 ± 0.003 b (14)	0.897 ± 0.011 a (14)	0.763 ± 0.009 a (14)	1.054 ± 0.014 a (14)	1.187 ± 0.016 b (14)	0.919 ± 0.070 b (14)	0.630 ± 0.011 b (14)	0.825 ± 0.008 b (14)
F	3.47	1.85	1.87	8.60	7.75	0.14	0.72	0.30	6.59	3.84	19.60	3.17
Df	3, 41	3, 41	3, 41	3, 41	3, 41	3, 41	3, 41	3, 41	3, 41	3, 41	3, 41	3, 41
P	0.0245	0.1531	0.1504	0.0002	0.0003	0.9334	0.5478	0.8269	0.0010	0.0165	< 0.0001	0.0341

Means in the same column followed by different letters are significantly different (P = 0.05), using Student-Newman-Keuls (SNK) test, while those in same column with different letters together are not significantly different from each other. Figures in parentheses are numbers of replicates.

*bl-body length; el-elytra length; ew-elytra width; ewb-elytra width at base; ewa-elytra width at apex; hl-head length; hw-head width; rl-rostrum length; pl-pronotum length; pw-pronotum width; pwa-pronotum width at apex; pwb-pronotum width at base

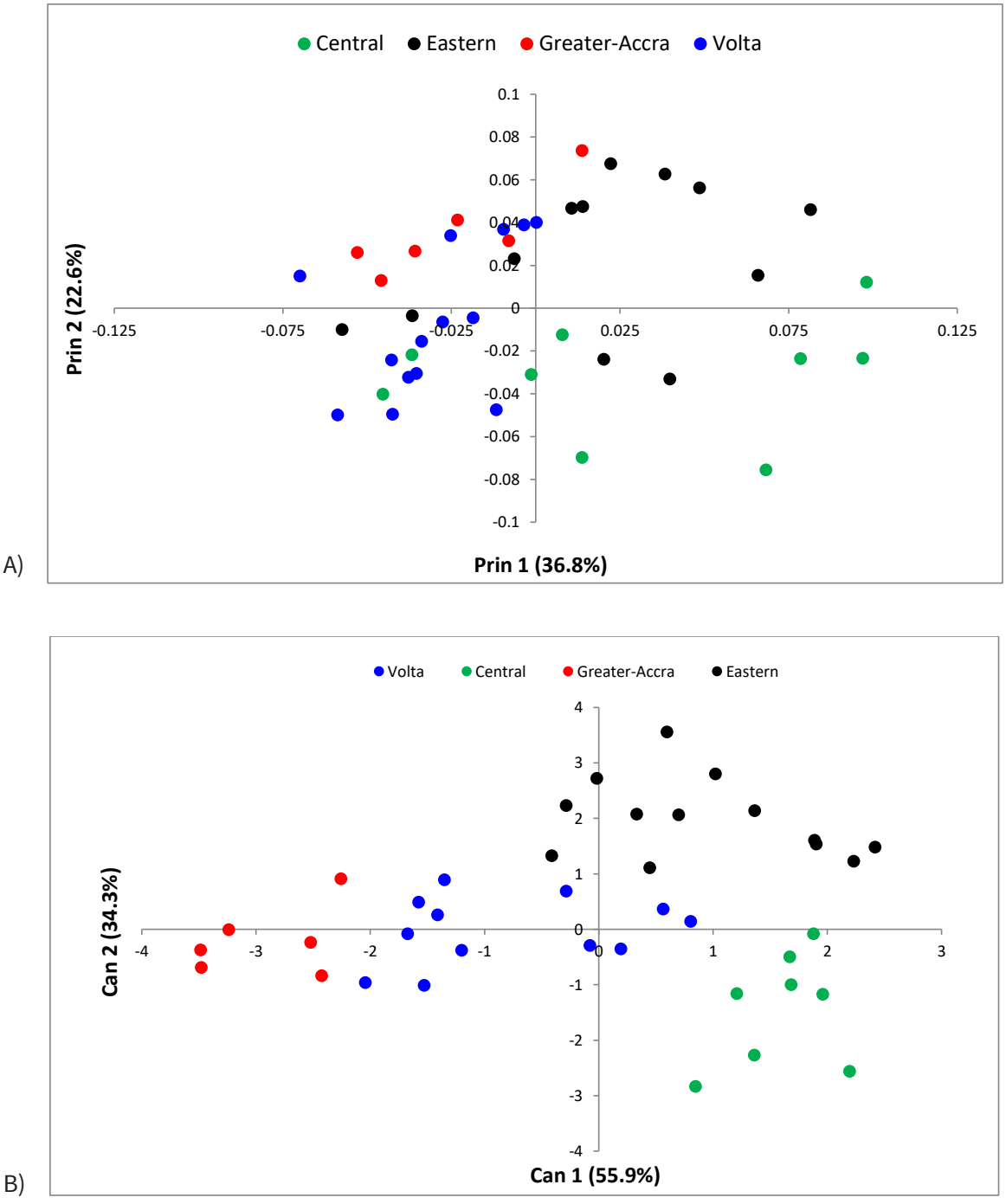

Fig. 2: Projection of linear body measurement dataset of male individuals of *Cylas puncticollis.* A) First two principal components, B) First two canonical variates.

Females of C. puncticollis

The only variable that could tell differences in the population was *pwa*, which put them in three clusters, while four other variables (*el, hw, rl* and *pwb*) could separate them into two clusters (Table 3). Projection of the dataset on the first two principal component axes produced a fuzzy separation of the populations, accounting for 64.8% (PC 1 = 44.0% + PC 2 = 20.8%) of the variation (Fig 3A). However, when the dataset was projected on the first two canonical axes, variation as high as 90.6% (CV 1= 74.3% + CV 2 = 16.3%) was accounted for, thus separating the populations into three clusters – Eastern, Greater Accra and Volta, with individuals from the Central Region lying between, and not clearly separated from the others (Fig 3B). Values in Table 6A show the most distant groups as the Greater Accra and Eastern populations (D^2 = 6.14), followed by the Volta and Eastern (D^2 = 3.36). The smallest value (and the most closely related) was between populations from the Volta and Central regions (D^2 = 1.43; Table 6A).

Table 3. Linear measurement (± SE) comparison of female populations of *C. puncticollis* from four regions (Central, Eastern, Greater Accra, and Volta).

Region	Mean linear measurements (mm) (± SE)											
	*bl	El	Ew	ewb	ewa	hl	hw	rl	pl	pw	pwa	pwb
Central	6.810 ± 0.156 b (10)	3.472 ± 0.063 b (10)	1.584 ± 0.027 a (10)	0.624 ± 0.026 a (10)	0.408 ± 0.014 a (10)	0.690 ± 0.016 a (10)	0.804 ± 0.014 b (10)	1.211 ± 0.039 b (10)	1.290 ± 0.032 b (10)	1.028 ± 0.025 a (10)	0.666 ± 0.013 b (10)	0.864 ± 0.013 b (10)
Eastern	7.092 ± 0.092 ab (13)	3.594 ± 0.046 ab (13)	1.585 ± 0.033 a (13)	0.615 ± 0.010 a (13)	0.415 ± 0.010 a (13)	0.720 ± 0.011 a (13)	0.826 ± 0.010 b (13)	1.302 ± 0.020 a (13)	1.318 ± 0.025 ab (13)	1.020 ± 0.017 a (13)	0.712 ± 0.015 a (13)	0.903 ± 0.010 ab (13)
Greater Accra	7.267 ± 0.133 a (6)	3.740 ± 0.063 a (6)	1.667 ± 0.027 a (6)	0.600 ± 0.000 a (6)	0.393 ± 0.007 a (6)	0.710 ± 0.013 a (6)	0.870 ± 0.015 a (6)	1.295 ± 0.019 a (6)	1.403 ± 0.034 a (6)	1.073 ± 0.028 a (6)	0.603 ± 0.013 c (6)	0.923 ± 0.025 a (6)
Volta	6.960 ± 0.072 ab (10)	3.520 ± 0.040 b (10)	1.576 ± 0.019 a (10)	0.584 ± 0.015 a (10)	0.400 ± 0.000 a (10)	0.708 ± 0.015 a (10)	0.816 ± 0.008 b (10)	1.230 ± 0.012 b (10)	1.342 ± 0.018 ab (10)	1.012 ± 0.012 a (10)	0.638 ± 0.010 bc (10)	0.878 ± 0.015 ab (10)
F	2.346	3.718	1.458	1.143	0.850	0.911	4.316	3.057	2.362	1.310	10.600	2.784
Df	3, 35	3, 35	3, 35	3, 35	3, 35	3, 35	3, 35	3, 35	3, 35	3, 35	3, 35	3, 35
P	0.090	0.020	0.243	0.345	0.476	0.446	0.011	0.041	0.088	0.287	< 0.0001	0.055

Means in the same column followed by different letters are significantly different (P = 0.05), using Student-Newman-Keuls (SNK) test, while those in same column with different letters together are not significantly different from each other. Figures in parentheses are numbers of replicates.

*bl-body length; el-elytra length; ew-elytra width; ewb-elytra width at base; ewa-elytra width at apex; hl-head length; hw-head width; rl-rostrum length; pl-pronotum length; pw-pronotum width; pwa-pronotum width at apex; pwb-pronotum width at base

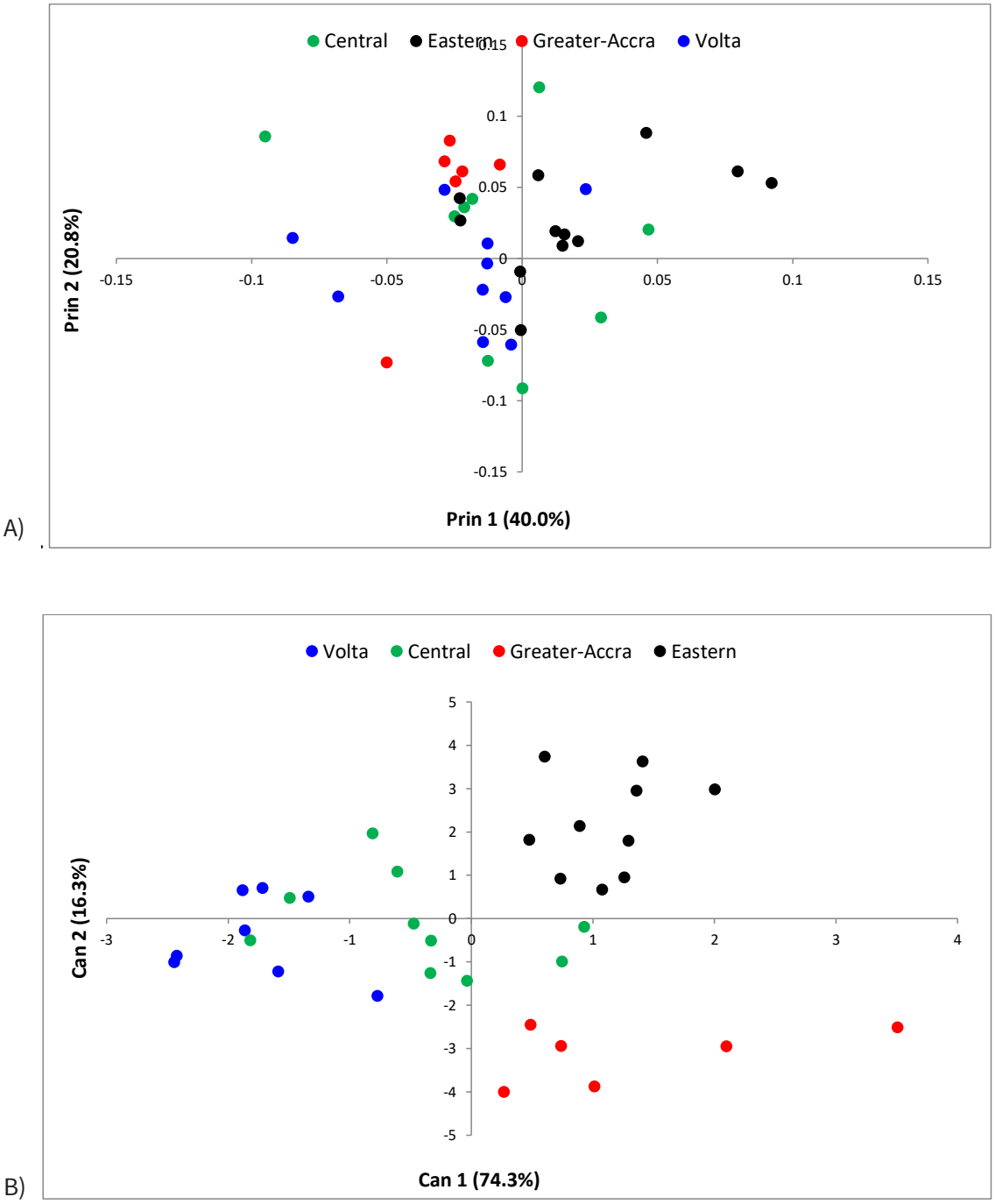

Fig. 3: Projection of linear body measurement dataset of female individuals of *Cylas puncticollis.* A) First two principal components, B) First two canonical variates

Males of C. brunneus

Table 4 shows that only variables *ewa* and *hl* had significant differences that could separate the populations into three groups, while *ewb, rl, pwa* and *pwb* could only identify them as two groups. Projection of the data on the first two principal component and canonical variate axes shows 66.0% (PC 1 = 38.5% + PC 2 = 27.5%) and 91.1% (CV 1 = 70.1% + 21.0%) of variations being accounted for in Figs. 4A and 4B, respectively. The canonical plot (Fig. 4B) shows populations from the Eastern, Greater Accra and Central regions almost in different quadrants, with those of the Volta Region lying in the middle. However, the largest distance between the centroids of the clusters was seen in populations of the Eastern and Central regions ($D^2 = 4.97$), followed by $D^2 = 4.44$ between the Greater Accra and Central regions. The closest was between the Greater Accra and Eastern regions ($D^2 = 1.60$), followed by $D^2 = 1.62$ between the Greater Accra and Volta regions (Table 6B).

Table 4: Linear measurement (± SE) comparison of male populations of *C. brunneus* from four regions (Central, Eastern, Greater Accra, and Volta).

Region	Mean linear measurements (mm) (± SE)											
	*bl	el	Ew	ewb	ewa	hl	hw	rl	pl	pw	pwa	pwb
Central	5.583 ± 0.065 a (6)	2.893 ± 0.041 a (6)	1.273 ± 0.022 a (6)	0.527 ± 0.028 a (6)	0.427 ± 0.013 a (6)	0.840 ± 0.023 a (6)	0.613 ± 0.012 a (6)	0.738 ± 0.013 b (6)	1.017 ± 0.012 b (6)	0.777 ± 0.012 a (6)	0.453 ± 0.012 b (6)	0.650 ± 0.015 ab (6)
Eastern	5.653 ± 0.054 a (15)	2.888 ± 0.023 a (15)	1.245 ± 0.016 a (15)	0.483 ± 0.011 ab (15)	0.355 ± 0.008 c (15)	0.728 ± 0.014 c (15)	0.617 ± 0.006 a (15)	0.803 ± 0.013 a (15)	1.091 ± 0.016 a (15)	0.789 ± 0.009 a (15)	0.507 ± 0.018 a (15)	0.667 ± 0.006 a (15)
Greater Accra	5.500 ± 0.082 a (10)	2.796 ± 0.050 a (10)	1.212 ± 0.023 a (10)	0.448 ± 0.009 b (10)	0.352 ± 0.005 c (10)	0.750 ± 0.017 bc (10)	0.598 ± 0.010 a (10)	0.781 ± 0.014 a (10)	1.066 ± 0.020 ab (10)	0.770 ± 0.017 a (10)	0.466 ± 0.009 b (10)	0.634 ± 0.010 b (10)
Volta	5.700 ± 0.049 a (15)	2.915 ± 0.029 a (15)	1.261 ± 0.010 a (15)	0.469 ± 0.009 a (15)	0.389 ± 0.005 b (15)	0.793 ± 0.012 ab (15)	0.615 ± 0.005 a (15)	0.798 ± 0.012 a (15)	1.075 ± 0.012 ab (15)	0.793 ± 0.008 a (15)	0.507 ± 0.006 a (15)	0.656 ± 0.005 ab (15)
F	1.974	2.242	1.978	5.060	17.157	8.450	1.392	3.098	2.607	0.904	3.617	3.049
Df	3, 42	3, 42	3, 42	3, 42	3, 42	3, 42	3, 42	3, 42	3, 42	3, 42	3, 42	3, 42
P	0.133	0.097	0.132	0.004	< 0.0001	< 0.0001	0.259	0.037	0.064	0.447	0.021	0.039

Means in the same column followed by different letters are significantly different (P = 0.05), using Student-Newman-Keuls (SNK) test, while those in same column with different letters together are not significantly different from each other. Figures in parentheses are numbers of replicates.

*bl-body length; el-elytra length; ew-elytra width; ewb-elytra width at base; ewa-elytra width at apex; hl-head length; hw-head width; rl-rostrum length; pl-pronotum length; pw-pronotum width; pwa-pronotum width at apex; pwb-pronotum width at base

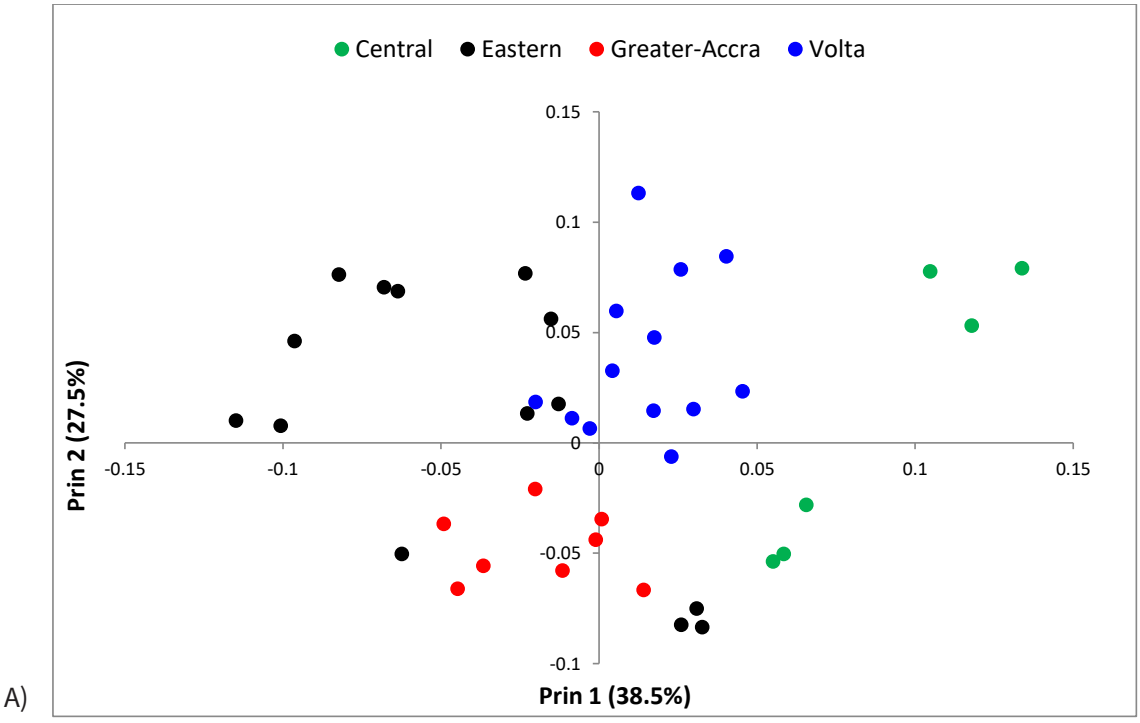

A)

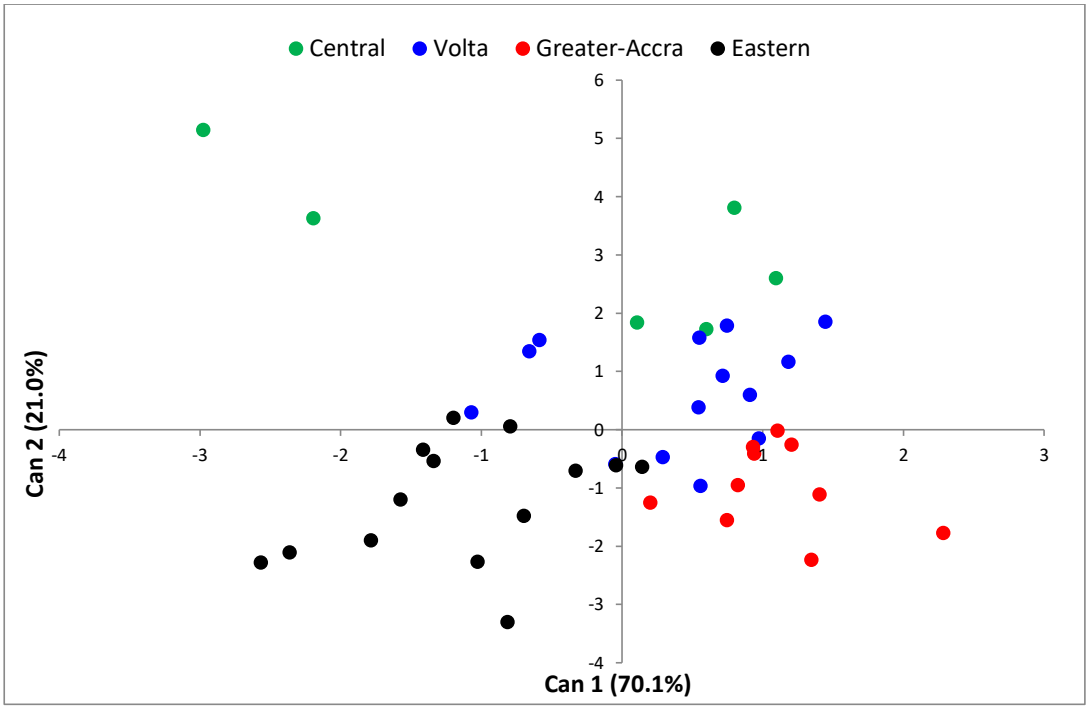

B)

Fig. 4: Projection of linear body measurement dataset of male individuals of *Cylas brunneus.* A) First two principal components, B) First two canonical variates

4.4. Females of C. brunneus

In this group, only two of the 12 variables made a significant difference - elytra width at apex (*ewa*) and pronotum width at apex (*pwa*) (Table 5). Elytra width at apex showed populations from Central and Volta being significantly different from those from the Eastern and Greater Accra regions. Based on *pwa,* populations from the Eastern and Central regions are significantly different from each other, but not any different from those of the Greater Accra and Volta regions (Table 5). With the close nature of the group, projection of the dataset on the first two principal component axes did not show much separation, accounting for only 60.5% (PC 1 = 36.4% + PC 2 = 24.1%) of the variation (Fig 5A). Projection on the first two canonical axes accounted for 90.6% (CV 1 = 74.3% + 16.3%) of the variation observed in the two variables – *ewa* and *pwa* (Fig 5B).Mahalanobis squared distance (D^2 = 4.23) was largest between Eastern and Volta, followed by that between Eastern and Central (D^2 = 4.11). The most closely related populations were Volta and Central (D^2 =1.35), followed by Volta and Greater Accra (D^2 =1.47) (Table 6B).

Table 5: Linear measurement (± SE) comparison of female populations of *C. brunneus* from four regions (Central, Eastern, Greater Accra and Volta)

Region	Mean linear measurements (mm) (± SE)											
	*bl	El	ew	ewb	ewa	hl	hw	rl	pl	pw	pwa	pwb
Central	5.520 ± 0.107 a (5)	2.896 ± 0.041 a (5)	1.280 ± 0.013 a (5)	0.512 ± 0.015 a (5)	0.400 ± 0.000 a (5)	0.680 ± 0.011 a (5)	0.636 ± 0.009 a (5)	0.817 ± 0.019 a (5)	1.148 ± 0.027 a (5)	0.844 ± 0.009 a (5)	0.444 ± 0.018 b (5)	0.692 ± 0.008 a (5)
Eastern	5.664 ± 0.072 a (11)	2.902 ± 0.035 a (11)	1.269 ± 0.014 a (11)	0.476 ± 0.014 a (11)	0.349 ± 0.008 b (11)	0.655 ± 0.012 a (11)	0.636 ± 0.008 a (11)	0.856 ± 0.008 a (11)	1.189 ± 0.012 a (11)	0.840 ± 0.010 a (11)	0.529 ± 0.021 a (11)	0.691 ± 0.009 a (11)
Greater Accra	5.511 ± 0.096 a (9)	2.809 ± 0.058 a (9)	1.249 ± 0.033 a (9)	0.467 ± 0.009 a (9)	0.360 ± 0.009 b (9)	0.667 ± 0.011 a (9)	0.629 ± 0.008 a (9)	0.841 ± 0.015 a (9)	1.153 ± 0.021 a (9)	0.822 ± 0.017 a (9)	0.482 ± 0.017 ab (9)	0.676 ± 0.008 a (9)
Volta	5.593 ± 0.07 a (15)	2.883 ± 0.028 a (15)	1.251 ± 0.012 a (15)	0.501 ± 0.009 a (15)	0.395 ± 0.007 a (15)	0.677 ± 0.007 a (15)	0.624 ± 0.005 a (15)	0.834 ± 0.009 a (15)	1.163 ± 0.014 a (15)	0820 ± 0.007 a (15)	0.497 ± 0.008 ab (15)	0.669 ± 0.007 a (15)
F	0.671	1.038	0.480	2.655	9.883	1.224	0.820	1.369	1.035	1.138	3.720	1.978
Df	3, 36	3, 36	3, 36	3, 36	3, 36	3, 36	3, 36	3, 36	3, 36	3, 36	3, 36	3, 36
P	0.575	0.387	0.698	0.063	< 0.0001	0.315	0.492	0.268	0.389	0.347	0.020	0.135

Means in the same column followed by different letters are significantly different (P = 0.05), using Student-Newman-Keuls (SNK) test, while those in same column with different letters together are not significantly different from each other. Figures in parentheses are numbers of replicates

*bl-body length; el-elytra length; ew-elytra width; ewb-elytra width at base; ewa-elytra width at apex; hl-head length; hw-head width; rl-rostrum length; pl-pronotum length; pw-pronotum width; pwa-pronotum width at apex; pwb-pronotum width at base

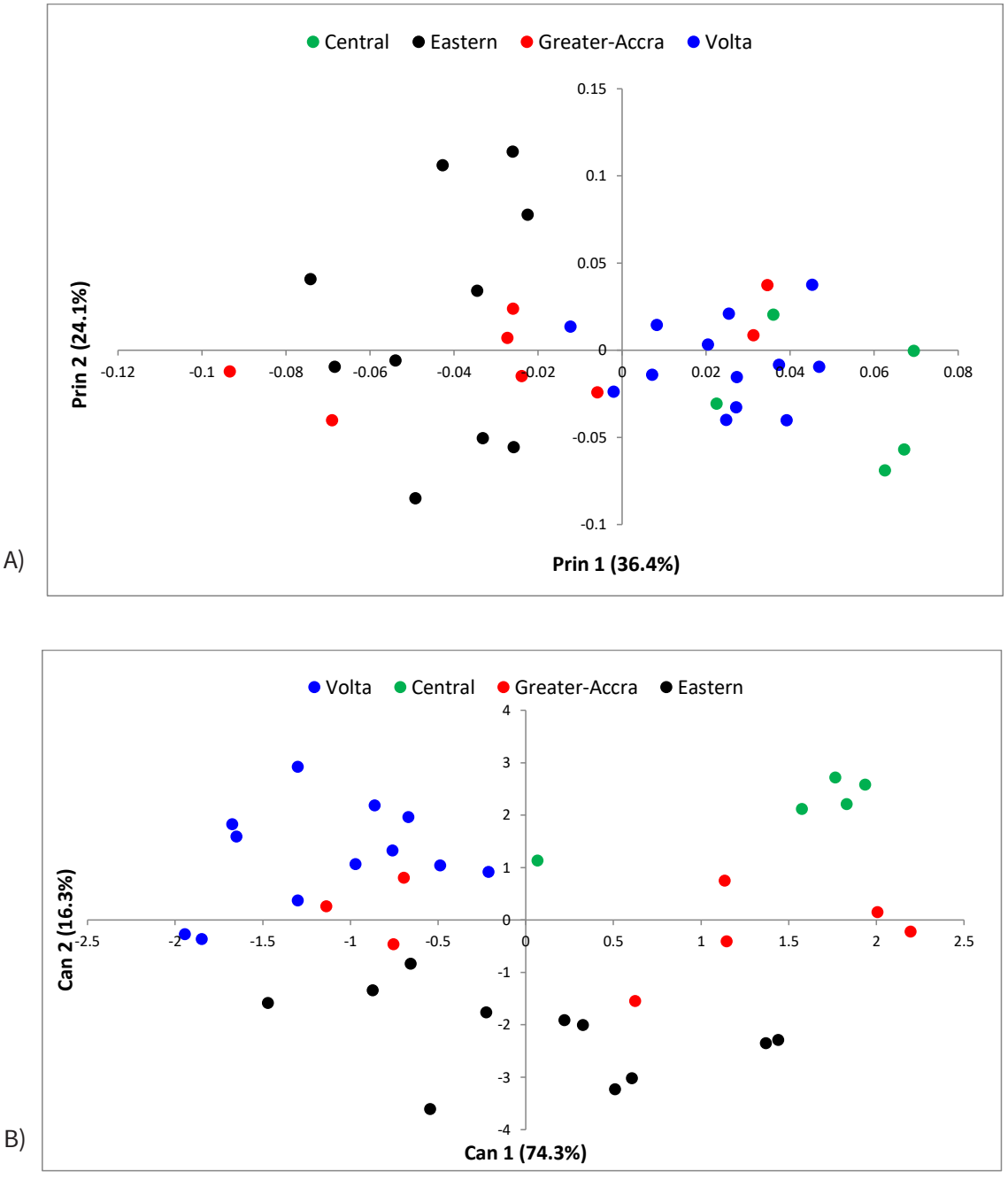

Fig. 5: Projection of linear body measurement dataset of female individuals of *Cylas brunneus.* A) First two principal components, B) First two canonical variates

Table 6. Mahalanobis squared distances (D^2) between sweet potato weevil populations from the four regions (Central, Eastern, Greater Accra and Volta). A = *Cylas puncticollis* **(male and female), and B =** *Cylas brunneus* **(male and female).**

A)

Region	Central	Eastern	Greater Accra	Volta
		Males		
Central	0			
Eastern	4.92	0		
Greater Accra	7.28	6.35	0	
Volta	3.84	3.50	3.00	0
		Females		
Central	0			
Eastern	2.60	0		
Greater Accra	3.06	6.14	0	
Volta	1.43	3.36	3.02	0

B)

Region	Central	Eastern	Greater Accra	Volta
		Males		
Central	0			
Eastern	4.97	0		
Greater Accra	4.44	1.60	0	
Volta	2.33	2.34	1.62	0
		Females		
Central	0			
Eastern	4.11	0		
Greater Accra	1.78	1.55	0	
Volta	1.35	4.23	1.47	0

Discussion

This study has expanded our appreciation of size variation in both *C. puncticollis* and *C. brunneus* and provided us solid information about geographical size variation in both species. Traditional morphometrics represents one of the most commonly used ways of investigating intra- and inter- specific body size variation among organisms within a given population (Rohlf & Bookstein, 1990; Umphrey, 1996; Billah, 2004). Morphometric studies revealed differences in traits in the population of the two weevil species across regions. In the males of *C. puncticollis,* the two variables that put the population into three clusters were *ewb* (elytra width at base) and *pwa* (pronotum width at apex). The population from the Central Region had the largest trait, followed by those from Eastern and Volta (which did not differ significantly); Greater Accra had the smallest size. In terms of *pwa,* Greater Accra still had the smallest pronotum width at the apex, and Eastern the highest value, while Central and Volta were found between the extremes (and did not differ from each other). In the females, however, only one variable (*pwa*) was able to put the populations into three clusters, and the separation was as observed in the males – Eastern, Central (together with Volta) in the middle, and Greater Accra with the smallest size.

In *C. brunneus,* two variables (*ewa* and *hl*) were responsible for putting the males into three clusters. In terms of elytra width at apex, Central had the biggest size, followed by Volta, and then Eastern and Greater Accra (as one cluster). In the head length too, Central had the biggest value and Eastern the smallest value, with Volta and Greater Accra falling between the two values. Interestingly, Volta did not differ significantly from the high Central values, but neither did Greater Accra differ significantly from the low Eastern values. In the females, however, no variable could separate the populations into more than two clusters, and only two variables (*ewa* and *pwa*) had significant differences. While *pwa* was common in both the male and female populations of *C. puncticollis, ewa* was common in both the male and female populations of *C. brunneus.*

Some of these characteristics have been reported in previous studies to be the source of variation and were used to describe individuals. Although the presence of cryptic species cannot be ruled out, the variation in traits could be the result of the polytypic status of some of the species such as the *C. puncticollis* group, to which species have been assigned to the group (Wolfe, 1991), and also due to the effect of the environment/habitat (Chown & Gaston, 2010). Traditional morphometrics represents one of the most commonly used ways of investigating intra- and inter- specific body size variation among organisms within a given population. This study has revealed differences in traits in the population of the two weevil species across regions.

For the 12 variables used in this study, the multivariate analyses were able to rearrange and rank those that played principal roles in the separation of the individuals into the population identities assigned them. There were 2-7 variables that were used in the four *Cylas* populations (*C. puncticollis* males + females and *C. brunneus* males + females). In the *C. puncticollis* males, two of the variables (*ewb* and *pwa*) could be used to separate populations from the four regions into three clusters, while five other variables (*bl, ewa, pl, pw* and *pwb*) separated the populations into two clusters. In the females of the same species, one variable (*pwa*) separated the populations into three clusters, while four others (*el, hw, rl* and *pwb*) could only separate them into two clusters. In the *C. brunneus* males, two variables (*ewa* and *hl*) separated the populations into three clusters, while four others (*ewb, rl, pwa,* and *pwb*) could only separate them into two clusters. In the females, only two variables (*ewa* and *pwa*) were of significant differences to separate them into two clusters. In all cases, the variables which contributed most in grouping of the populations were *pwa, pwb, pl, pw, ewa, ewb,*and occasionally, *bl, hl, hw, rl,* and *el*, representing measurements of different parts of the pronotum, elytra, head, rostrum, and body length. These have thus become the principal variables that contribute most to the variations observed in the populations.

Conclusion

Identified as a powerful tool in species delimitation, the morphometric study has provided an in-depth knowledge of the status of the sweet potato weevil. It has been demonstrated in this study that variations in body size exist among individuals within each species across and within the four regions. It is therefore suggested that more studies be conducted on the two common species, *C. puncticollis* and *C. brunneus*, to ascertain their true taxonomic status, which has important practical implications for the effective development and use of management strategies against such pest complexes, and which can also result in the incorrect establishment of trade barriers for agricultural commodities that serve as hosts of the sweet potato pests.

Acknowledgments

The second author received a scholarship from the German Academic Exchange Service (DAAD) through the African Regional Postgraduate Programme in Insect Science (ARPPIS) at the University of Ghana, Legon, Ghana. We thank Henry Davis, ARPPIS Curator, for helping in the identification of the insects. We also thank the Royal Belgian Institute of Natural Sciences and Belgian Focal Point of the Global Taxonomy Initiative for the facilities and the partial grant which allowed him to visit their lab for further training in the identification of insects.

References

Agbessenou, A., Wilson, D.D., Billah, M.K., Dekoninck, W., Vangestel, C., Carey, E.E. and Adofo, K. (2016). Survey on the distribution of the Sweet potato weevil, *Cylas* species-complex (Coleoptera: Brentidae) in Ghana.*Bulletin de la Société royale belge d'Entomologie/Bulletin van de Koninklijke Belgische Vereniging voor Entomologie (Bulletin SRBE/KBVE*), 152: 81-88.

Bidzakin, J. K., Acheremu, K., and Carey, E. E. (2014). Needs assessment of sweet potato production in Northern Ghana: Implications for research and extension efforts. ARPN *Journal of Agricultural and Biological Science*, 9: 315-319.

Bill and Melinda Gates Foundation (2011). Agricultural Development Strategy Overview. Available at: https://docs.gatesfoundation.org/Documents/agricultural-development-strategy-overview.pdf

Billah, M.K. (2004). Biosystematic Studies of *Psyttalia* species (Hymenoptera: Braconidae): Parasitoids Attacking Fruit-Infesting Flies (Diptera: Tephritidae) in Africa. PhD Dissertation, University of Ghana, Legon. 136 pp.

Billah, M.K., Kimani-Njogu, S., Overholt, W.A., Wharton, R.A., Wilson, D.D. & Cobblah, M.A. (2005). The effect of host larvae on three Psyttalia species (Hymenoptera: Braconidae): parasitoids of fruit-infesting flies (Diptera: Tephritidae). *International Journal of Tropical Insect Science*, 25(3): 168–175.

Billah, M. K., Kimani-Njogu, S. W., Wharton, R. A., Woolley, J. B., and Masiga, D. (2008). Comparison of five allopatric fruit fly parasitoid populations (*Psyttalia* species) (Hymenoptera: Braconidae) from coffee fields, using morphometric and molecular methods. *Bulletin of Entomological Research*, 98: 63-75.

Bookstein, F. L. (1991). Morphometric Tools for Landmark Data. Cambridge University Press. 435 pp.

Bouis, H., and Islam, Y. (2012). Delivering Nutrients Widely through Bio-fortification: Building on Orange Sweet Potato - Scaling Up in Agriculture, Rural Development and Nutrition. Focus 19, Brief 11. Washington, DC: International Food Policy Research Institute.

Bulgarella, M., Trewick, S. A., Godfrey, A. J. R., Sinclair, B. J., & Morgan-Richards, M. (2015). Elevational variation in adult body size and growth rate but not in metabolic rate in the tree weta, *Hemideina crassidens*. *Journal of Insect Physiology*, 75: 30-38.

Chown, S. L., & Gaston, K. J. (2010). Body size variation in insects: a macro-ecological perspective. *Biological Reviews*, 85: 139-169.

Ewell, P. T. & Mutuura, J. N. (1994). *Sweet potato in the food system of eastern and southern Africa, pp. 405-420. In:* Ofori, F., Hahn, S. K. (Eds.). Tropical root crops in a developing economy. Proceedings of the ninth symposium of the International Society for Tropical Root Crops,20–26 October 1991, Accra, International Institute for Tropical Agriculture (IITA), Ibadan.

Kimani-Njogu, S. W., Trostle, M.K., Wharton, R.A., Woolley, J.B. & Raspi, A. (2001). Biosystematics of the Psyttalia concolor species complex (Hymenoptera: Braconidae: Opiinae): the identity of populations attacking Ceratitis capitata (Diptera: Tephritidae) in coffee in Kenya. Biological Control, 20: 167–174.

Low, J. W. (2013). Bio-fortified crops with a visible trait: the example of orange-fleshed sweetpotato in Sub-Saharan Africa, pp. 371–384. In: V.R. Preedy, R. Srirajaskanthan and V.B. Patel (Eds). *Handbook of Food Fortification and Health*, New York, NY, USA: Springer.

Low, J. W., Arimond, M., Osman, N., Cunguara, B., Zano, F. and Tschirley, D. (2007). A food-based approach introducing orange-fleshed sweetpotatoes increased vitamin A intake and serum retinol concentrations in young children in rural Mozambique. *Journal of Nutrition,* 137: 1320-1327.

Marcus, L. F. (1990). Traditional morphometrics, pp. 77–122. *In*: Rohlf, F. J and Bookstein, F. L. Proceedings of the Michigan Morphometric Workshop. Special Publication No. 2. Ann Arbor MI, The University of Michigan Museum of Zoology.

McSorley, R., and Jansson, R. K. (1991). Spatial Patterns of *Cylas formicarius* in Sweet Potato Fields and Development of a Sampling Plan, pp. 157-168. In: R.K. Jansson and K.V. Raman (Eds). Sweetpotato Pest Management. A Global Perspective. Westview Press, Boulder, Colorado, USA.

Pfeiffer, W. H. & McClafferty, B. (2007). HarvestPlus: breeding crops for better nutrition. *Crop Sci.,* 47: 88-105.

Plavcan, J. M. (2012). Body size, size variation, and sexual size dimorphism in early *H*omo. *Current Anthropology*, 53: S409-S423.

Rohlf, F.J. & Bookstein, F.L. (1990). Proceedings of the Michigan Morphometrics Workshop. Special Publication No. 2 (The Blue Book). Ann Arbor, Michigan, University of Michigan, Museum of Zoology.

Statistical Analyses Software (SAS) Institute Inc. (2003). SAS/STAT1 User's Guide, Version 8.2. Cary, NC, USA.

Smit, N. E. J. M. (1997a). Integrated pest management for sweetpotato in Eastern Africa. Ph. D. Thesis *Landbouw Uninversiteit Wageningen*, Netherlands.

Smit, N. E. J. M. (1997b). The effect of the indigenous cultural practices of in-ground storage and piecemeal harvesting of sweetpotato on yield and quality losses caused by sweetpotato weevil in Uganda. *Agriculture, Ecosystems & Environment*, 64: 191–200.

Smit, N. E. J. M., Downham, M. C. A., Laboke, P. O., Hall, D. R., and Odongo,B. (2001). Mass-trapping male *Cylas* spp. with sex pheromones: a potential IPM component in sweet potato production in Uganda. *Crop Protection*, 20: 643-651.

Smit, N. E. J. M., and Matengo, L. O. (1995). Farmers' cultural practices and their effects on pest control in sweetpotato in South Nyanza, Kenya. *International Journal of Pest Management*, 41: 2-7.

Smit, N. E. J. M., and van Huis, A. (1999). Biology of the African sweet potato weevil species *C. puncticollis* (Boheman) and *C. brunneus* (Fabricius) (Coleoptera: Apionidae). *The Journal of Food Technology in Africa*, 4: 103-107.

Umphrey, G.J. (1996). Morphometric discrimination among sibling species in the fulva-rudis-texana complex of the ant genus *Aphaenogaster* (Hymenoptera: Formicidae). *Canadian Journal of Zoology*, 74(3), 528–559.

Wolfe, G.W. (1991). The origin and dispersal of the pest species of *Cylas* with a Key to the pest species groups of the world, pp. 13-44. *In:* Sweetpotato Pest Management. A Global Perspective (Edited by R.K. Jansson and K.V. Raman). Westview Press, Boulder, Colorado, USA.

Cocoa Pod Husk Plus Enzymes is a Potential Feed Ingredient for Hy-Line Silver Brown Laying Hens

Thomas N. Nortey[1*], Dorinda V. Kpogo[1], Augustine Naazie[1] and Emmanuel O. K. Oddoye[2]

[1]Department of Animal Science, College of Basic and Applied Sciences, University of Ghana, Legon, Accra
[2]Cocoa Research Institute of Ghana, New Tafo-Akim
***Corresponding author:** tnortey@ug.edu.gh

ABSTRACT

The aim of the experiment was to determine whether the inclusion of pelleted cocoa pod husks (CPH) in diets for Hyline Silver Brown (HSB) layers would affect egg laying performance and egg characteristics. Two hundred and sixteen (216), 36-week old, HSB layers in battery cages were randomly assigned to twelve experimental diets for 12 weeks in a completely randomized design (CRD). Diets had three levels of CPH inclusion: 0, 10 and 15%. For each inclusion level, the diets were further sub-divided into four treatments. The four treatments either had, i) no enzyme, ii) phytase only, iii) a commercial enzymes cocktail only, or iv) a mixture of both phytase and cocktail. The enzyme cocktail and phytase were added at rates of 250g and 300g per ton of complete feed respectively according to the manufacturer's recommendation. Overall, adding CPH did not affect Average Daily Feed Intake, although a combination of an enzyme cocktail and phytase improved ADFI, especially at the 15% CPH-inclusion level. Hen-day egg production of birds on diets with 0, 10 and 15% CPH, with an enzyme cocktail alone (78.70, 76.23 and 71.96% respectively), or with a combination of enzyme cocktail and phytase (79.5, 71.89 and 72.16% respectively) was better than egg production of hens on the other diets. There were no effects of CPH or enzyme addition on egg quality characteristics. Cocoa pod husk can be used in diets for HSB birds (up to 15%) without adversely affecting production performance or egg quality characteristics when appropriate exogenous enzymes are added.

Keywords: Egg production, Egg quality, Enzymes, Hy-Line Silver Brown Layers

Introduction

Agriculture forms the backbone of many developing countries. In Ghana it contributed 38.8% of the Gross Domestic Product (GDP) in fiscal year 2012, with the livestock sector contributing 7.5% (Ministry of Food and Agriculture [MoFA] 2012). Commercial poultry production, in particular, provides easily accessible and affordable meat and eggs.

Worldwide, a major contributor to the total cost of raising poultry is feed (Teguia & Beynen, 2004), with traditional cereal grains like maize, rice, wheat and millet constituting the major energy providers (Ravindran & Blair, 1993). Such traditional cereal grains are however major food sources for humans as well, and consequently their use in animal feed brings about undesirable competition with man for this resource. It is important therefore to seek local replacements for traditional feed for livestock in order to alleviate the stress imposed on them (Teguia & Beynen, 2004).

Apart from grains, roots and tubers like cassava root meal have been shown to be potential energy sources for poultry, and have been experimented with some degree of success in poultry feed (Adeniji & Balogun, 2003; Nortey *et al.,* 2013). Cocoa pod husk (CPH) is a by-product of cocoa processing. It is readily available, has high levels of protein, energy and other nutrients, and could be used in animal feeding. Compared to maize however, cocoa pod

husk (CPH) is relatively high in fibre. It is also high in lignin (14%) and non-starch polysaccharides (NSP) like hemicellulose (11%), cellulose (35%) and pectin (6%) (Alemawor *et al.*, 2010). The phosphorous in plant based ingredients like CPH also exists as phytate phosphorous (P) (Adeola & Cowieson, 2011; Adeola *et al.*, 2004). Since monogastrics do not by themselves possess the necessary enzymes to hydrolyse both fibre and phytate P (Yu *et al.*, 2004), diets high in these nutrients need to be supplemented with the requisite exogenous phytase and carbohydrase enzymes, if production performance is to be maintained. Undigested NSP can influence intestinal transit time and increase digesta viscosity (White *et al.*, 1981). Both result in inefficient nutrient absorption which ultimately affects the growth and egg laying performance of birds. Although some work has been done on the use of CPH in monogastric diets, little or no literature exists on the use of CPH as a potential feed ingredient in Hy-Line Silver Brown layer hens. The HSB layer hen is a white bird that lays brown eggs, and is a new strain that has recently been introduced to Ghanaian poultry farmers.

The hypothesis of this study was that CPH in the presence of exogenous enzymes could be used in HSB layer hen diets without adversely affecting performance. The objective was to determine the effect that CPH inclusion in diets with appropriate exogenous enzyme supplementation has on egg production and quality characteristics of HSB layers.

Materials and Methods

The trial was carried out at the Livestock and Poultry Research Centre (LIPREC) of the University of Ghana (UG).

Preparation of dried cocoa pod husk

Fresh cocoa (*Theobroma cacao*) pods were harvested from the cocoa plantations of the Cocoa Research Institute of Ghana (CRIG), New-Tafo in the Eastern Region of Ghana. They were cracked open to remove the cocoa beans together with the placenta. The husks were then chopped into slices (average length 2 cm) at the Product Development Unit of CRIG. They were dried in the sun for about 24 hours to reduce the moisture content to about 80%. The pre-dried slices were then passed through a combination mincer and pelleting machine to produce pellets (about10-12 mm). The pellets were again sun-dried for about 48-72 hours to further reduce moisture content to about 10% and then stored until use.

Dietary Treatment, birds and management

Twelve experimental diets consisting of three main diets initially formulated to contain 0, 10 and 15% CPH were used in the trial. Each main diet was further sub-divided into four parts. Part one was not treated any further. Parts two, three and four were treated respectively with phytase alone (300g/ton of complete feed), a commercial enzyme cocktail alone (250g/ton of complete feed), and a combination of both phytase and the enzyme cocktail at the stated inclusion levels. Thus T1, T2, T3 and T4 represented diets with a) 0% CPH with no exogenous enzyme, b) 0% CPH plus phytase alone, c) 0% CPH plus enzyme cocktail alone, and d) 0% CPH plus a combination of phytase and an enzyme cocktail. Treatments five to eight (T5, T6, T7 and T8), and nine to twelve (T9, T10, T11 and T12) represented diets with 10% and 15% CPH respectively, and with the same combination of enzymes as in T1 to T4. The microbial phytase used was ZY Phytase 5000© which is manufactured by Lohmann Animal Health, Germany. The enzyme cocktail contained phytase, amylase, protease, cellulase, xylanase, β-glucanase and pectinase, and was supplied by Zoetis under the brand name Enziver.

The animal protocol was approved by the LIPREC Research Committee on Animal Use and Experimentation and followed principles recommended by the Noguchi Institutional Animal Care and Use Committee of the University of Ghana. Two hundred and sixteen (216) Hy-Line Silver Brown (HSB) layers at 36 weeks of age were randomly assigned in battery cages to twelve experimental diets in a Completely Randomized Design. The layers were fed the respective diets over a period of

twelve weeks. The experiment was set up in a 3 x 4 factorial arrangement with three levels of CPH and four levels of enzymes. There were 18 birds in each treatment, made up of nine replications of two birds per replication/cage. The laying hens were allowed seven (7) days on the experimental diets for conditioning. The experiment consisted of three periods of 28 days each. Birds were fed the same treatment diet during the experimental period. Water was provided *ad libitum*.

Data collection/criteria

A known amount of feed was provided every morning, and feed left over after 24 hours was collected and weighed to determine feed intake. This amount represented the average daily feed intake (ADFI). Feed conversion efficiency (FCE) was calculated as the ratio of weight of eggs to feed intake. Eggs were collected twice a day at 08:00 and 16:00. Records of egg weight, hen-day and hen-housed egg production performance were kept daily and summarized on a weekly basis.

Six eggs that had been laid within a two hour period on days 28, 56 and 84 were selected at random from each treatment and parameters such as shell thickness, egg length and width, and albumen height were determined within 24 hours of collection. For egg width (at the broadest end) and shell thickness measurements, a digital caliper Model AD-5761-150 (A&D Company Ltd. Yamagata, Japan) with a sensitivity of 0.01mm was used. Egg weight was measured with an electronic balance (OHAUS-Pioneer ™, Ohaus Corp., USA; sensitivity of 0.01g). Albumen height was taken at three points between the yolk and edge of the thick albumen and the results averaged. The Haugh Unit was calculated by the method described by Haugh (1937) as follows:

$$\mathbf{HU = 100 * \log\left[H - \frac{\sqrt{G\,(30\,W^{0.37} + 100)}}{100} + 1.9\right]}$$

Where:
HU = Haugh unit
H= observed height of the albumen in millimeters
W = weight of egg in grams
G = the gravitational constant, 32.2

Chemical Analysis

The proximate chemical composition of all the major ingredients used was analyzed using methods outlined in the Association of Official Analytical Chemists (AOAC, 1995). Calcium and phosphorus were determined according to the methods outlined by James (1996) and AOAC (1995).

Statistical Analyses

All data gathered were subjected to statistical analysis using the Generalised Linear Model procedure of the Statistical Analysis Systems Institute (SAS, 1999). Significant differences among means were separated using the Student Newman-Kuels (SNK) Test. *A priori*, it was decided to compare the following treatments which were of particular interest, using contrasts:

All diets without enzymes versus all diets with both phytase plus cocktail

All diets without enzymes versus all diets with only a cocktail

All diets without enzymes versus all diets with only phytase

All diets with only phytase versus all diets with only a cocktail

All diets with phytase alone versus all diets with both phytase plus a cocktail

All diets with only a cocktail versus all diets with both phytase and a cocktail

Results

The chemical composition of the CPH used for the trial is shown in Table 1A. A profile of the diets used, showing CPH levels and combination of enzymes (T1 – T12), is shown in Table 1B. The composition and calculated values of the layer diets are shown in Table 2. The crude protein (CP) levels represent the recommended level of 15 -16.5% for brown type laying hens that are consuming between 100 and 120g of feed per day (NRC, 1994).

Table 1: A) Chemical composition of cocoa pod husk

Nutrient	Concentration (g/kg)
Dry matter	857.2
Crude protein	70.4
Crude fibre	311.2
Total ash	96.2
Ether extract	59.3
Calcium	8.1
Phosphorous	4.4

Table 1: B) Profile of layer diets showing CPH inclusion levels and combination of enzymes used

DIET	CPH inclusion	Phytase inclusion*	Enzyme cocktail inclusion
T1#	0	-	-
T2	0	+	-
T3	0	-	+
T4	0	+	+
T5	100	-	-
T6	100	+	-
T7	100	-	+
T8	100	+	+
T9	150	-	-
T10	150	+	-
T11	150	-	+
T12	150	+	+

* -: not included in treatment; +, included in treatment ;T#: Treatment

Table 2: Composition of the primary layer diets

Ingredients (%)	0% CPH*	10% CPH	15% CPH
Corn	51.55	51.55	51.55
Soybean meal	18	18	18
Wheat bran	20	10	5
Cocoa pod husk	0	10	15
L-Lysine HCl	0.15	0.15	0.15
DL-Methionine	0.15	0.15	0.15
Limestone	8.0	8.0	8.0
Dicalcium phosphate	0.7	0.7	0.7
Salt	0.5	0.5	0.5
Layer premix	0.25	0.25	0.25
BE3[1]	0.5	0.5	0.5
Toxin binder[2]	0.2	0.2	0.2
Total	100	100	100
Calculated Analysis			
ME, MJ/kg	9.75	9.55	9.45
CP, g/kg	162.4	156.4	153.4
CF, g/kg	35.7	43.8	47.9
Total Lys, g/kg	9.8	9.8	9.8
Total Met, g/kg	4.0	3.8	3.6
Ca, g/kg	31.2	31.4	31.4
P, g/kg	6.5	5.7	5.3

*Cocoa pod husk

[1:] *Lactobacillus sp, Bacillus sp, Saccharomyces sp* and Fermentation products.

[2:] Mycofix® Select 3.0 by Biomin

At the 0 CPH inclusion level (T1 to T4), there were no differences (P >0.05) in ADFI among the treatments (106.4, 106.4, 107.4 and 106.5g respectively) (Table 3). Similarly, when the level of CPH in the diets was 10% (T5 to T8), there were no differences (P >0.05) in ADFI among the different treatments (109.6, 108.7, 110.7 and 111.6 g respectively). ADFI of birds on T5 to T8 were however higher (P <0.05) than ADFI of birds on treatments with 0 CPH.

On average, birds ate more feed when the level of CPH in the diet was 15% (T9 to T12). ADFI of birds on T10 and T11 (111.5 and 111.6 g respectively) were similar to (P >0.05) ADFI of birds on T12 (110.8 g) and higher than ADFI of birds on T9 (108.1 g).

Table 3: Effect of cocoa pod husk on egg laying performance

	Inclusion level of cocoa pod husk													
	0%				10%				15%					
	Enzyme levels				Enzyme levels				Enzyme levels					
	T1	T2	T3	T4	T5	T6	T7	T8	T9	T10	T11	T12		
Parameter	None	Phy	Cock	Phy+ Cock	None	Phy	Cock	Phy+ Cock	None	Phy	Cock	Phy+ Cock	SEM	P-Value
ADFI (g)	106.4^{d}	106.4^{d}	107.4^{cd}	106.5^{d}	109.6^{abc}	108.7^{abc}	110.7^{ab}	111.6^{ad}	108.1^{bcd}	111.5^{a}	111.6^{a}	110.8^{ab}	0.74	<0.001
Egg production (%)*	78.77a	78.57^{a}	78.70^{a}	79.50^{a}	70.77^{b}	75.56^{ab}	75.49^{ab}	71.89^{b}	66.00^{c}	70.85^{b}	71.96^{b}	72.16^{b}	1.17	<0.001
Egg weight (g)	53.68^{d}	55.80^{c}	54.27^{d}	55.70^{c}	55.70^{c}	55.35^{c}	55.47^{c}	55.46^{c}	56.26^{bc}	57.18^{a}	56.80^{ab}	56.33^{bc}	0.25	<0.001
FCE	0.51	0.53	0.51	0.53	0.51	0.52	0.55	0.50	0.53	0.52	0.52	0.51	0.01	0.629

None= No enzyme added: Phy = Phytase added; Cock = Enzyme cocktail added; SEM = Standard Error of Means: * = Hen-Day egg production

The birds appeared to increase their daily feed intake when enzymes were added to the diet.

There was no effect (P <0.05) of enzyme supplementation on hen day egg production in diets with 0 and 10% CPH. For birds on T1, T2, T3 and T4, hen day egg production was 78.77, 78.57, 78.70 and 79.50% respectively.

Birds on T9 (15% CPH; no enzymes) had the lowest hen day egg production (66.0%) and this was different (P <0.05) from all the other hen-day production values. Birds on T10, T11 and T12 had egg production values of 70.85, 71.96 and 72.16% respectively, and these values were not different from each other or from values obtained for birds on T5 and T8. The cocktail and the mixture of cocktail plus phytase significantly improved the production at the 15% inclusion rate despite its being the lowest. There were no differences in FCE among the various treatments.

There were no differences (P >0.05) in egg weights at the 10% CPH inclusion level irrespective of the presence of enzymes. Egg weights for birds on T1 and T3 (53.68 and 54.27 g respectively) were lower (P <0.05) than egg weights of birds on T2 and T4 (55.8 and 55.7 g respectively), but similar to egg weights of birds on T5 to T8. The heaviest eggs (57.18 g) were recorded for birds on T10 (15% CPH plus phytase). This was similar to (P >0.05) egg weight of birds on T11 (56.80 g), but heavier (P <0.05) than eggs from birds on all the experimental diets. There were no differences in egg length and width, shell thickness, albumin height and Haugh Unit (Table 4).

A-priori contrasts between some treatments of specific interest for production parameters indicated differences in ADFI, egg weight, and hen day egg production (Table 5). Average daily feed intake when no enzyme was added was 108.0 g irrespective of the level of CPH. This was lower than (P <0.05) ADFI when phytase plus a cocktail enzyme, cocktail alone, or phytase alone (109.6, 109.9 and 108.9 g respectively) was added. Similarly, egg weight when no enzyme was added to the feed was 55.21 g, and this was lower than egg weights of birds fed diets either with only a cocktail enzyme (55.51 g) or with phytase alone (56.11 g). Hen day egg production of hens fed diets without any enzyme was 71.85%. This was lower than egg production of hens fed diets with a mixture of phytase and a cocktail (74.52 g), a cocktail enzyme alone (75.38 g) or phytase alone (74.99 g) (P <0.05).

Table 4: Effect of cocoa pod husk on egg quality characteristics

	Inclusion level of cocoa pod husk													
	0%				10%				15%					
	Enzyme levels				Enzyme levels				Enzyme levels					
Parameter	None	Phy	Cock	Phy + Cock	None	Phy	Cock	Phy+ Cock	None	Phy	Cock	Phy+ Cock	SEM	P-Value
Egg Length (mm)	57.00	57.47	57.07	57.17	57.20	57.60	57.20	57.60	58.90	57.67	57.20	58.10	0.55	0.496
Egg width (mm)	41.33	41.60	42.03	41.53	41.30	41.34	41.87	41.3	42.57	42.07	41.50	42.03	0.36	0.247
Shell thickness (mm)	0.36	0.37	0.36	0.37	0.36	0.37	0.36	0.37	0.36	0.37	0.35	0.38	0.06	0.412
Albumin height (mm)	7.99	7.95	7.29	7.26	7.30	7.59	7.37	7.44	7.50	7.35	7.62	7.78	0.19	0.36
Haugh Unit	74.23	73.79	68.39	67.80	68.47	70.89	69.03	69.52	70.19	75.24	71.13	72.96	1.67	0.05

None= No enzyme added: Phy = Phytase added; Cock = Enzyme cocktail added; SEM = Standard Error of Means

Table 5: P-values of A priori treatment comparisons of interest: Production parameters

	P-Value					
PARAMETER	Non vs Phy +Cock	Non vs Cock	Non vs Phy	Phy vs Cock	Phy vs Phy+Cock	Cock vs Phy+Cock
ADFI	<0.001	<0.001	<0.001	0.951	0.513	0.474
Hen day production	<0.001	<0.001	0.006	0.556	<0.001	<0.001
FCE	0.894	0.790	0.445	0.303	0.369	0.895
Egg weight	<0.001	<0.001	<0.001	<0.085	0.075	0.953

None= No enzyme added: Phy = Phytase added; Cock = Enzyme cocktail added; SEM = Standard Error of Means

Discussion

Average daily feed intakes of the three main diets by the layers were 106.7, 110.2 and 110.5 g (0% CPH, 10% CPH and 15% CPH respectively). With increasing levels of CPH in the diets, ADFI tended to increase. This may be due to the increasing fibre levels leading to slightly reducing energy densities as the dietary levels of CPH increased. The birds were fed *ad-lib*, and monogastrics like birds will eat more of a diet that is low in nutrient density in an attempt to meet their daily nutrient requirements, particularly energy (Leeson & Summers, 1997). This phenomenon has been observed in broilers by Adeyanju *et al*. (1976) and Alemawor *et al*. (2010) and in layers by Umar Faruk *et al*. (2010).

With increasing dietary CPH levels, hen-housed egg production generally decreased. The average drop in production when CPH was first introduced at a level of 100g per kg was 5% (78.89 to 73.43%) and this was greater than the drop in production when the level of CPH was raised by a further 50 g to 150 g per kg (73.43 to 70.24). These averages represent all the values that were observed when the levels of CPH were 100 g per kg and 150 g per kg respectively, irrespective of enzyme addition.

It can be assumed from this observation that any anti-nutritive factor (ANF) present in CPH exerted a greater negative effect on egg production at a level between zero and 100g/kg than between 100 g/kg and 150 g/kg. Osei *et al.* (1991) however saw no adverse effects on egg production when CPH was included at a dietary level of 75 g per kg. It could be argued that the level of CPH inclusion was tolerable and so no adverse effects of the ANF were manifest. On average, egg weights were 54.9, 55.5 and 56.6 g in the 0%, 10% and 15% CPH diets respectively for the three levels of CPH inclusion. Thus egg weights showed an increase with increasing CPH inclusion in the diets. This increased egg weight followed a similar trend as their ADFI. Several factors affect the weight of an egg, including protein content of the diet, water intake, ADFI, atmospheric temperature and age. The HSB layers increased their feed intake as the level of CPH increased in the diet, and this could explain the resultant increase in egg weight.

Feed conversion efficiency (FCE) in egg production is the efficiency of converting feed into eggs. It is calculated as the weight of eggs (g) that a unit of feed (g) will produce over a period. With the observed trend in ADFI and egg weight, the lack of effect of CPH level in the diet on FCE was expected. The lack of an effect of CPH on shell thickness may be due to the fact that the levels of both calcium and phytate (P) in the diet, which are the main minerals needed for egg shell formation, were adequate and not out of balance. Internal egg parameters were not affected by the level of CPH in the diet.

The need to add exogenous enzymes to monogastric feeds becomes necessary when portions of the diet are such that the animal does not have the appropriate enzymes to hydrolyse them (Bedford, 2000; Brufau *et al.*, 2006). The phytate molecule in addition to phosphorous binds to other nutrients like amino acids, minerals and vitamins. The use of exogenous phytase has thus been demonstrated to improve the availability of these nutrients to monogastrics (Mroz, *et al.,* 1994; Liao *et al.*, 2005; Nortey *et al.*, 2007). The total P in the CPH determined in this study was 4 g/kg, of which a certain portion (not determined) was phytate P. Cocoa pod husk replaced wheat bran which has a total P content of 9 g/kg, of which 80% is phytate P (NRC, 1994). If it is assumed that the phytate P content of CPH, as a percentage of total P, was close to 100%, it can be seen that replacing wheat bran with CPH will result in a diet with a phytate content which is not significantly different from a diet based on wheat bran alone. The targeted substrates for the cocktail enzymes in addition to phytates are amyloses, proteins, celluloses, xylans, β-glucans and pectins. This group of enzymes degrade fibre and release energy (Khattak *et al.,* 2006). They improve nutrient utilization by reducing intestinal viscosity and also through demasking, which is the process whereby xylanase breaks down water-insoluble-pentosans found in cell walls of fibrous plant materials. Increased intestinal content viscosity slows transit time and retards nutrient absorption, with a resultant depression in chick growth (Antoniou *et al.,* 1981; Nasi 1988; Marquardt *et al.*,1994). Enzyme

addition increased ADFI at the various levels of CPH inclusion. This trend was contrary to observations by Osei & Oduro (2000) and Dong (1997).

Although addition of phytase or an enzyme cocktail by itself tended to increase ADFI, especially at the 15% CPH inclusion level in this trial (Table 3), a combination of both phytase and a cocktail caused a slightly higher numerical effect. This observation was contrary to the situation where enzyme addition can result in a drop in ADFI (Osei and Oduro, 2000). The theory behind a drop in ADFI upon enzyme supplementation is the phenomenon of nutrient uplift where exogenous enzyme addition causes a release of nutrients, resulting in the daily nutrient requirement of animals being met much more readily and thereby causing a cessation of feeding (Richardson, 1970). However, according to Smith & Bright-Taylor (1974), the glucostatic theory of feed intake regulation, as observed in some mammals, is either not present in poultry or is not well understood. Results from this study showed an absence of this theory. One can therefore speculate that the inclusion of enzymes, in addition to releasing nutrients, may have reduced (or prevented) any possible fibre-inducing intestinal viscosity. This will result in slightly faster intestinal transit times; thus, less feed in the Gastro-Intestinal Tract (GIT) will result in a feeling of emptiness, leading to a need to increase ADFI. The enzymes reduce the water holding capacity of the gut contents, thus increasing the dry matter (Khusheeba & Sajid, 2013). The fact that a combination of both enzymes in the diet resulted in a marginal increase in ADFI compared to either enzyme alone indicates that there is synergy between the two enzymes, and that the phytase content of the cocktail enzyme alone may not be sufficient. Increased ADFI in the presence of added enzymes could be the cause of an increase in average hen-day egg production and egg weights at each level of CPH inclusion. Although the addition of CPH resulted in a dilution effect of the diets, the resultant increase in ADFI in the presence of enzymes may have compensated for this. Internal egg parameters were not affected by enzyme addition in this trial.

A priori contrasts, performed to determine which of the enzymes and/or combination of enzymes resulted in improved production characteristics irrespective of CPH inclusion, showed that birds benefited significantly from enzyme addition when diets with added enzyme cocktails plus phytase were compared with diets with no enzymes added.

This was expected since in addition to phytase, the cocktail contained other enzymes which together would act synergistically to improve nutrient digestibility (Nortey *et al.*, 2008). The absence of any improvement, when the effect of phytase alone or a cocktail alone versus diets without any enzyme, seems to indicate that the suggested level of enzyme application was either not enough, or the type of substrate in the diets presented a unique "lock" that required slightly different enzyme combinations.

The use of phytase in monogastric diets in developing countries like Ghana must be encouraged. Once the di- and tri-valent bonds in phytic acid are broken by phytase, phosphorous and other encapsulated nutrients are released for use by the animal. Fibre degrading enzymes have not been so popular probably because the results have not always been positive (Nortey *et al.*, 2015). This may be because local ingredients, grown under local climatic and soil conditions, may have slightly different Non-Starch-Polysaccharide (NSP) profiles, which may present slightly different substrates to the commercially available enzymes developed in Europe and North America.

Conclusions

Results of this study on the use of CPH in diets for HSB layers suggest that cocoa pod husk can be included in diets up to a level of 100 g/kg in the presence of enzymes without affecting production or egg characteristics. Also, there was little to no overall advantage of phytase plus a cocktail over phytase or a cocktail alone.

References

Adeniji, A. A. & Balogun, O. O. (2003). Replacement value of cassava flour for maize in layers' diet containing bovine blood-rumen content meal. *Ghana Journal of Agricultural Science*, 36, 41 – 55.

Adeola, O. & Cowieson, A. J. (2011). Board-invited review: Opportunities and challenges in using exogenous enzymes to improve nonruminant animal production. *Journal of Animal Science*, 89, 3189-3218.

Adeola, O., Sands, J. S., Simmins, P. H. & Schulze, H. (2004). The efficacy of an Escherichia coli-derived phytase preparation. *Journal of Animal Science*, 82, 2657-2666.

Adeyanju, S. A., Ogutuga, D. B. A., Ilori, J. O. & Agebola, A. A. (1976). Cocoa husks in poultry diets. *Malaysian Agricultural Journal*, 4, 131-134.

Alemawor, F., Oddoye, E. O. K., Dzogbefia, V. P., Oldham, J. H. & Donkor, A. (2010). Broiler performance on finisher diets containing different levels of either *Pleurotus ostreatus*-fermented dried cocoa pod husk or dried cocoa pod husk supplemented with enzymes. *Tropical Animal Health* and *Production*, 42, 933-939.

Antoniou T., Marquardt, R. R. & Cansfield, P. E. (1981). Isolation, partial characterization and antinutritional activity of a factor (pentosans) in rye grain. *Journal of Agricultural and Food Chemistry*, 29, 1240-1247.

Association of Official Analytical Chemists (AOAC) (1995). Official Methods of Analysis. 16th Edition, Washington DC.

Bedford, M. R. (2000). Exogenous enzymes in monogastric nutrition – their current value and future benefits. *Animal Feed Science* and *Technology,* 86, 1-13.

Brufau, F., Francesch M. & Perez-Vendrell, A. M. (2006). The use of enzymes to improve cereal diets for animal feeding. *Journal* of the *Science* of *Food* and *Agriculture*, 86, 1705-1713.

Dong, D. D. (1997). Enzyme supplementation of corn-based and wheat-based layer diets. M.S. Thesis. UPLB College, Laguna, Philippines.

Haugh, R. R. (1937). The Haugh unit for measuring egg quality. *United States Egg and Poultry Magazine*, 43, 522-555.

James, C. S. (1996). Analytical chemistry of foods. *Blackie Academic and Professional, Glassgow*, 234-239.

Khattak, F. M., Pasha T. N., Hayat, Z. & Mahmud, A. (2006). Enzymes in poultry nutrition .Dept of poultry production, Dept. Of Animal Nutrition. University of Veterinary and Animal Sciences, Lahore, Pakistan. *Journal of Animal and Poultry Science*, 16, 1-2.

Khusheeba, M. & Sajid, M. (2013). A review on role of exogenous enzyme supplementation in poultry production. *Emirates Journal of Food and Agriculture,* 25(1), 66-80.

Leeson, S. & Summers, J. D. (1997). Commercial Poultry Nutrition, 2nd edn. University Books, Guelph, Canada. pp 355.

Liao, S. F., Sauer, W. C., Kies, A. K., Zhang, Y. C., Cervantes, M. & He, J. M. (2005). Effect of phytase supplementation to diets for weanling pigs on the digestibilities of crude protein, amino acids, and energy. *Journal of Animal Science*, 83, 625-633.

Marquardt, R. R., Boros, D., Guenter, W. & Crow, G. (1994). The nutritive value of barley, rye, wheat and corn for young chicks as affected by use of a *Trichoderma reesei* enzyme preparation. *Animal Feed Science and Technology,* 45, 363-378.

Ministry of Food and Agriculture (MoFA), Agriculture in Ghana: facts and figures (2012). http://mofa.gov.gh/site/wp-content/uploads/2014/03/AGRICULTURE-IN-GHANA-FF-2012-nov-2013.pdf (accessed on December 22, 2014).

Mroz, Z., Jongbloed, A. W. & Kemme, P. A. (1994). Apparent digestibility and retention of nutrients bound to phytate complexes as influenced by microbial phytase and feeding regimen in pigs. *Journal of Animal Science*, 72, 126-132.

Nasi, M. (1988). Enzyme supplementation of laying hen diets based on barley and oats. Proceedings of Alltech's Fourth Annual Symposium. Nicholasville, KY. pp. 199-204.

National Research Council (NRC). (1994). Nutrient requirements of poultry. 9th Rev. Ed. National Academics Press, Washington DC, USA.

Nortey, T. N., Kpogo, D. V., Kpogo, A. L., Naazie, A. & Oddoye E. O. K. (2015). Cocoa pod husk is a potential feed ingredient in laying hen diets. *Livestock Research for Rural Development*, Volume 27, Article #119. Retrieved December 13, 2017, from http://www.lrrd.org/lrrd27/6/nort27119.htm

Nortey, T. N., Manu-Barfo, P. & Naazie, A. (2013). Effect of sorghum barley brewers spent grain as a feed ingredient on broiler performance and carcass quality. *The Bulletin of Animal Health* and *Production* in *Africa,* 61, 89-99.

Nortey, T. N., Patience, J. F., Sands, J. S., Trottier, N. L. & Zijlstra, R. T. (2008). Effects of Xylanase supplementation on the apparent digestibility and digestible content of energy, amino acids, phosphorous, and calcium in wheat and wheat by-products from dry milling fed to grower swine. *Journal of Animal Science*, 86, 3450-3464.

Nortey, T. N., Patience, J. F., Simmins, P. H., Trotier, N. L. & Zijlstra, R. T. (2007). Effects of individual or combined xylanase and phytase supplementation on energy, amino acid, and phosphorus digestibility and growth performance of grower pigs fed wheat-based diets containing wheat millrun. *Journal of Animal Science*, 85, 1432-1443.

Osei, S. A., Atuahene, C. C., Heathcote, D., Frimpong, E. B. & Adomako, D. (1991). Cocoa pod-and-husk meal as a feed ingredient in layer diets. Anim. Feed Sci. Technol. 35, (3–4) 283–288.

Osei, S. A. & Oduro, S. (2000). Effects of dietary enzyme on broiler chickens fed diets containing wheat bran. *Journal of Animal and Feed Science*, 9, 681-686.

Ravindran, V. & Blair, R. (1993). Feed resources for poultry production in Asia and the Pacific. III. Animal protein sources. *Worlds Poultry Science Journal*, 49, 219–235.

Richardson, A. J. (1970). Blood glucose levels and food intake in the domestic chicken. *British Poultry Science,* 11, 501.

SAS Institute Inc. (1999). SAS User's Guide. SAS Institute, Cary, NC, USA.

Smith, C. J. V. & Bright-Taylor, B. (1974). Does glucostatic mechanism for food intake control exist in chicken? *Poultry Science*, 53, 1720.

Teguia, A. & Beynen, A. C. (2004). Nutritional aspects of broiler production in small-holder farms in Cameroon. *Livestock Research for Rural Development*, Vol. 16, Art. #7. Retrieved December 15th, 2014, from http://www.lrrd.org/lrrd16/1/tegu161.htm.

Umar Faruk, M., Bouvarel, I., Meme, N., Rideau, N., Roffidal, L., Tukur, H. M., Bastianelli, D., Nys, Y. & Lescoat. P. (2010). Sequential feeding using whole wheat and a separate protein-mineral concentrate improved feeding in laying hens. *Poultry Science*, 89, 785-796.

White, W. B., Bird, H. R., Sunde, M. L., Prentice, N., Burger, W. C. & Marlett, J. A. (1981). The viscosity interaction of barley beta-glucan with Trichoderma viride cellulase in the chick intestine. *Poultry Science*, 60, 1043-1048.

Yu, B., Jan, Y. C., Chung, T. K., Lee, T. T. & Chiou, P. W. S. (2004). Exogenous phytase activity in the gastrointestinal tract of broiler chickens. *Animal Feed Science and Technology*, 117, 295-303.

Petrogenetic Evolution of the Eastern Buem Volcanic Rocks, South-Eastern Ghana

Naa A. Agra[1]*, Daniel Kwayisi[1], Prince O. Amponsah[3, 4,] Samuel B. Dampare[2], Daniel Asiedu[1], Prosper M. Nude[1]

[1]University of Ghana, School of Physical and Mathematical Sciences, Department of Earth Science, P.O. Box LG 58, Legon-Accra, Ghana
[2]University of Ghana, School of Nuclear and Allied Sciences, P.O. Box LG 80, Legon-Accra, Ghana
[3]Université de Toulouse, CNRS, Géosciences Environnement Toulouse, Institut de Recherche pour le Développement, Observatoire Midi-Pyrénées, 14 Av. Edouard Belin, F-31400 Toulouse, France
[4]Azumah Resources Ghana limited, PMB CT452, Cantonments, Accra
***Corresponding author:** ntaki@ug.edu.gh

ABSTRACT

Petrography, major, trace element and Rare Earth Element (REE) data are presented for volcanic rocks from the Eastern Buem Structural Unit (BSU) in south-eastern Ghana to constrain their petrogenesis and tectonic setting. The volcanic rocks are generally aphanitic, ophitic and massive, although some varieties exhibit weak foliation. They are primarily composed of plagioclase and pyroxene. These primary minerals have either partially or wholly altered to chlorite, epidote, sericite and opaque minerals. The basalts have low TiO2 (0.56–1.19wt. %) content with fairly low magnesium numbers ranging from 38 to 55. They display flat to slightly depleted REE patterns and are mostly more enriched than chondrite. On the primitive mantle (PM) normalised spider diagram, they are variably enriched in Light Rare Earth Elements (LREE) and incompatible elements relative to normal mid-ocean ridge basalt (N-MORB), with similar Large-ion Lithophile Element (LILE) and High Field Strength Element (HFSE) patterns as enriched mid-ocean ridge basalt (E-MORB) but 10 fold more enriched than primitive mantle (PM). They show minor negative and positive Sr, positive Cs, Ba, Ta, La and Ce anomalies and minor negative Rb, Th, Zr and Ti anomalies. The basalts plot within the MORB mantle array on the Th/Yb versus the Nb/Yb diagram and have low Th/Nb ratios (0.07– 0.09) which indicate their derivation from asthenospheric sources with minimal or no contamination from crustal or subducted components. They show affinity to Enriched MORB on multi-trace element normalised diagrams. The E-MORB affinity of the basalts is also confirmed on Th–Hf–Nb, Y–La–Nb and V–Ti tectonic discrimination diagrams. These volcanic rocks may have erupted during rifting along the marginal basin of the WAC prior to peak collision during the Pan-African Orogeny.

Keywords: Basalt, Buem Structural Unit, Geodynamic evolution, Pan-African Orogeny, Petrogenesis

Introduction

The 600 Ma Pan African Dahomeyide orogenic belt, which occurs on the eastern margin of the West African Craton (WAC), crops out as the Dahomeyan, Togo and Buem Structural Units in SE Ghana. Rocks in this region are broadly composed of metamorphosed sedimentary packages, para- and ortho-gneisses, intrusive and volcanic materials which evolved during the Pan African event (Jones, 1990). During the last few years, rocks in this area have been subjected to various age dating geochemical and structural studies. Attoh and Nude (2008) worked on the tectonic significance of carbonatites and ultrahigh-pressure rocks in the suture

zone while Attoh *et al.* (2007) worked on the ages of the carbonatites and alkaline rocks in the suture zone. Others such as Grant (1969); Saunders (1970); Jones (1990); Affaton *et al.* (1997; 1980); Duclaux *et al.*, (2006) and several others have worked on the various rock types, their stratighraphy, and their ages, to understand the Pan-African orogeny.

Of interest to this work are the volcanic packages found within the Buem Structural Unit (BSU). The source component of the BSU volcanics and its geodynamic setting has been an issue of ongoing debate. Two contrasting views have been proposed on the source of the BSU volcanic rocks. According to Jones (1990), the volcanic rocks have characteristics of a consanguineous alkaline lava series in which felsic rocks have evolved by fractional crystallization which formed in a continental rift zone. Affaton *et al.* (1997), on the other hand, proposed that the volcanic mafic lavas were derived from tholeiitic magmas similar to E-MORB, which originated from the partial melting of the lithospheric mantle with a possible asthenospheric contribution. However, Nude *et al.* (2015) described the Buem volcanic rocks as representing mantle derived magmas with both alkaline and subalkaline signatures that may be related to a rifting event and eventual emplacement at the eastern passive margin of the WAC. Work on the Buem volcanic rocks in Ghana (Jones, 1990; Nude *et al.*, 2015) has been mainly on the volcanic rocks within the western BSU. Therefore, in order to have an all-inclusive view and to better characterize the source of the volcanic suites and theirrelationship to the Pan African event, the petrographic and geochemical characteristics of volcanic rocks of the eastern BSU have been analysed to find out how they compare to the volcanic rocks of the western BSU.

This research seeks to determine the mantle source from which the primary magma of the rocks was generated, magma type, percentage partial melting, depth of magma generation and contamination, and to establish the relationship between volcanic emplacement and the Pan African Orogeny. The results have been discussed and compared to previous studies done in areas where the BSU outcrops.

Regional Geological setting

The BSU occupies an irregular wide strip of about 15 km which trends NNE-SSW from SE Ghana to the Republic of Benin (Fig. 1). It is divided into the western unit which comprises nappe outliers of the Volta basin and the eastern unit which borders the Togo Structural Unit (Blay, 1991).

In general, BSU is composed of; a) clastic sediments, b) limestone and jasperoids, c) serpentinites d) volcanic rocks and e) intrusive rocks (Fig.2; Agyei Duodu *et al.*, 2009). The clastic rocks comprise sandstones, fine-grained quartzites, siltsones and red shales. They form the uppermost and lowermost parts of the succession. The jasperoids consist of a series of bedded, normally massive and sometimes brecciated red cherts. Some, however, may have formed by metasomatic alteration of the clastic sediments, limestone and volcanic rocks (Junner, 1940; Jones, 1990). Serpentinites are schistose in nature and rich in chromite. Volcanic rocks in the area consist predominantly of basalts, basaltic-andesite, trachytes and phonolite (Nude *et al.*, 2015). Pillow lavas have been recorded in a few places (Junner, 1936). The intrusives are mostly gabbros which are associated with the volcanic rocks (Kwayisi, 2014) and jaspers, and often intrude the shale (Taki, 2014). The BSU is normally unmetamorphosed or locally slightly metamorphosed up to prehnite-pumpellyite facies (Affaton *et al.*, 1997), and has experienced some deformation inferred from the presence of folds, joints and thrust faults within the rocks. The Buem is faulted by the North and South Nkonya fault systems.

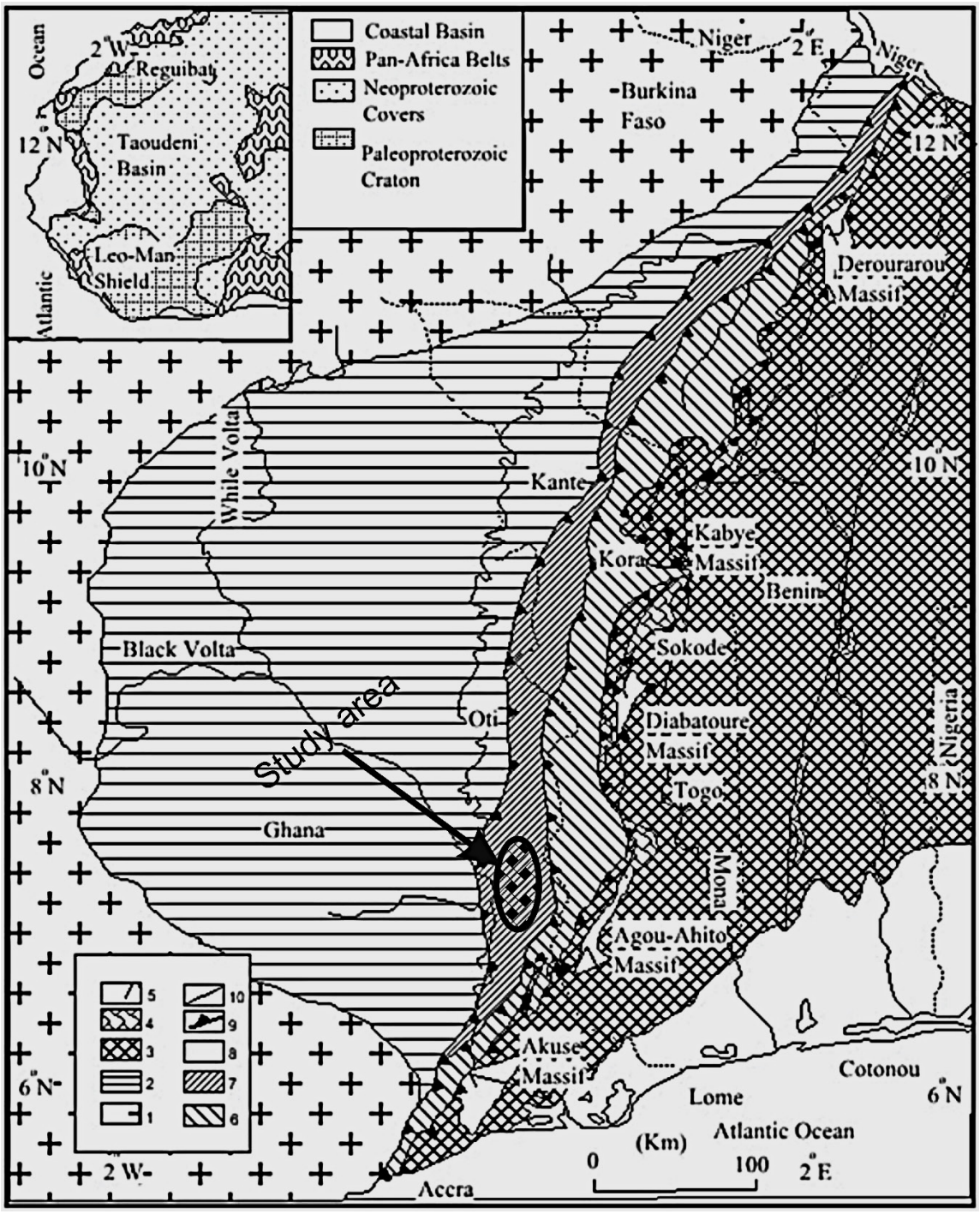

Fig. 1: Dahomeyide orogen showing the major tectonic units (Modified from Affaton *et al.*, 1997). 1 = Eburnean basement complex (WAC); 2 = Neoproterozoic to Paleozoic cover (Volta Basin); 3 = internal and external gneiss-migmatite units; 4 = kyanite bearing micaceous quartzites; 5 = basic and ultrabasic massifs of the suture zone; 6 = Atacora or Akwapim structural unit; 7 = Buem structural unit; 8 = Meso-Cenozoic cover of the Gulf of Guinea Basin; 9 = thrust contact; 10 = Kandi fault mylonitic zone

Folds observed have a general dip to the east, although some of the shales and sandstones dip to the west (Jones, 1990). BSU is considered a tectonic and metamorphic lateral equivalent of the middle part of the Voltaian supergroup that has been dated 620–640 Ma (Grant, 1969; Affaton *et al.*, 1980).

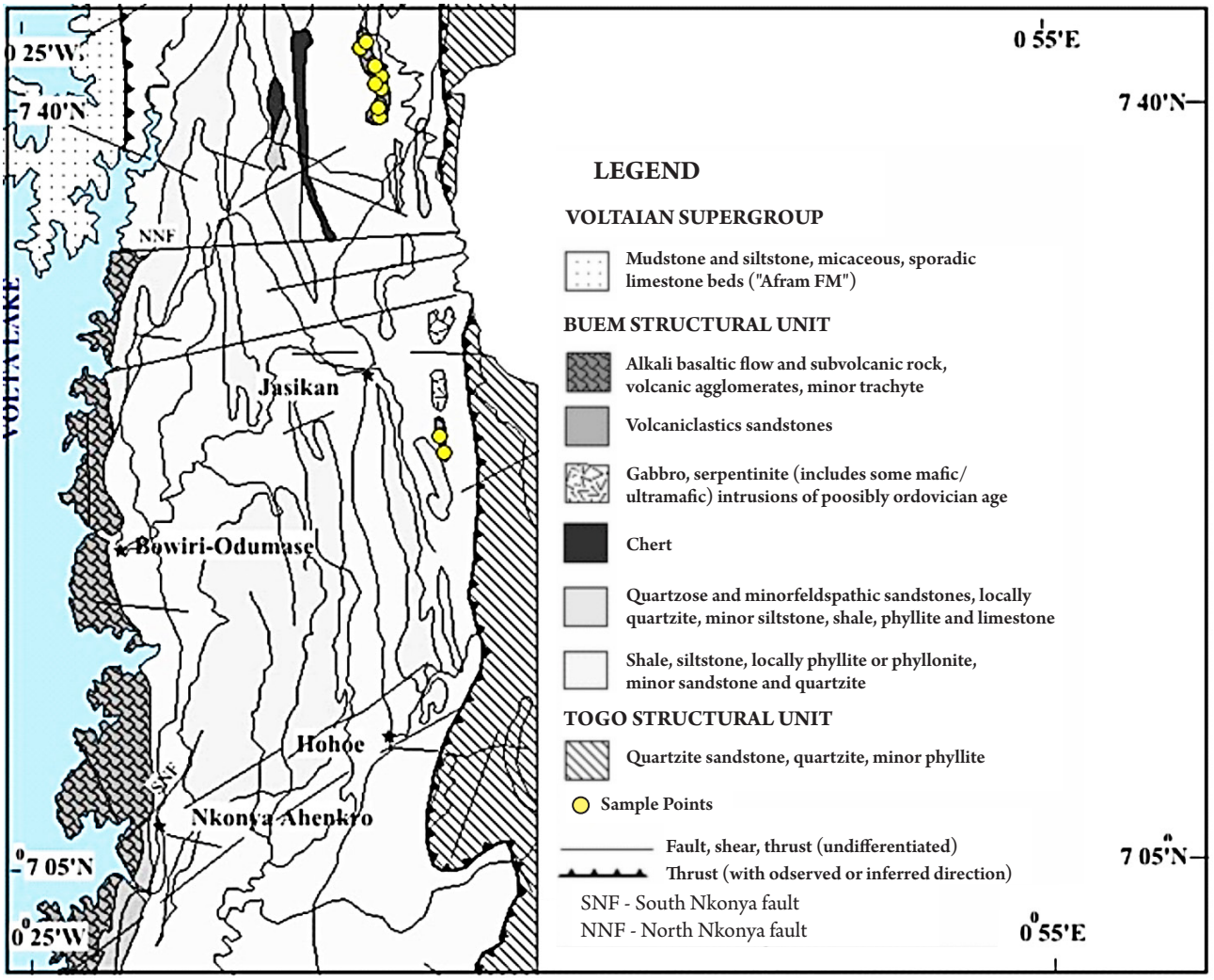

Fig. 2: Geological map of the Buem Structural Unit with yellow circles showing the sampling points (Modified from Agyei Duodu *et al.*, 2009)

Materials and Methods

Mineralogical and textural relationships of the rock samples were investigated using the Leica DM 750 petrographic microscope at the Department of Earth Science, University of Ghana, Ghana. Whole rock, trace element and REE composition of the samples were analyzed using the Inductively Coupled Plasma Mass-Spectroscopy (ICP-MS) and Inductively Coupled Plasma-Atomic Emission Spectroscopy (ICP-AES) at the ALS Chemex Laboratory in Vancouver, Canada. The major elements were determined using the x-ray fluorescence method on pressed powder pellets. Results obtained were corrected for spectral inter-element interferences and precision was better than 2%.

Petrography and whole rock geochemistry

Lithological and petrographic description

Most of the volcanic rocks were sampled along rivers and on small hills. The volcanic rocks are greenish or dark grey, fine-grained, dense, and mostly massive except for a few localized areas where they exhibit weak foliation and shear features (Figs. 3A and B). Microscopically, the volcanic rocks are ophitic (Fig. 3C) with few broken crystals and composed primarily of plagioclase and pyroxenes which have undergone various degrees of alteration into sericite, chlorite, epidote and opaque minerals. In some volcanic rocks, euhedral to subhedral plagioclase laths of various sizes, rarely twinned and randomly oriented, occur (Fig. 3D). Quartz- carbonate veinlets cut the volcanic rocks either concordantly or discordantly.

Whole rock geochemistry

The bulk rock major, trace, rare earth element concentrations of the rocks are presented in Table 1 below. The volcanic rocks are characterised by variable major oxide contents. SiO_2 content varies from 48.88 wt.% to 50.64 wt.%, TiO_2 from 0.56 wt. % to 1.19 wt.%, Al_2O_3 from 13.07 wt.% to 15.31 wt.% and Fe_2O_3t content from 6.76 wt.% to 10.40 wt.%, whereas the MgO content ranges from 5.35 wt.% to 10.70 wt.%, CaO from 8.80 wt.% to 13.38 wt.%, Na_2O from 0.42 to 4.04 wt.% and K_2O from 0.02 to 0.54 wt.%.

The magnesium numbers (Mg#) of the volcanic rocks are low, spanning a range of 38-55, which shows that the rocks are moderately fractionated. The volcanic rocks have Cr, Ni, Co and V, ranging from 390 to 830 ppm, 113 to 428 ppm, 26 to 50 ppm and 103 to 303 ppm respectively. On the Nb/Y versus Zr/TiO_2 (Fig. 4A) and SiO_2 versus K_2O (Fig. 4B) diagrams the volcanic rocks plot as sub-alkaline and low K tholeiitic basalts, respectively.

All the volcanic rock samples analyzed are more enriched relative to chondrite except one sample which exhibits a depleted LREE and a flat HREE pattern similar to N-MORB (Fig. 5A). They have $(La/Sm)N = 0.46 - 1.27$ and $(La/Yb)N = 0.36 - 1.38$ with total REE abundance (Σ REE) ranging from 20.02 to 53.03 ppm.

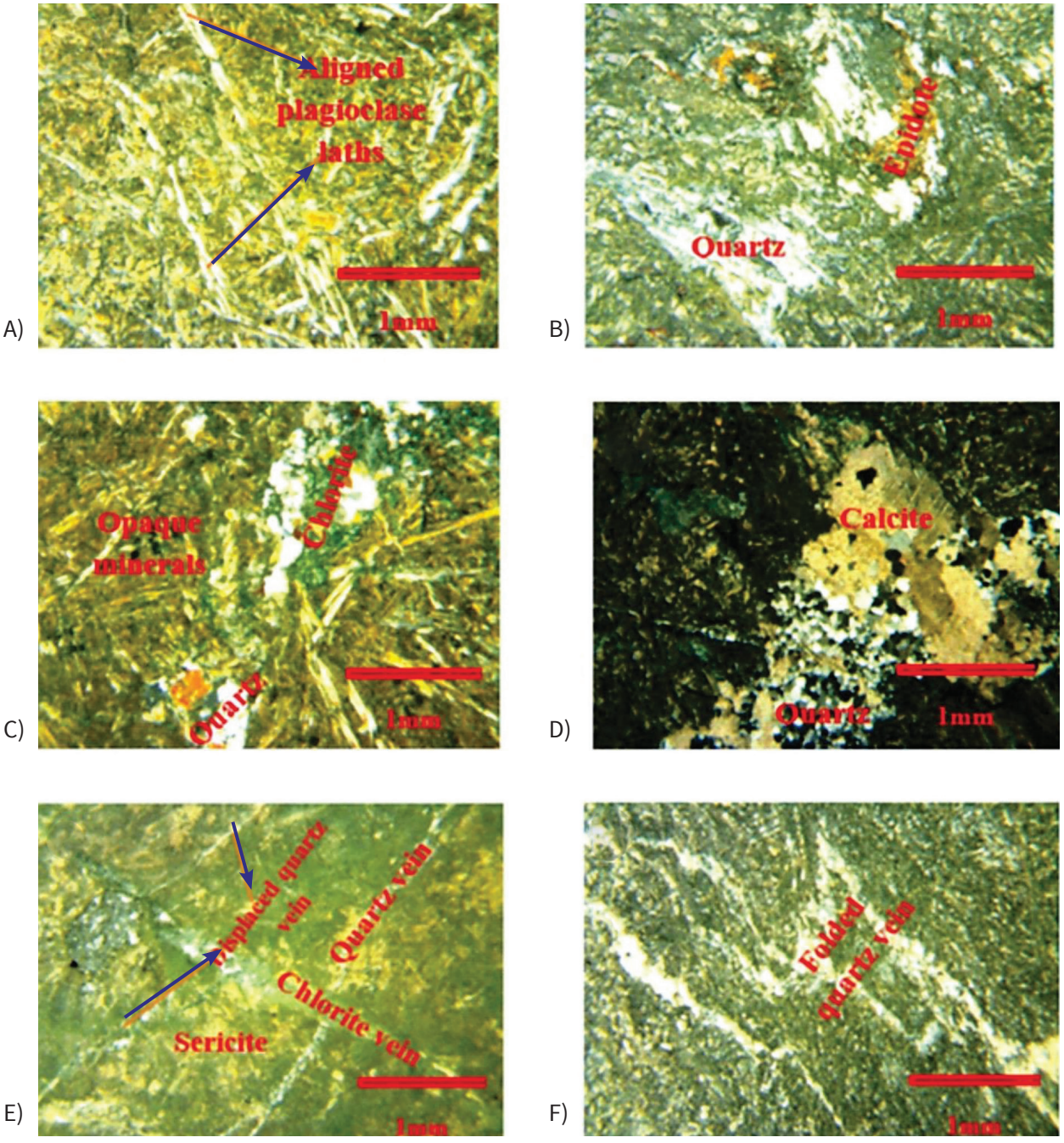

Fig. 3: A) Basalts with stretched and aligned plagioclase laths B) basalt showing epidote and quartz veins occurring together C) photomicrograph showing chlorite and quartz veins occurring together in basalt D) quartz and carbonate veins occurring together in basalt E) photomicrograph of basalt showing quartz vein cut by a chlorite vein F) basalt showing folded quartz vein.

On a primitive mantle (Sun and McDonough, 1989) normalized spider diagram, the volcanic rocks exhibit a flat pattern, but are more enriched in both LILE and HFSE than primitive mantle. They exhibit enrichment in Cs, Sr, Ba, Ta, La, Ce and Hf, and depletion in Sr, Rb, Th, K, Zr and Ti, with a relatively flat HFSE pattern (Fig. 5B). On the other hand, their multi-element pattern is similar to that of E-MORB, yet they are more enriched than N-MORB and depleted relative to OIB.

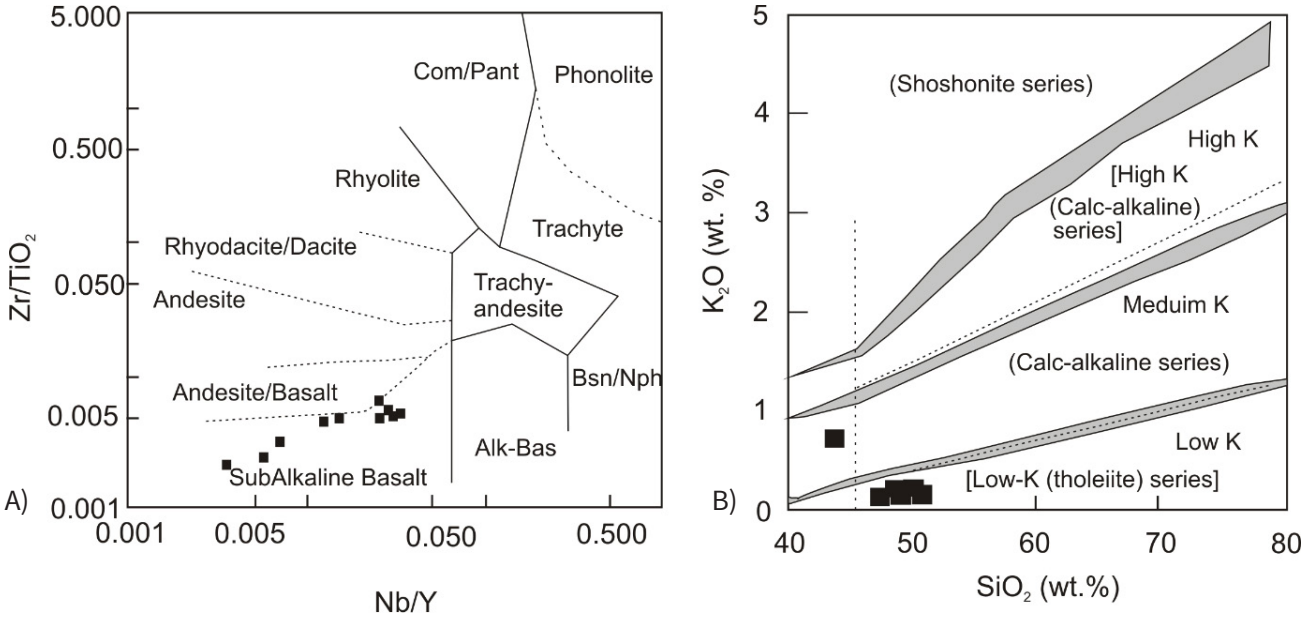

Fig. 4: A) Nb/Y versus Zr/TiO_2 plot of Winchester and Floyd (1977), B) K_2O versus $SiO=_2$ binary diagram by Le Maitre (1989), for the nine (9) sampled basalts

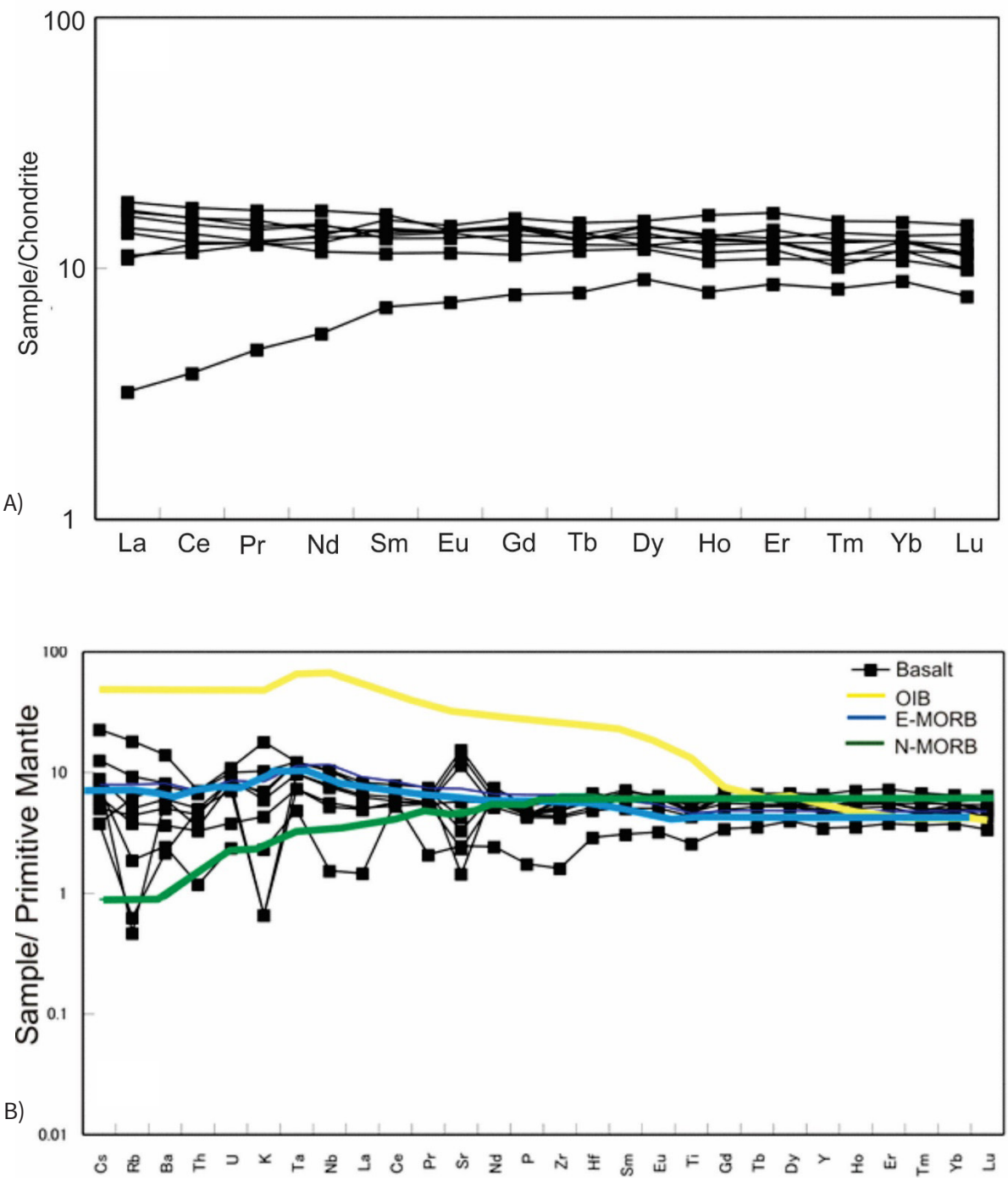

Fig. 5: A) Chondrite normalized REE plot, B) Primitive mantle normalized multi-element plot, for the nine (9) sampled basalts

Table 1: Major and trace element compositions of the basalts

wt.%	NT-TT-006A	NT-TT-006B	NT-TT-006B1	NT-TT-007A	NT-TT-007B	NT-TT-008	NT-TT-009A	NT-TT-009B	NT-TT-011
SiO_2	49.19	50.58	49.16	48.48	46.88	48.91	50.64	47.31	47.60
TiO_2	0.94	1.02	1.01	1.19	1.16	1.16	1.18	0.56	1.07
Al_2O_3	13.07	14.62	14.68	15.31	14.97	14.87	15.23	14.30	14.10
Fe_2O_3	9.06	6.76	6.80	7.83	9.99	8.56	8.66	8.64	10.40
MnO	0.17	0.14	0.15	0.14	0.17	0.15	0.13	0.15	0.18
MgO	8.54	6.35	6.16	6.37	9.66	7.45	5.35	10.70	6.73
CaO	13.38	11.44	12.05	10.32	8.80	10.51	11.69	11.56	12.38
Na_2O	0.42	2.59	2.74	3.38	2.29	3.05	4.04	1.69	1.75
K_2O	0.02	0.18	0.20	0.31	0.54	0.21	0.02	0.07	0.13
P_2O_5	0.09	0.10	0.10	0.10	0.12	0.10	0.10	0.04	0.10
LOI	4.98	5.67	6.63	5.94	4.86	4.86	2.84	4.34	5.11
Total	99.96	99.56	99.80	99.46	99.51	99.91	99.97	99.47	99.62
Mg #	55.80	48.50	48.40	44.90	49.20	46.50	38.20	55.30	39.30
Na_2O+K_2O	1.89	0.44	2.77	3.69	2.83	3.26	4.06	1.76	1.88
ppm									
Cr	760.00	430.00	550.00	490.00	460.00	390.00	470.00	830.00	460.00
Ni	428.00	123.00	110.00	151.00	133.00	129.00	113.00	230.00	137.00
Co	26.00	39.00	45.00	50.00	43.00	48.00	48.00	49.00	44.00
V	103.00	254.00	263.00	299.00	303.00	280.00	286.00	238.00	294.00
Cu	3.00	60.00	74.00	74.00	70.00	78.00	59.00	100.00	68.00
Zn	29.00	63.00	74.00	80.00	72.00	93.00	96.00	60.00	76.00
Cs	0.03	0.04	0.07	0.10	0.18	0.03	0.07	0.06	0.05
Rb	0.40	2.80	3.20	5.90	11.60	3.90	0.30	1.20	2.40
Ba	15.00	35.30	42.00	57.50	98.30	54.10	42.00	17.10	25.50
Th	0.42	0.38	0.43	0.59	0.60	0.57	0.30	0.10	0.28
U	0.15	0.18	0.18	0.21	0.23	0.17	0.17	0.05	0.08
Nb	5.40	5.60	6.20	7.40	7.50	7.30	3.70	1.10	4.00
Ta	0.40	0.40	0.50	0.50	0.50	0.50	0.30	0.20	0.30
K	166.00	1494.00	1660.00	2573.00	4483.00	1743.00	166.00	581.00	1079.00
La	4.30	4.50	5.00	5.20	5.70	5.30	3.40	1.00	3.50
Ce	10.30	11.10	12.10	12.90	14.10	12.80	10.10	3.10	9.40
Pr	1.54	1.57	1.74	1.80	2.08	1.90	1.54	0.58	1.52
Sr	241.00	294.00	327.00	70.00	30.30	89.90	49.40	52.10	121.50
P	405.90	419.00	423.40	427.70	506.30	427.70	449.60	165.90	423.40
Nd	7.00	8.00	8.90	9.00	10.20	8.40	8.10	3.30	7.60

Table 1 Continues

wt.%	NT-TT-006A	NT-TT-006B	NT-TT-006B1	NT-TT-007A	NT-TT-007B	NT-TT-008	NT-TT-009A	NT-TT-009B	NT-TT-011
Sm	2.24	2.63	2.70	2.57	3.20	2.78	3.04	1.37	2.82
Zr	47.00	67.00	49.00	64.00	64.00	59.00	55.00	18.00	54.00
Hf	1.50	2.10	1.60	1.90	1.90	1.80	1.80	0.90	1.80
Eu	0.85	1.02	1.04	0.97	1.04	1.03	1.09	0.54	1.03
Ti	5635.00	6115.00	6055.00	7134.00	6954.00	6954.00	7074.00	3357.00	6415.00
Gd	2.94	3.31	3.68	3.52	3.85	3.82	4.11	2.04	3.73
Tb	0.56	0.59	0.66	0.63	0.65	0.62	0.72	0.38	0.61
Dy	3.86	3.98	3.98	4.28	4.75	4.46	4.98	2.93	4.71
Y	21.20	22.10	24.10	23.30	26.10	24.20	30.00	15.80	26.10
Ho	0.77	0.83	0.93	0.95	0.98	0.89	1.17	0.58	0.96
Er	2.30	2.50	2.68	2.68	2.77	2.65	3.50	1.82	3.00
Tm	0.35	0.33	0.37	0.36	0.45	0.41	0.50	0.27	0.42
Yb	2.26	2.47	2.45	2.67	2.82	2.70	3.21	1.86	2.68
Lu	0.32	0.32	0.37	0.36	0.44	0.37	0.48	0.25	0.40

Discussion

From the information presented so far, the magma source, magma type, percentage partial melting, tectonic setting and others will be determined and discussed.

Alteration

The occurrence of secondary minerals such as chlorite, epidote and carbonates-quartz veins shows that the rocks are altered. LOI values of the volcanic rocks are moderate to high (2.84-6.63 wt. %), and this, coupled with scattered to positive correlation between SiO_2 and LOI (Fig. 6A), also suggests alteration and SiO_2 remobilisation in the volcanic rocks. Hence, before attempting petrogenetic and tectonic setting interpretation, it is important to evaluate the effect of alteration on the samples. The lack of correlation between LOI and Nb/La and Th/La (not shown) suggests that the primary Th-Nb-LREE concentrations in the rocks have not been disturbed much by hydrothermal alteration or metamorphism. Also, according to Gaffney *et al.* (2004) and Shervais *et al.* (2006), $K_2O/P_2O5 > 1$ indicates that samples have not undergone significant post-cooling alteration, which would mobilize K relative to P. Notwithstanding 2 samples with $K_2O/P_2O5 < 1$, the K_2O/P2O5 ratios for the volcanic rocks range from 1.54 to 4.66, which are mostly greater than 1. This also suggests minimal element mobility or alteration of the rocks. In addition, linear relations observed between Zr and most of the elements, especially REE, the transition elements and HFSE in the volcanic rocks, connote relative immobility of these elements. Therefore, although these rocks are altered, some of the elements' (REE, HFS and Transition elements) concentrations have been preserved in the rock. Thus, for petrogenetic and tectonic setting interpretations, we focused mainly on the immobile elements.

Petrogenesis

Magma differentiation/ Fractional crystallization

A decrease in MgO, CaO, Al_2O_3 and FeOt and an increasing SiO_2 observed on variation diagrams could suggest the fractional crystallisation of olivine, clinopyroxene and plagioclase in basalts during the early stages of magma evolution. However, clinopyroxene and plagioclase were observed in thin sections. The MgO content of the volcanic rocks is below 14 wt. % and coupled with the low magnesium numbers, suggests that

the rocks may have experienced some fractionation. On the AFM diagram (Fig. 6B), the samples plot away from MgO but towards FeO, which also suggests that the rocks have experienced some fractionation.

It is sometimes difficult to differentiate between the effects of fractional crystallization and/or partial melting on the compositions of primary magmas. However, compatible–incompatible element plots such as Ni and Th versus SiO_2 may provide a clue to the type of process taking place. Fractionation of ferromagnesian minerals such as olivine and clinopyroxene usually decreases the concentrations of compatible elements (e.g., Ni and Cr) and increases the concentrations of incompatible elements such as Th, La and Nd in the liquid (Dampare *et al.*, 2008). In the plots of Ni and Th versus SiO_2 (Fig. 7A & B), the volcanic rocks show a decrease in compatible and an increase in incompatible element concentrations with increasing SiO_2 content. It can be inferred from these plots that the volcanic rocks evolved mostly by fractional crystallization, but the effect of partial melting in the evolution of these rocks cannot be ruled out due to the high Th content as well as the dispersed trend observed from the Th versus SiO_2 diagram.

The fractional crystallisation trend observed in the volcanic rocks is further supported by the (La/Lu) chond versus Mg# diagram of Shervais *et al.* (2006). An increase in La/Lu with decreasing Mg# suggests assimilation of crustal component with fractional crystallisation

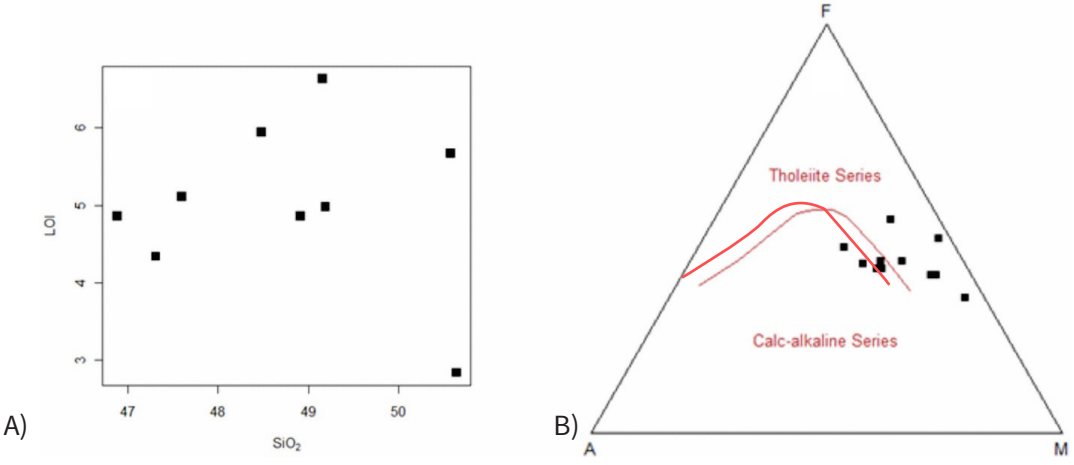

Fig. 6: A) LOI versus SiO_2 plot, B) AFM diagram by Irvine and Baragar (1971) plotted for the nine (9) basalts

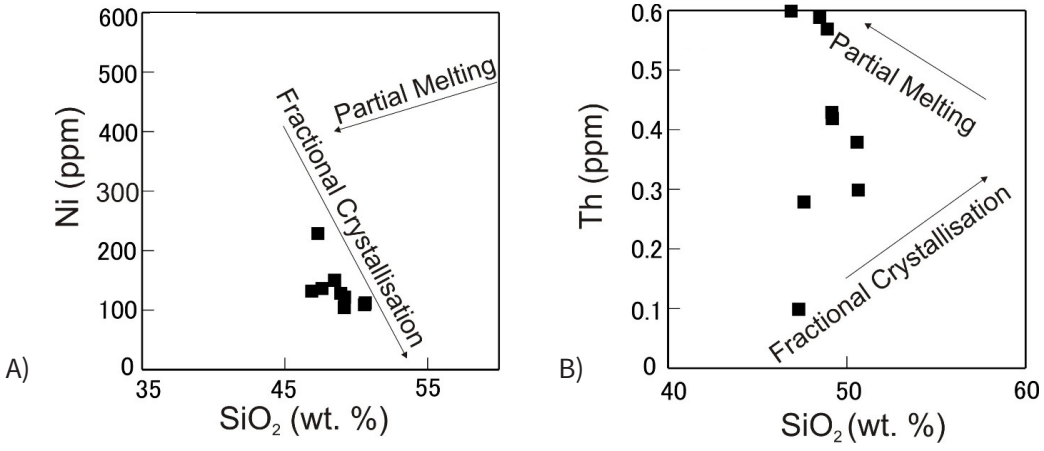

Fig. 7: A) SiO_2 versus Ni, B) SiO_2 versus Th plots for the nine (9) sampled basalts

(Shervais *et al.*, 2006). The low La/Lu content (Fig. 8) of the volcanic rocks thus suggests minimal or no assimilation of crustal component following fractional crystallisation. The flat REE pattern of the volcanic rocks and their La/Sm (= 0.46 – 1.27) and La/Yb (0.36 – 1.38) ratios suggest that the rocks have experienced minimal fractionation.

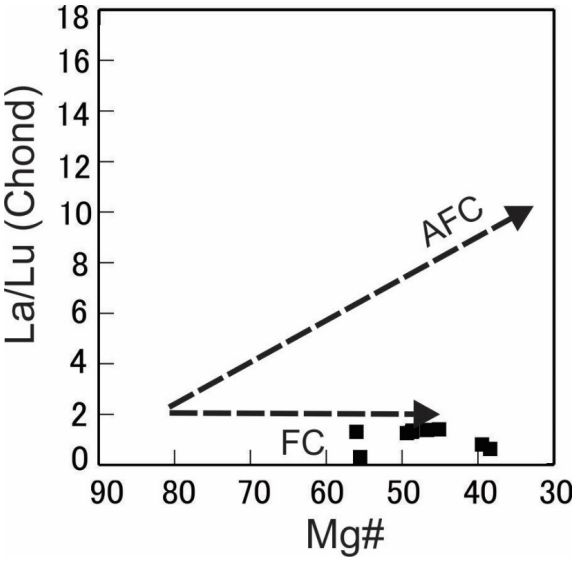

Fig. 8: (La/Lu) chond versus Mg# plot for the rocks (Shervais *et al.*, 2006).

Modelling of magma source, enrichment and contamination

Earlier workers have shown that the elemental ratios such as Th/Yb, Nb/Yb and Ta/Yb emphasize source variations and crustal assimilation as they are mostly independent of fractional crystallization and/or partial melting (Dampare *et al.*, 2008). Basaltic magmas which have been derived from the mantle asthenosphere (Depleted MORB Mantle), the plume asthenosphere or the mantle lithosphere enriched by a small degree of melt from the asthenosphere, often fall within or close to a diagonal mantle array defined by constant Th/Nb and Th/Ta values. Th, rather than Nb, Ta or Yb, is usually entrained in subduction zone components. Source components that have been metasomatised by subduction processes will be enriched in Th relative to Nb or Ta, thereby resulting in higher Th/Yb ratios than Nb/Yb or Ta/Yb. Crustal contamination may also increase Th/Yb values with respect to Nb/Yb or Ta/Yb values, as crustal rocks also contain relatively higher concentrations of Th than Nb and Ta. The volcanic rocks were plotted on the Th/Yb versus Nb/Yb diagram of Pearce (1983), Pearce and Peate (1995) and Pearce (2014; Fig. 9), where they plotted within the mantle array and span the area between N-MORB and E-MORB. This suggests that the volcanic rocks have not experienced any form of contamination, either from the crust or by subducted component.

Johnson and Plank (1999) interpreted the fluid-immobile element Th (e.g., the Th/Nb value) as a proxy for melted and recycled sediment. The Th/Nb ratios for the volcanic rocks span a range of 0.07 to 0.09, which is very low. This also confirms that the volcanic rocks were generated from a mantle source which has not experienced any contribution from melted and recycled sediments, as shown by the Th/Yb and Nb/Yb diagram (Fig. 9). The mantle source of the rocks wasdetermined in the Th–Nb–Ce systematics of oceanic basalts proposed by Saunders *et al.* (1988). According to the authors, the Th–Nb–Ce systematics of oceanic basalts could be visualized in terms of mixing between a depleted MORB source mantle (DMM: relatively high Ce/Nb), a recycled residual slab component processed through the subduction zone (RSC: low Ce/Nb), and a recycled subduction component complementary to RSC (SDC: high Th/Nb).

The rock samples were plotted in a Ce/Nb versus Th/Nb diagram (Fig. 10), following the approach of Kerrich *et al.* (1999). All the samples plotted in the field of E-MORB. This may suggest that the rocks were generated solely from an enriched source in the mantle rather than through enrichment by crustal or subducted material.

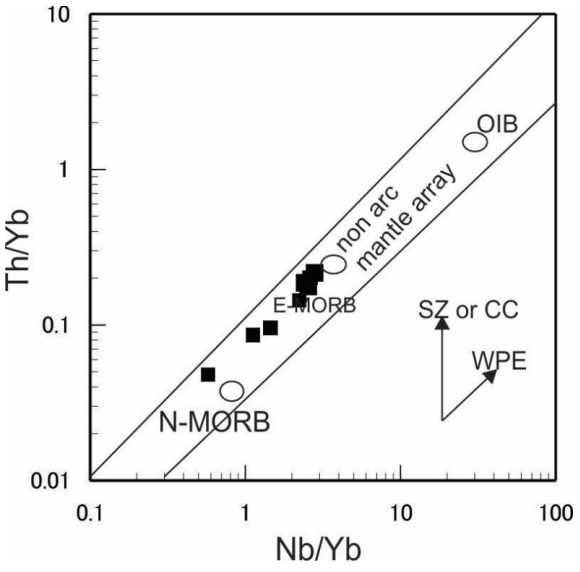

Fig. 9: Th/Yb versus Nb/Yb diagram (after Pearce, 1983; Pearce and Peate, 1995, Pearce, 2014) of the nine (9) sampled rocks illustrating the input of Th from either subduction-zone enrichment or crustal contamination (CC). Samples with very little subducted slab influence lie within or very close to the 'mantle' array defined by the N-MORB array whereas samples influenced by subducted slab flux are displaced from the 'mantle' array to higher Th at a given Nb content than do the former. WPE: within-plate enrichment; SZ: subduction zone flux. N-MORB, E-MORB, and OIB from Sun and McDonough (1989).

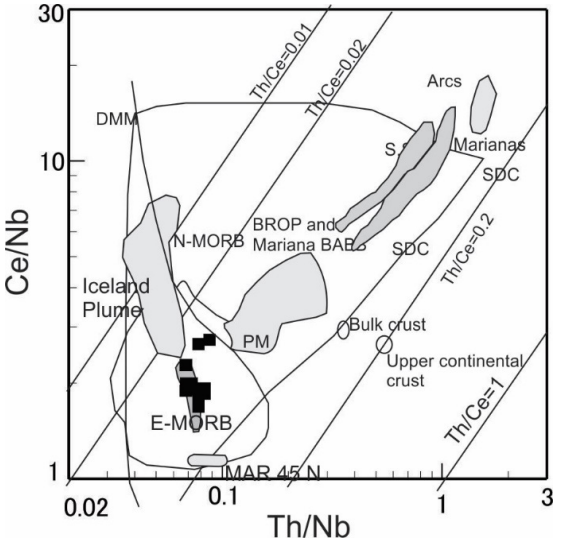

Fig. 10: Plot of Th/Nb vs. Ce/Nb (after Saunders *et al.*, 1988) for the nine (9) sampled basalts. DMM: depleted MORB mantle; E-MORB: enriched mid-ocean ridge basalt; N-MORB: normal mid-ocean ridge basalt; OIB: oceanic island basalt; MAR45◦N: Mid Atlantic Ridge 45◦N; PM: primitive mantle; RSC: recycled residual slab components; SDC: recycled subduction derived component. Lines indicate mixing trajectories between components. Also shown are the compositions of the bulk crust and upper continental crust, as well as the fields of Ontong Java Ocean Plateau (OJOP), Broken Ridge Ocean Plateau (BROP), Back Arc Basin Basalts (BABB) and Iceland Plume basalts. Diagram was adopted from Dampare *et al.* (2008) and references therein.

Evaluation of the source characteristics of the basalts and REE modeling of partial melting.

The composition of the mantle source, residual mineralogies and degree of partial melting that produced the parental magmas of basalts can be determined using REE abundances and ratios (Aldanmaz *et al.*, 2000). The non-modal batch partial melting equations of Shaw (1970) and the REE partition coefficients of McKenzie and O'Nions (1991) were used to model the degree of partial melting for the volcanic rocks. Usually, modelling should involve only the least evolved samples; thus, samples with relatively higher Mg numbers (Mg≥55), elevated Ni and Cr abundances (>100 ppm) and low REE abundances should be used. Although the Mg numbers of the volcanic rocks are relatively low, they were used for the modelling since they have Ni and Cr concentrations (>100 ppm) and low REE abundances. Following Aldanmaz *et al.* (2000), two different reference compositions were used to define the likely mantle array: (1) depleted MORB mantle (DMM) which was assumed to represent the convecting asthenospheric mantle with the composition of the hypothetical depleted MORB source proposed by McKenzie and O'Nions (1991); and (2) Primitive Mantle (PM; Sun and McDonough, 1989) which represents the initial mantle composition prior to MORB formation and depletion.

The contents of the highly incompatible element La and the less incompatible element Sm in basalts can be used to constrain the bulk source compositions, since their concentrations are not influenced much by the variations in either spinel-bearing or garnet-bearing source mineralogies (Aldanmaz *et al.*, 2000; Dampare *et al.*, 2008). From the samples plotted on Fig. 11A, it can be observed that most of the rocks have La concentrations and La/Sm ratios greater than those that could be generated by direct melting of DMM, even when the degree of partial melting is very small (0.1%). It can therefore be inferred that one-stage melting of DMM (or PM) cannot produce magma with incompatible element content similar to those of the basalts. A mantle source that has been enriched in LREE relative to DMM composition is required to produce the basaltic magma since the rocks plot closer to E-MORB (Sun and McDonough, 1989).

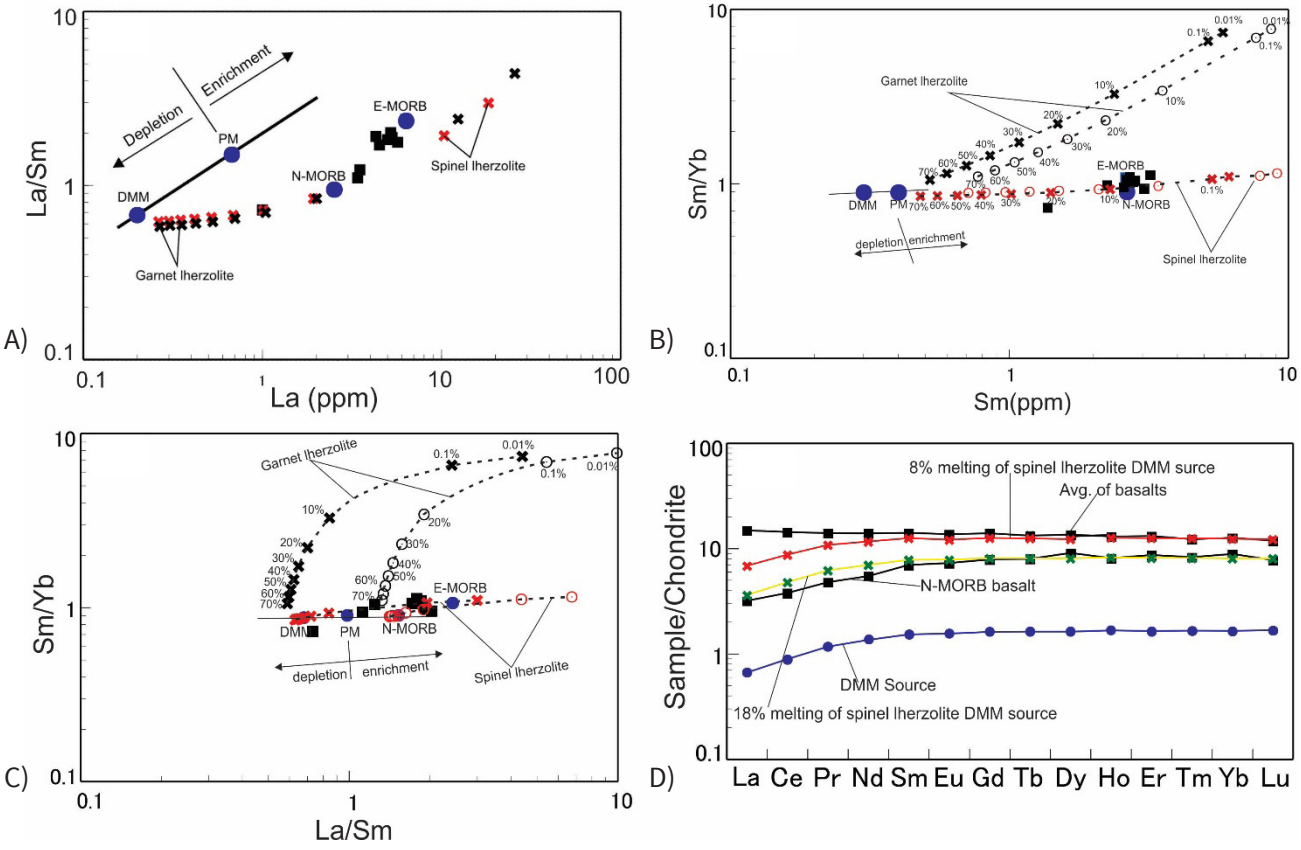

Fig. 11: A) La vs. La/Sm, B) Sm/Yb vs. Sm and C) Sm/Yb vs. La/Sm, D) REE Spectrum modelling for the nine (9) Eastern Buem basalts. Melting curves (lines) for spinel–lherzolite (ol53 + opx27 + cpx17 + sp3) and garnet–peridotite (ol60 + opx20 + cpx10 +gt10) sources with both DMM and PM compositions were drawn following the approach of Aldanmaz *et al.* (2000). Open circles and crosses on the melting curves correspond to degrees of partial melting for a given mantle source. The heavy line represents the mantle array defined by depleted MORB mantle (DMM; McKenzie and O'Nions, 1991) and primitive mantle (PM, Sun and McDonough, 1989) compositions. The N-MORB and E-MORB compositions (Sun and McDonough (1989) have also been shown.

The Sm/Yb ratios can be used to determine the source mineralogy of basaltic rocks, because Yb is compatible with garnet but not with clinopyroxene or spinel. Partial melting of a spinel lherzolite mantle source does not change the Sm/Yb value because both Sm and Yb have similar partition coefficients, whereas it may decrease La/Sm values and Sm contents of the melts as melting progresses. Melts derived from spinel lherzolite sources would be expected to produce melting trends that are sub-parallel to and nearly coincident with a mantle array defined by depleted to enriched source compositions (Fig. 11B and C). However, melts generated by small to moderate degrees of garnet lherzolite melting with residual garnet would have Sm/Yb values significantly higher than Sm/Yb values in the mantle source(s). This will produce melting trends of garnet lherzolite that is displaced from the DMM-PM "mantle" array to higher Sm/Yb. (Aldanmaz *et al.*, 2000; Zhao *et al.*, 2007; Dampare *et al.*, 2008). It is observed from Figs. 11B and C that most of the volcanic rocks plot close to the spinel lherzolite melting curve between 1-10% partial melting, except one N-MORB-like sample that plots close to the 20% partial melting curve. This suggests that the enriched rocks were generated by about 1-10% partial melting of a spinel lherzolite source that is more enriched than DMM and PM since they plot close to E-MORB while the N-MORB-like sample was generated by about 20 % melting of a spinel lherzolite from a DMM source. The high LILE content of the basalts relative to N-MORB and PM is also confirmed by their incompatible multi-element diagram (Fig. 6). The degree of partial melting was also constrained by modeling a spinel lherzolite source for the entire REE spectrum (Fig. 11D). From Fig. 11D it can be confirmed that the average basalt composition of the enriched rocks can be generated by about 8% partial melting of a depleted spinel lherzolite source that has been enriched, since the volcanic rocks are relatively enriched in LREE (La, Ce, Pr, Nd and Sm) compared to DMM. The enrichment processes are mostly considered to be due to either small volume melt fractions or subduction-related fluids (McKenzie, 1989; Anderson, 1994), and are therefore restricted to the non-convecting (lithospheric) mantle. The N-MORB-like sample on the other hand was generated from about 18% partial melting of a spinel lherzolite from the DMM source.

From the REE model therefore it can be inferred that the volcanic rocks may have been generated by a two stage partial melting, the first by the melting of an enriched source to produce the enriched basalts. Continuous melting of the previously enriched source that has been depleted by earlier melt extraction generated the magma that formed the depleted N-MORB-like sample. This mechanism could be attributed to a multi-stage emplacement of basaltic magma within the eastern BSU as a result of the occurrence of volcanic rocks with N-MORB and E-MORB signatures within the BSU. The results compare with recent work by Nude *et al.* (2015), in which the authors inferred multi-stage emplacement for the western Buem volcanic rocks due to their distinct petrography and geochemical characteristics. Hence, taken together, volcanism in the BSU can be considered as episodic with source fractionation at different depths and emplacement at different periods.

According to Winter (2001), depth of origin of plagioclase lherzolite, spinel lherzolite and garnet lherzolite is from 0-40 km, 40-80 km and greater than 80 km respectively. Since it has been inferred that the rocks were generated by partial melting of a spinel lherzolite source, their approximate depth of generation will be from about 40-80 km according to the literature.

Tectonic Setting

Immobile element proxy discrimination diagrams have been employed to complement the patterns observed on incompatible multi-element diagrams for identifying the tectonic setting of the rocks. The volcanic rocks from the Eastern BSU show enriched MORB characteristics as they plot in the field of E-MORB, within plate tholeiitic basalts on the Th-Hf-Nb tectonic discrimination by Wood (1990; Fig. 12A), except for one sample that plots in the field of N-MORB. The E-MORB affinity of the basalts is further confirmed on the Y/La/Nb discrimination diagram of Cabanis and Lecolle (1989; Fig. 12B), where

the basalts plot in the field of anorogenic E-MORB. Shervais (1982) proposed the V–Ti discrimination diagram, on which lava compositions shift from low V/Ti in MORB lavas through intermediate V/Ti in island arc tholeiites (IAT) to high V/Ti in boninites. On this diagram, volcanic arc basalts have Ti/V ratios ranging between 10 and 20, MORB has ratios between 20 and 50, and oceanic island arcs and alkaline basalts between 50 and 100. Most of the volcanic rocks plot in the field of Ocean Floor basalts on this diagram (Fig. 12C), which supports their MORB-like affinity.

In Fig. 5B the volcanic rocks define a similar trend as E-MORB, with slight depletion in LILE but flat HREE pattern. This, therefore, suggests that the volcanic rocks originated from an enriched MORB source within the mantle. Rocks with MORB-like affinity can occur in different tectonic settings, but will have distinct geochemical signatures with which they can be identified. However, since the volcanic rocks do not show geochemical signatures similar to arcs materials, it can be inferred that the volcanic rocks were emplaced in a rifted environment prior to the Pan-African peak collisional event. Nude *et al.* (2015) observed similar geochemical characteristics for the volcanic rocks of western BSU and suggested that the rocks may be related to rifting of a strongly attenuated continental crust that may have preceded the onset of the Pan-African collision. Hence, a similar tectonic setting can be inferred for the eastern Buem volcanic rocks. Considering all these, the volcanic rocks of the BSU may be related to a rifting event and eventual emplacement at the eastern margin of the WAC.

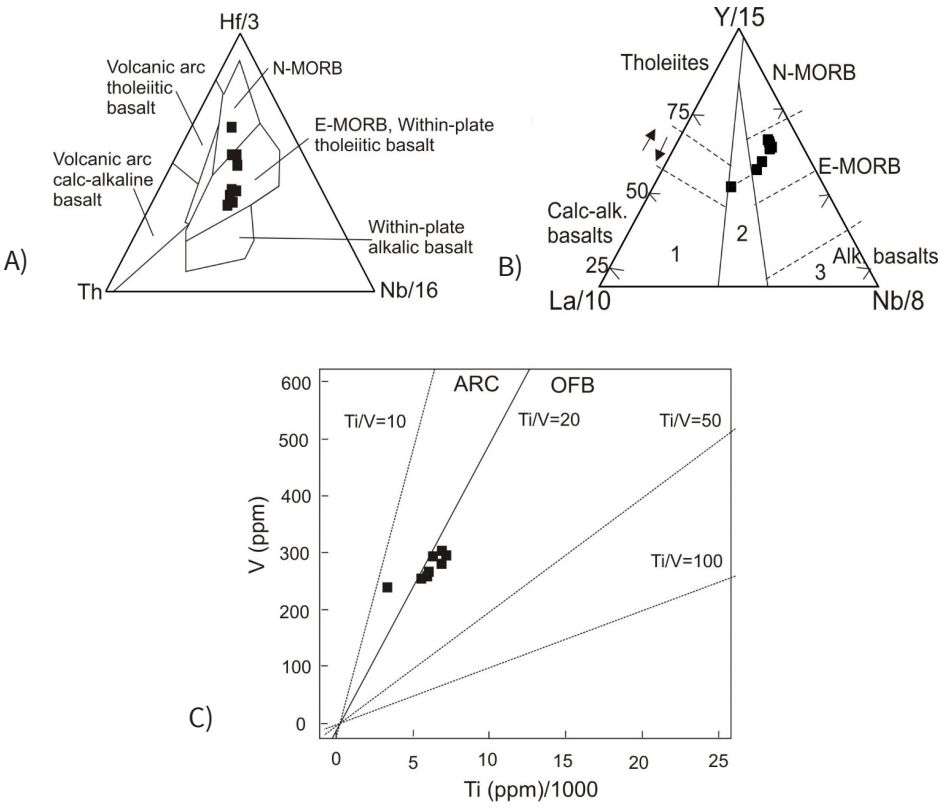

Fig. 12: A) Th–Hf–Nb triangular discrimination diagram of Wood (1990), B) Y/La/Nb discrimination diagram (after Cabanis and Lecolle, 1989); 1: orogenic domains; 2: late- to post-orogenic continental domains; 3: anorogenic domains, C) V versus Ti diagram of Shervais 1982, plotted for the nine (9) Eastern Buem basalts.

Conclusion

The volcanic rocks are sub alkaline and appear to have originated from a low-K tholeiitic magma series by low degree partial melting of an enriched mantle source with possible asthenospheric contribution.

Geochemical characteristics suggest that these volcanic rocks are mantle derived magmas that have an affinity to E-MORB with minimal or no contamination from subducted sediment or crustal component. Major and trace element variation patterns suggest that the rocks were not derived from primary magma but have evolved through fractional crystallisation of clinopyroxene and plagioclase. From trace element modelling, the enriched basalts were generated from about 8-9% melting of a spinel lherzolite from a DMM source that has been enriched, while the typical N-MORB-like sample was generated from about 18% partial melting of spinel lherzolite from a DMM source. The approximate depth of generation of the volcanic rocks is between 40 and 80 km. The eastern Buem volcanic rocks show similar petrographic and geochemical characteristics as the western Buem volcanic rocks, Hence, the two may have formed in the same tectonic environment. Thus, rifting that may have occurred prior to the Pan-African collision and emplacement at the eastern margin of the WAC.

Acknowledgements

We are grateful to the Department of Earth Science, University of Ghana (capacity building project) for funding this research. We would also like to thank the entire teaching and non-teaching staff of the Department of Earth Science (University of Ghana) for their support. We are also grateful to the chief, the Bani family and the people of Jasikan for their hospitality during our stay in the town.

References

Affaton, P., Aguirre, L. & Menot, R.P. (1997). Thermal and geodynamic setting of the Buem volcanic rocks near Tiélé, Northwest Benin, West Africa. *Precambrian Research*, 82, 191–209 and all references therein.

Affaton, P., Sougy, J. & Trompette, R. (1980). The tectono-stratigraphic relationships between the Upper Precambrian and Lower Paleozoic Volta Basin and the Pan-African Dahomeyide Orogenic Belt (West Africa). *American Journal of Science,* 280, 224-248.

Agyei Duodu, J., Loh, G.K., Boamah, K.O., Baba, M., Hirdes, W., Toloczyki, M., & Davis, D.W. (2009). *Geological Map of Ghana 1:1 000 000*. Geological Survey Department of Ghana (GSD).

Aldanmaz, E., Pearce, J.A., Thirlwall, M.F. & Mitchell, J.G. (2000). Petrogenetic evolution of late Cenozoic, post-collision volcanism in western Anatolia, Turkey. *Journal of Volcanology and Geothermal Research*, 102, 67–95.

Anderson, D.L. (1994). The sublithospheric mantle as the source of continental flood basalts; the case against the continental lithosphere and plume head reservoirs. *Earth Planet Science Letter*, 123, 269-280.

Attoh K., Corfu F. & Nude P.M. (2007). U-Pb zircon age of deformed carbonatite and alkaline rocks in the Pan-African Dahomeyide suture zone, West Africa. *Precambrian Research*, 155, 251-260.

Attoh K. & Nude P.M. (2008). Tectonic significance of carbonatite and ultrahigh-pressure rocks in the Pan-African Dahomeyide suture zone, southeastern Ghana. *Geological Society of London*, Special Publication, 297, 217–231.

Blay, P.K. (1991). The Geology of ¼ Field Sheet No. 184, Hohoe N.E.

Cabanis, B. & Lecolle, M. (1989). Le diagramme La/10-Y/15-Nb/8: un outil pour la discrimination des series volcaniques et la mise en evidence des processus de mdlange et/ou de contamination

crustale. C. R. Academy Science Paris 309, 2023-2029.

Dampare, S.B., Shibata, T., Asiedu, D.K., Osae, S. & Banoeng-Yakubo, B. (2008). Geochemistry of Paleoproterozoic metavolcanic rocks from the southern Ashanti volcanic belt, Ghana: Petrogenetic and tectonic setting implications. *Precambrian Research*, 162, 403–423.

Duclaux G., Ménot R.P., Guillot S., Agbossoumondé Y. & Hilairet N. (2006). The mafic layered complex of the Kabyé massif (north Togo and north Benin): Evidence of a Pan-African granulitic continental arc root. *Precambrian Research*, 151, 101-118.

Gaffney, A.M., Nelson, B.K. & Blichert-Toft, J. (2004). Geochemical Constraints on the Role of Oceanic Lithosphere in Intra-Volcano Heterogeneity at West Maui, Hawaii. *Journal of Petrology*, 45 (8), 1663–1687.

Grant, N.K. (1969). The Late Precambrian to early Palaeozoic Pan-African Orogeny in Ghana, "Togo, Dahomey and Nigeria. *Bulletin of Geological Society of America*, 80, 45-55.

Irvine, T.N. & Baragar, W.R.A. (1971). A guide to the chemical classification of the common volcanic rocks. Canadian Journal of Earth Science, 8, 523-548.

Johnson, M.C. & Plank, T. (1999). Dehydration and melting experiments constrain the fate of subducted sediments. *Geochemical Geophysics and Geosystems,* 1. doi: 10.1029/1999GC000014.

Jones, W.B. (1990). The Buem volcanic and associated sedimentary rocks, Ghana: a field and geochemical investigation. *Journal of African Earth Science*, 11, 373-383.

Junner, N.R. (1936). *Volta River District and Togoland under British Mandate.* Gold Coast Geological Survey Annual Report, 1935-36, 10-16.

Junner, N.R. (1940). Geology of the Gold Coast and Western Togoland. *Gold Coast Geological Survey Bulletin*, 11.

Kerrich, R., Polat, A., Wyman, D. & Hollings, P. (1999). Trace element systematics of Mg-to Fe-tholeiite basalt suites of the Superior Province: implication for Archaean mantle reservoirs and greenstone belt genesis. *Lithos* 46, 163–187.

Kwayisi, D. (2014). Petrology and geochemistry of western Buem volcanic rocks, southeastern Ghana: geodynamic setting implication (unpublished master's thesis). University of Ghana, Legon. 140 pp.

Le Maitre, R.W. (1989). *A classification of igneous rocks and glossary of terms.* In: Le Maitre, R.W. (Ed.), Recommendations of the International Union of Geological Sciences, Subcommission on Systematics of Igneous Rocks. Blackwell Science Publication, 193 pp.

McKenzie, D.P. (1989). Some remarks on the movement of small volume melt fractions in the mantle. *Earth Planet Science*, Letter 95, 53-72.

McKenzie, D. & O'Nions, R.K. (1991). Partial melt distribution from inversion of rare earth element concentrations. *Journal of Petrology*, 32, 1021–1091.

Nude, P.M., Kwayisi, D., Taki, N. A., Kutu, J. M., Anani, C. Y., Banoeng-Yakubo, B. & Asiedu, D. K. (2015). Chemical evidence for multi-stage emplacement of western Buem volcanic rocks in the Dahomeyide orogenic belt, Southeastern Ghana, West Africa. Journal of African Earth Science, 112, 314-327.

Pearce, J.A. (1983). *Role of the sub-continental lithosphere in magma genesis at active continental margins*. In: Hawkesworth, C.J., Norry, M.J. (Eds.), Continental Basalts and Mantle Xenoliths. Shiva Publication Limited, Cheshire, UK, 230–249.

Pearce, J.A. (2014). Immobile Element Fingerprinting of Ophiolites. *Elements*, 10, 101–108.

Pearce, J.A. & Peate, D.W. (1995). Tectonic implications of the composition of volcanic arc magmas. *Annual Review Earth Planet Science,* 23, 251–285.

Saunders, A.D., Norry, M.J. & Tarney, J. (1988). Origin of MORB and chemically depleted mantle reservoirs: trace element constraints. *Journal of Petrology.* (Special Lithosphere Issue), 415–445.

Saunders, S.R. (1970). Early Paleozoic Orogeny in Ghana: Foreland Stratigraphy and Structure. *Geological Society of America Bulletin*, 81, 233-240.

Shaw, D.M. (1970). Trace element fractionation during anatexis. Geochim. *Cosmochim. Acta.* 34, 237–243.

Shervais, J.W. (1982). Ti–V plots and the petrogenesis of modern and ophiolitic lavas. *Earth Planet Science. Express*, 59, 101–118.

Shervais, J.W., Vetter, S.K. & Hanan, B.B. (2006). Layered mafic sill complex beneath the eastern Snake River Plain: Evidence from cyclic geochemical variations in basalt. *Geology*, 34 (5), 365–368.

Sun, S. & McDonough, W.F. (1989). Chemical and isotopic systematic of oceanic basalts: implications for mantle composition and processes. In: Saunders, A.D., Norry, M.J. (Eds.), Magmatism in the Ocean Basins. *Geological Society Special Publication,* 42, 313-345.

Taki, N. A. (2014). Petrogenetic evolution of the eastern Buem mafic suite, southeastern Ghana (unpublished master's thesis). University of Ghana, Legon. 96 pp.

Winchester, J.A. & Floyd, P.A. (1977). Geochemical discrimination of different magma series and their differentiation products using immobile elements. *Chemical Geology,* 20, 325–343.

Winter, J. (2001). *Introduction to igneous and metamorphic petrology*. Prentice Hall Upper Saddle River, New Jersey 07458, 796 pages.

Wood, D.A. (1990). The application of a Th–Hf–Ta diagram to problems of tectonomagmatic classification and to establishing the nature of crustal contamination of basaltic lavas of the British Tertiary volcanic province. *Earth Planet Science Letter,* 50, 11–30.

Zhao, J-H, Zhou & M-F. (2007). Geochemistry of Neoproterozoic mafic intrusions in the Panzhihua district (Sichuan Province, SW China): Implications for subduction-related metasomatism in the upper mantle. *Precambrian. Research*, 152, 27–47.

Characterization of Rock Samples from Yale Area of the Upper East Region of Ghana

Samuel A. Atarah[1*] and Gabriel K. Atule[2]

[1] Department of Physics, School of Physical and Mathematical Sciences, University of Ghana, Legon, Accra, Ghana
[2] Sabodala Mining Company, Immeuble 2K Plaza, Route du Meridien President, Almadies, BP 38385, Dakar-Yoff, Senegal
***Corresponding author:** saatarah@ug.edu.gh

ABSTRACT

Quantitative analysis of the mineral and elemental components of rock samples in Yale locality of Ghana, Africa has been done by using the Instrumental Neutron Activation Analysis (INAA) and Atomic Absorption Spectroscopy (AAS). Both the INAA and AAS tests independently showed that the samples were dominated by Mn. INAA showed that across all samples the average composition of Mn was 3322.90 +/-169.60 ppm. Ti (6625.299 +/- 344.68 ppm), Cr (291.27 +/-48.13 ppm) and Cu (16.50 +/- 1.43 ppm) were also revealed by the INAA test on the samples. The results from the AAS test confirmed that Mn was dominant, with an average composition of 6052.22 +/- 2219.03 ppm. The presence of Cr (67.32 +/-72.73 ppm) and Cu (91.61 +/- 69.53 ppm) was also confirmed in the samples from AAS tests. Additionally, Au (1.5 + /- 0.66 ppm) and Co (49.14 +/-15.18ppm) were found, but an AAS test could not be used to confirm the presence of these elements. Gold was detected and estimated for the first time in the rock sample in that area of Ghana. These preliminary results indicate that the Yale area in the Upper East region of Ghana has substantial amounts of Mn, Ti and gold, and signify that the area is a potential mining zone for Mn and Au. The results of the present study add to information on the minerology of the Yale area.

Keywords: INAA, AAS, X-ray Diffraction, Mineral content, Yale Ghana

Introduction

Surface mining is widespread across Ghana today. In some communities, the mining potential has somehow been convincing enough to attract foreign miners, especially from South East Asia. Information on the host rock of any locality is important for mining there. The Minerals Commission, Ghana, does share mining data to inform mining. Other references such as the work of Kesse (Kesse, 1985), also provide important information on the distribution of minerals across the country. Data on mineralogy applicable to the Yale area in the Upper East region was however from sources as old as five decades. For example, Junner *et al.* were among the earliest documented to have sampled and studied the mineralogy of the Yale area (Junner, 1954). Murray's studies (Murray, 1960), which covered a wider area between latitude 10 30′ to 11 00′ and longitude 0 30′ – 1 00′, also included Yale. There are very few available recent reports on work on the area. Yet, whilst collecting data for this study in the Upper East region, artisanal prospecting for gold or gold mining by both native and Asian groups was very active in many communities and this was said to be on the increase. It is fair to state, given the basic manner in which mining was carried out, that such activities are based on no scientific reference data on the mining potential of the area. Availability of data on the composition of the rock in any locality does not only provide information on the mineral prospects of the area, but also gives vital evidence on some minerals which may be deleterious (Petruk, 2000; Chryssoulis, Cabri, & Salter, 1987). Thus, from the environmental or

agricultural perspective, information on characterized ores is important for safety management. This work is partly an attempt to add material to the documentation of the mineralogy of the Yale area.

In conducting this study, the Yale area in the Upper East region of Ghana was thought to be an interesting sampling site for three reasons. 1. There is active prospecting for gold in the region recently, especially in and around the locality, making Yale a good representative sample site for the region. 2. A lot of artisanal miners already had very deep pits in the locality, which suggested that there could be mineral ore in them, and this made sampling from them attractive. 3. The area has a relatively old history of rock sampling but little reference literature. The current study is also an effort to explore the mineralogy of that section of the country by projecting data from a representative sample site.

In this study, the rock samples obtained from selected parts of Yale community were examined to identify their mineral components. Figure 1 is a map of the Yale area indicating spots from which samples where taken. (Spots closer the 2 km apart were marked as one).

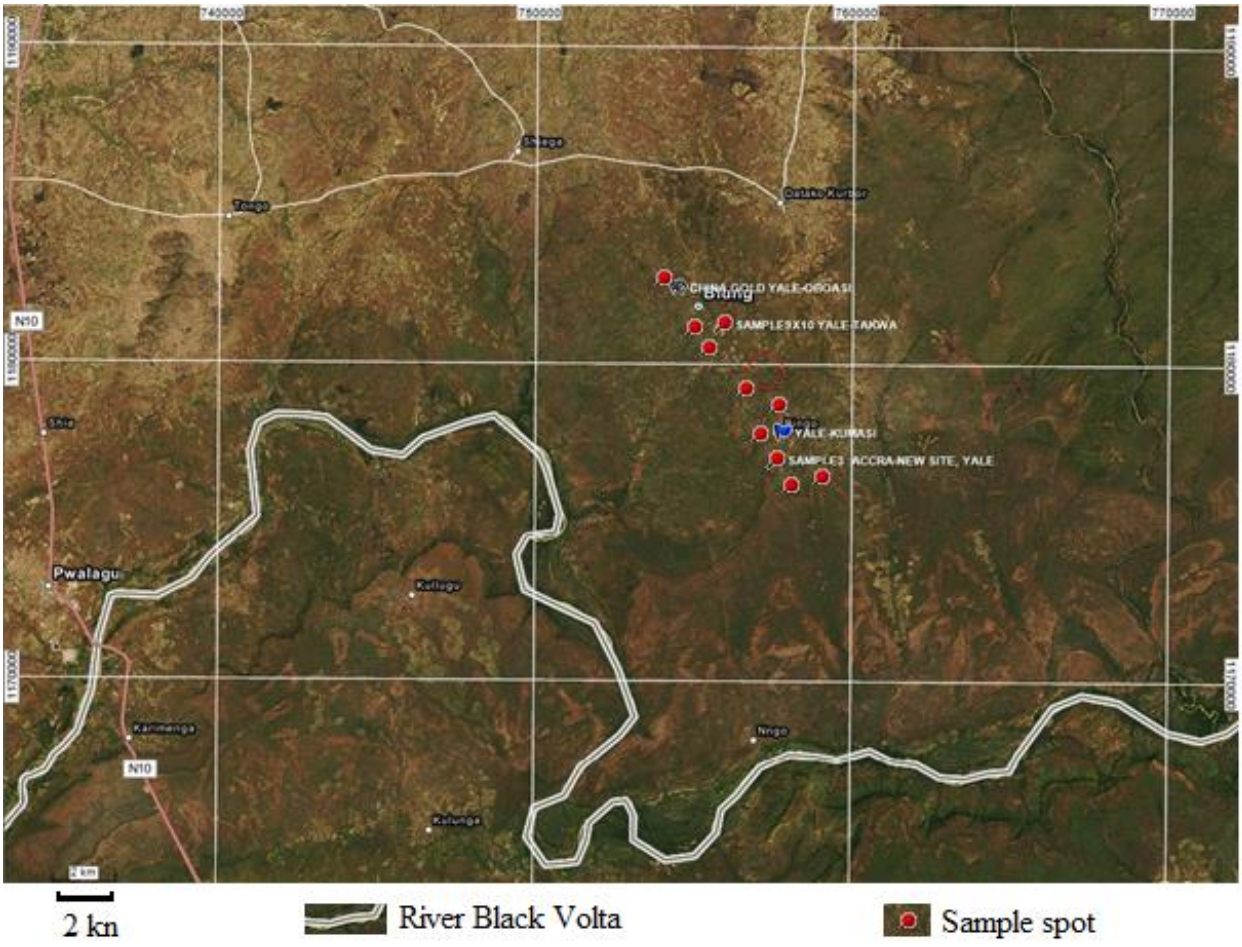

Fig. 1: Map of Yale area showing the sampling sites (Source: www.googlemaps.com)

The work focused on the main components of the rock samples. Identified elements were quantified to enable a discussion of the mining potential of the Yale locality.

A variety of lab methods are available for characterizing suspected ore samples. The methods suggested by the Minerals Commission, Ghana, include gravimetry, fire assay, neutron activation, cyanidation or aqua regia followed by Atomic Absorption and Atomic Emission Spectroscopy (Griffis *et al.*, 2002). Elsewhere (Champion & Huston, 2016), radiogenic techniques have been applied to study the origin of minerals. The focus of this study however is more on establishing the constitution of the sample than on revealing their genesis. Recently, a technique for processing laterite ores using hydrochloric acid and atmospheric pressure leaching has been reported to yield high concentrates of minerals (Guo *et al.*, 2015). However, this technique was not pursued in the current work, as no particular mineral was targeted for purification. It is worth noting that the use of an analysis technique depends on the objective of the analysis (i.e. qualitative, semi-quantitative or quantitative).

In the present work, Instrumental Neutron Activation Analysis (INAA) and Atomic Absorption Spectroscopy (AAS) were applied for characterizing the rock samples collected. The purpose was to determine the chemical composition of the rock samples as well as any relevant compounds. INAA is not often used in mineralogy (Oerter *et al.*, 2007), but it was applied in this work because of its accuracy. AAS is a common and reliable method (Kryazhov, 2014; Shokrollahi, 2017) often applied in mineral characterization or quantification. It was used in this work for qualitive comparison with the INAA results. Results from both high resolution lab methods corroborated each other fairly well.

Experimental methods

Sampling of rocks

Rock samples were taken from eleven random locations within the chosen locality. The locations from which samples were taken are indicated in Fig. 1. To ensure that rock samples were not oxidized or weathered by exposure to air or to water, they were taken from depths of no less than 9 m, and to avoid the possibility of sampling from the same rock, sample spots were more than 1 km apart. Each sample was then sealed in a separate sample bag before being transported to the laboratories for conditioning and experiments. The labels on the samples were kept throughout the analysis, as they appear in the tables below. The procedure adopted for handling the rock samples was necessary in order to avoid cross contamination between samples and was also in accordance with the recommendation of the Minerals Commission (Griffis *et al.*, 2002).

Conditioning of sample for experiments

The samples were then crushed, pulverized and further sieved to at most 50 μm at the National Centre for Nuclear Research Laboratory of the Ghana Atomic Energy Commission (GAEC-NCNR). To avoid sample contamination during grinding, the grinder was used on quartz and cleaned in between samples. A portion of each of the so conditioned samples was taken for separate INAA and AAS analyses.

Atomic Absorption analyses were carried out at the ECOLAB of the Institute for Environment and Sanitation Studies, University of Ghana, using a Perkin Elmer Spectrophotometer. Distilled water was used as blank. Thus distilled water and standard solutions of the element to be tested were used to calibrate the system. To avoid cross contamination, different pipettes were used for solutions of different samples and only glassware was used as containing vessels. The calibration procedure was applied to each of the samples for the test of elements within the test list of the ECOLAB: Mn, Cu, Zn, Pb, Cr, Ni, and Cd. (Although some of these elements could not be tested using INAA, the full result is presented as tested). About 0.5 - 1.0 g of each sample was first digested in nitric acid solution and topped with distilled water to a volume of 100 mL for 36-48 hrs and then irradiated with a lamp consisting of different elements to be tested.

Neutron Activation Analyses for elemental composition and concentration of the samples were done at the Ghana Atomic Energy Commission - National Nuclear Research Centre (GAEC-NCNR) laboratory following the procedure detailed in Atarah (2015) and summarized here. About 100 mg of each sample was weighed (3 replicates each) into irradiation capsules and heat sealed for neutron activation (irradiation). NIST Standard Reference Material 1646a Estuarine Sediment and IAEA Reference Materials SL-3 were similarly weighed as the control samples for calibration. The samples were irradiated in the Ghana Research Reactor-1 (GHARR-1) operated at 15 kW. Thermal neutron flux of 5.0 x 10^{11} n cm^{-2} s^{-1} was used for radiation. The radio activated samples were delayed for a period of 2-5 minutes before counting for identification of short lived radionuclides. For medium lived radionuclides the delay was for a maximum of 24 hours. In either case, counting was done for 10 minutes. Radioactivity measurements of induced radionuclides were performed by a PC-based γ-ray spectrometry set-up, which consisted of an N-type HyperpureGe detector coupled to a computerized multi-channel analyzer via electronic modules.

Results

AAS Data

Fig. 2 shows a calibration graph for Cu. During measurements the spectrometer returns readings in mg/L, representing the amount of test sample in 100 mL. The concentration of the samples was determined in mg/kg (i.e. parts per million, ppm) from:

$$\frac{Q_r(\mu g/mL) \times V_{sol\,(mL)}}{M_{sample\ (g)}} \qquad (1)$$

Where Q_r is the returned reading, V_{sol} is the volume of solution and M_{sample} is the mass of the sample digested.

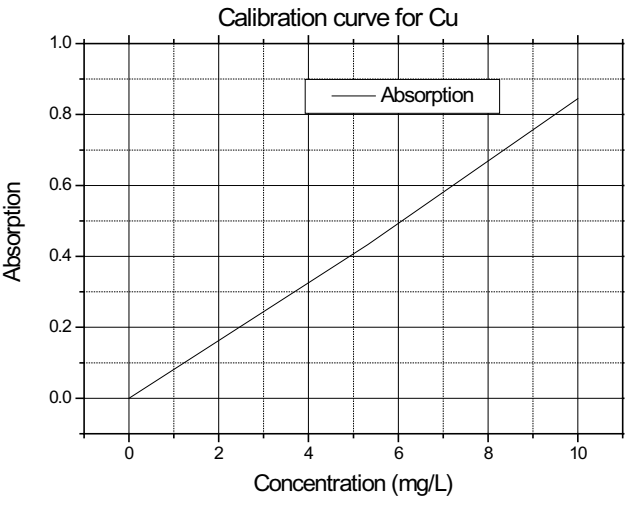

Fig. 2: Calibration graph for measuring Cu concentration in a sample

Fig. 3 shows the composition of the ore samples as obtained from the AAS analysis. The figure shows the percentage composition by weight of the element in the samples. For clear contrast, the data is presented in relative form (percentages) which enables visualization of the dominant components of the rock samples.

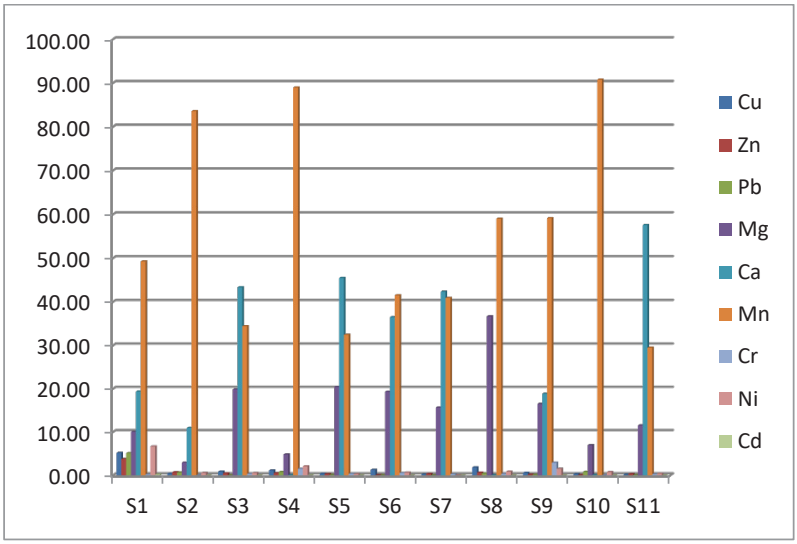

Fig. 3: AAS analysis of elemental composition of the sample, in wt %

Table 1: AAS data showing the elemental composition and concentration (wt %) of the samples

Sample Code	S1	S2	S3	S4	S5	S6	S7	S8	S9	S10	S11
Element	**Proportions of the elements contained in each sample, as revealed by AAS, are shown below in wt%.**										
Cu	5.21	0.43	0.89	1.14	0.40	1.29	0.27	1.84	0.61	0.34	0.22
Zn	3.80	0.73	0.49	0.52	0.34	0.07	0.38	0.62	0.20	0.11	0.34
Pb	5.14	0.68	0.02	0.79	0.13	0.05	0.05	0.46	0.17	0.82	0.10
Mn	49.26	83.60	34.47	88.97	32.50	41.51	40.92	59.01	59.14	90.79	29.51
Cr	0.23	0.04	0.36	1.50	0.37	0.57	0.30	0.36	2.94	0.05	0.28
Ni	6.69	0.58	0.55	2.09	0.32	0.65	0.02	0.87	1.53	0.77	0.41
Cd	0.22	0.01	0.00	0.05	0.02	0.00	0.02	0.03	0.01	0.01	0.00

The data shows that at least 40% of each sample is composed of Mn. The results also show that 10 - 15% of all but three samples (S2, S4 and S10) were composed of Mg. There was no INAA data on Mg to verify these. The rest of the elements that were tested for existed in the samples only in trace from (< 1%). The proportions of the elements (wt %) are also shown in Table 1.

INAA Data

Radionuclides were identified by their specific γ-ray energy using the relative comparator method and ORTEC MAESTRO-32. Fig. 4 shows the energy distribution curve recorded by the detector during counting for sample S9. The main constituent elements are indicated.

The components were identified by the characteristic γ-ray energy distribution of their activated nuclides. A multipurpose γ-ray spectrum analysis software winSPAN-2010 ver. 2.10 (Preece *et al.,* 1999) was used for their concentration analysis. Fig. 5 shows the percentage elemental composition of the samples as obtained by INAA. The composition and proportions of all the samples are presented in Table 2.

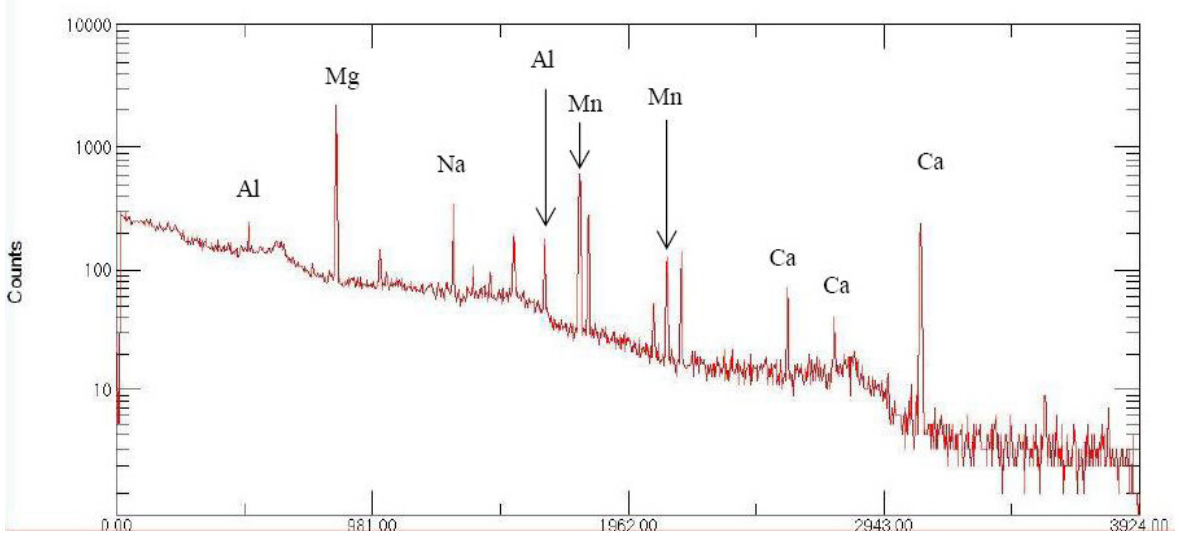

Fig. 4: Energy distribution curve for sample S9

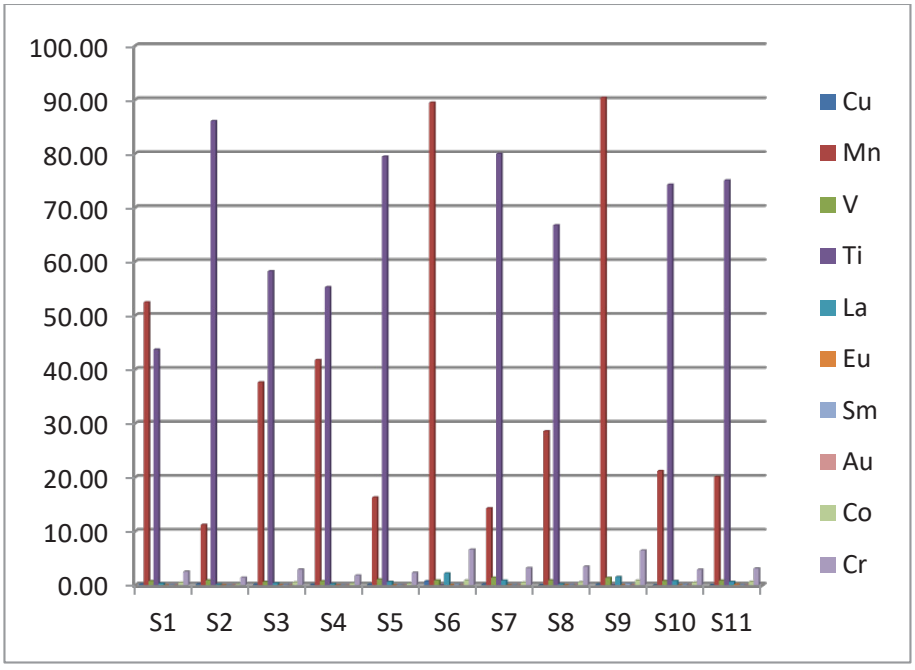

Fig. 5: Elemental composition by wt% of samples as obtained by INAA

Table 2: INAA data showing the elemental composition and their wt% in the samples

Sample code	S1	S2	S3	S4	S5	S6	S7	S8	S9	S10	S11
Element	Amounts of the elements contained in each sample, as revealed by INAA, are shown below in wt%.										
Cu	0.18	0.22	0.17	0.14	0.15	0.76	0.19	0.06	0.19	0.02	0.08
Mn	52.46	11.21	37.63	41.77	16.31	89.47	14.29	28.57	90.42	21.20	20.09
V	0.77	0.92	0.63	0.76	1.09	0.89	1.42	0.93	1.38	0.80	0.86
Ti	43.71	86.06	58.22	55.27	79.47	0.01	80.00	66.74	0.02	74.28	75.06
La	0.33	0.17	0.41	0.23	0.64	2.20	0.87	0.21	1.53	0.79	0.64
Eu	0.00	0.02	0.02	0.01	0.02	0.03	0.01	0.03	0.01	0.01	0.15
Sm	0.10	0.03	0.11	0.01	0.10	0.18	0.04	0.09	0.29	0.14	0.09
Au	0.02	0.01	0.02	0.01	0.01	0.02	0.01	0.01	0.02	0.01	0.02
Co	0.49	0.18	0.55	0.36	0.30	0.90	0.51	0.58	0.87	0.52	0.65
Cr	2.54	1.41	2.92	1.82	2.32	6.63	3.21	3.46	6.45	2.89	3.12

Table 3: INAA data showing the compound composition and their wt% in the samples

Oxides	**MgO**	**Al_2O_3**	**Ca O**	**Na_2O**	**K_2O**	**Fe_2O_3**
			Concentration in percent (%)			
S1	10.44	9.99	1.99	14.23	17.92	8.76
S2	2.38	13.15	2.62	2.51	21.11	7.84
S3	2.77	10.14	0.75	16.99	18.78	6.83
S4	1.27	17.59	0.35	1.68	5.68	6.33
S5	5.85	17.21	2.84	10.9	25.77	6.43
S6	2.6	31.98	1.04	15.51	23.07	7.71
S7	1.52	16.06	1.17	1.12	16.45	6.94
S8	1.87	18.77	1.55	1.73	20.53	6.97
S91	3.13	35.05	0.71	3.34	16.3	6.98
S10	6.45	22.8	0.67	0.1	0.75	6.31
S11	3.99	15.23	0.15	9.81	16.53	6.96

The INAA data also revealed the composition of oxides in the samples as shown in Table 3. As the samples were collected from great depth beneath the surface, these are likely to be stable oxides that were formed at the same time as the rock. Indeed, except for Na, K and Al, the oxides in Table 3 are those of the elements revealed by the AAS study and contained in Fig. 3.

Discussion

AAS

The AAS data shows that Mn is the most dominant element across all the samples. Nearly half of the samples (according the AAS test) consisted of no less than 50 wt % of Mn. The result is in line with the fact that Mn is the most prevalent mineral in rock. The data also shows that Pb, along with Ni, Cd, Zn (as determined by AAS only), Cr, and Cu were all found to be in trace form only. (see also Table 1). Mn was also observed from the INAA data (in Fig. 4) to be in high concentrations in all the samples. The AAS data, showing the dominance of Mn in the samples, is in good agreement with that of the INAA. It must be stated however that as AAS equipment could only test for a limited list of elements, the comparison of data can be deemed incomplete as data on Ti, Au and the rare earth elements was not available from AAS tests. The absence of such data however is not enough to doubt the data, as AAS has been applied for Au characterization in other works (Sighinolfi, 1976).

Instrumental Neutron Activation Analysis

The INAA experimental data is shown in Fig. 6. When examined in detail, it reveals two groups of minerals in terms of their concentrations. The data consisted of a few minerals each in high relative concentrations as shown in Fig. 6 (A). According to the figure, the components that dominated all samples were Ti and Mn, although the data also showed that there were moderate amounts of chromium. The dominance of Mn is totally in agreement with the observation from the AAS data (Fig. 3); however, Ti could not be tested by the latter method.

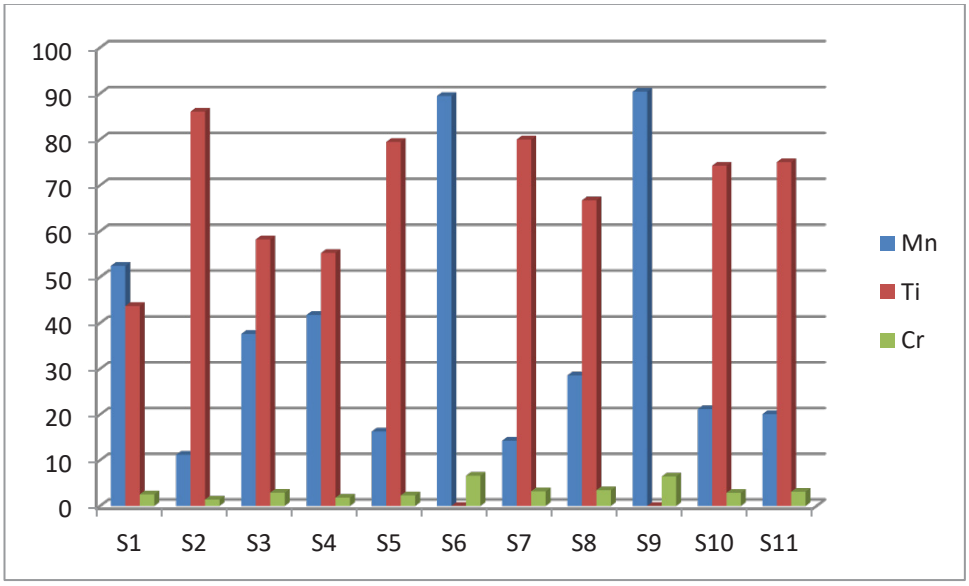

Fig. 6: A) INAA data showing minerals in relative high proportions (up to 90% wt)

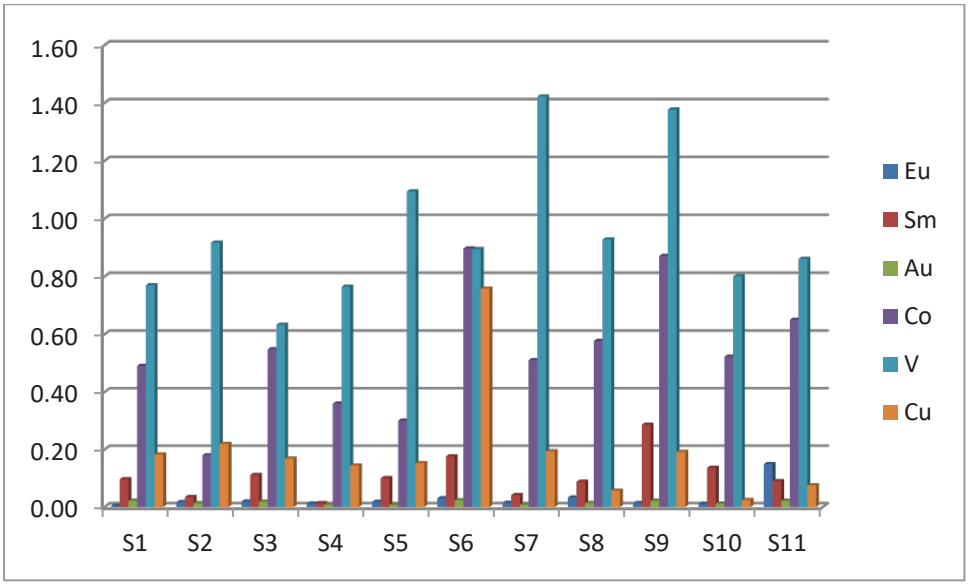

Fig. 6: B) INAA data showing smaller proportions (<1.5 % wt)

The other group of minerals from the INAA data consisted of those in smaller concentrations (< 1.55 wt %) as shown in Fig. 6 (B). These included 'economic' metals Au, Cu and Co as well as rare earth elements such as La, Eu and Sm. The proportions of the economic metals Cu and Au appear to be insignificant, but in absolute terms all samples contained up to 32.6 ppm of Cu. By the data, Au was present up to 2.67 ppm in all samples. Except for Au, the presence of Cu, Cr and Mn in the samples as established by AAS analysis was confirmed by the results from INAA experiments. Between the INAA and AAs tests, a difference in the relative proportions of the content of the samples is observable across the data sets. The trend appears to be a positive correlation, indicating that both qualitatively and quantitatively the components of the samples as characterized were cross confirmed.

In addition to Au and Mn, the data also showed substantial amounts of Co, which are of economic and commercial value. The study also established that Pb and Zn were in minor concentrations in the samples. Indeed, older reports indicate that no significant occurrences of Zn or Pb have been found in the country (Cooper, 1934). The data from the current study validates these earlier reports.

Conclusions

AAS and INAA techniques were applied to quantitatively analyse the mineral and elemental components of rock samples in Yale locality in Ghana. In the limit of each technique the qualitative (content) results were well correlated. INAA and AAS tests independently showed the presence of Mn, Ti, Cr, Ca, Cu, Co and Au. According to the AAS data, Mn accounted for 29 - 59%. The AAS data showed that elements such as Cu, Zn, Pb, Cr, Ni and Cd are each less than 1% of the samples. The INAA data showed that Mn and Ti are the dominant components of all the samples, accounting for 11 – 90% and 43 - 86% of their content respectively (though two samples showed only 0.01 and 0.02% Ti). The data confirmed the presence of Cr (1.4 - 6.6%) and Cu in trace amounts. INAA data also showed that all samples contained 0.67 - 2.67 mg/kg of Au. These are minerals of economic and industrial value whose presence in this locality has never been analysed and documented.

Acknowledgements

The authors are grateful to Mr. Nicholas S. Opata, of the Nuclear Reactor Research Centre at the Ghana Atomic Energy Commission (GAEC) for technical support in neutron activation experiments and to Prof. Shilo Osae (Director, National Nuclear Research Institute, GAEC) for providing the Centre's resources for this work. Mr. Prince Owusu of the Institute for Environmental & Sanitation Studies, University of Ghana, kindly provided technical assistance in atomic absorption spectroscopy experiments.

References

Atarah, S. A., Atule, G. K., Egblewogbe, M. N. Y,. Kuditcher, A. (2015). Instrumental analysis and characterization of minneral ores from Yale, Upper Earst Region, Ghana. *J. Appl. Sc. Tech, 20*(1 & 2), 62-68.

Champion, D. C., & Huston, D. L. (2016). Radiogenic isotopes, ore deposits and metallogenic terranes: Novel approaches based on regional isotopic maps and the mineral systems concept. *Ore Geology Reviews, 76*, 229-256.

Chryssoulis, S. L., Cabri, L. J., & Salter, R. S. (1987). Direct determination of "invisible" gold in refractory sulfide ores. In R. S. Salter, D. M. Wysouzil & G. M. McDonald (Eds.), *Proceedings of the International Symposium on Gold Metallurgy* (pp. 234-244). New York: Pergamon Press.

Cooper, W. G. G. (1934). Zinc blende and galena in quartz reef at Chichiwere prospect, west of Kumasi. *Annual report of the Director of Geological Survey for the period 1933-34* (pp. 16).

Griffis, R. J., Barning, K., Agezo, F. L., & Akosah, F. K. (2002). *Gold Deposits of Ghana*. Ontario, Canada: Gandalf Graphics Ltd.

Guo, Q., Qu, J., Han, B., Zhang, P., Song, Y., & Qi, T. (2015). Innovative technology for processing saprolitic laterite ores by hydrochloric acid atmospheric pressure leaching. *Minerals Engineering, 71*, 1 - 6.

Junner, N. R. (1954). *Notes on the classification of the Precambrian of West Africa*. Paper presented at the XIX Inter. Geol. Cong., Algiers. 20, 114-117

Kesse, G. O. (1985). *The mineral and rock resources of Ghana*. Rotterdam: A.A Balkema.

Kryazhov, A., Panova, S., Kolpakova, N., Pshenichkin, A. (2014). Determination of Au, Pb, Ni and Co in Mineral Raw Materials by Atomic Absorption Spectroscopy with Graphite Furnace. *Procedia Chemistry* 10, 437-440.

Murray, R. J. (1960). The Geology of the "Zuarungu" 1/2° Field Sheet Lattitude 10° 30' - 11° 00' Longitude 0° 30' - 1° 00' *Geological Survey Bulletin* (pp. 117). Accra: Ghana Geological Survey.

Oerter, E. J., Brimhall Jr, G. H., Redmond, J., & Walker, B. (2007). A method for quantitative pyrite abundance in mine rock piles by powder X-ray diffraction and Rietveld refinement. *Applied Geochemistry, 22*(12), 2907-2925. doi: http://dx.doi.org/10.1016/j.apgeochem.2007.08.002.

Petruk, W. (2000). *Applied Mineralogy in the Mining Industry*. Amsterdam: Elsevier, BV.

Preece, R. D., Briggs, M. S., Mallozzi, R. S., & Brock, M. N. (1999). WINGSPAN: A WINdows Gamma-ray SPectral Analysis program. *Astrophysics Source Code Library, record ascl:9910.007*.

Sighinolfi, G.P., Santos, A.M. (1976). Determination of gold in geological samples at part per milliard levels by flameless atomic-absorption spectroscopy. *Mikrochim. Acta,* 2, 33-40.

Shokrollahi, A., Masoud Gohari (2017), Flame atomic absorption determination of zirconium in glass and refractory bricks after coprecipitation with aluminium hydroxide. *Journal of Taibah University for Science*, 11 (4), 540-547

Numerical Analysis of Graphene Cladded Optical Fibre

Ferdinand A. Katsriku[1]*, Grace G. Yamoah[1] and J-D Abdulai[1]
[1]Department of Computer Science, University of Ghana
***Corresponding author:** fkatsriku@ug.edu.gh

ABSTRACT

Graphene has been hailed as a material with extraordinary properties capable of transforming many scientific and industrial fields. In this work, the vector H-field finite element method is used in the characterization of a graphene cladded fibre. Results are presented on the modal analysis of various types of graphene cladded optical fibres. Such fibres may find use as nonlinear elements in linear pulse compression schemes for ultra fast pulse generation.

Keywords: Graphene, FEM, vector H-field, waveguide, optical fibre

Introduction

Integrated all-optical devices will be fundamental in future communication systems. As an essential component of communication systems, these optical devices will act as switches, multiplexers, modulators, reflectors, etc. Research has shown that by perfectly reflecting the waves over the frequency range of interest, or confining propagation in a specified direction and controlling the optical properties of the material, high-speed data transmission could be achieved. Photonic crystal (PhC) technology has made it possible to manipulate light in a way that is not feasible with conventional optical technology. The last two decades has seen tremendous advances in the development of femtosecond laser systems. In particular, optical pulses with temporal widths of a few hundredths of a second or at most a few picoseconds are predicted to be central to ultra fast communications systems and will find application in many domains, including biomedical applications such as optical coherence tomography, laser eye surgery, metallurgy, chemistry, optical signal processing, sensing and terahertz (THz) wave generation.

Recently a new material "graphene", which is an allotrope of carbon, has been investigated and proven to be an optoelectronic material with excellent parameters, namely its chemical, magnetic, thermal and electrical properties. Graphene is a single layer 2-D atomic crystal of carbon with a hexagonal honeycomb structure. Studies have found that a graphene-integrated medium is amenable to convenient tuning of its electronic and optical properties by varying the applied voltage. This property is the prime requirement for an optical waveguide material, and it has spurred a spate of activities within the research community to undertake a study of graphene in the optical waveguide domain. It has been suggested that graphene could be used as saturable absorber in femtosecond laser systems (Bonaccorso *et al.*, 2011; Pumera, 2011; Sun *et al.*, 2010; Zhang *et al.*, 2009; Bao *et al.*, 2009). The literature on graphene has grown quite rapidly in recent years, an indication of the level of interest in this new material within the research community. Graphene has been proposed for use in the design of electro-optic modulators, waveguides, transistors and integrated circuits, and recently it has been suggested as a saturable absorber in a femtosecond pulse generation scheme (Bonaccorso *et al.*, 2011) in order to achieve mode locking. The use of graphene as a saturable absorber offers the possibility of building more compact laser systems. In a saturable absorber, the absorption of light will decrease as the intensity of

the laser beam increases. Until recently, mode-locking was achieved by the use of semiconductor saturable absorber mirrors. However, their low damage threshold, limitations on design flexibility and the carrier relaxation time which limits the pulse width have necessitated the search for new systems. The operation of such mode locked lasers is very complicated, as all the parameters associated with its operation are interdependent on each other, so that minor changes in one parameter could lead to major changes in the laser output (Inoue and Namiki, 2008). Another well-established method for obtaining ultra-short pulses is to use a pulse compression within an optical fibre. This method is applicable to any continuous wave laser source and is more stable because it is based on the intrinsic properties of the travelling wave within the fibre. These methods may suffer from large pedestal and require the use of nonlinear elements, usually dispersion shifted fibre of several hundred metres or even kilometres length of fibre.

Liu *et al.* (2011) demonstrated a broadband, high-speed, waveguide-integrated electro-absorption modulator based on monolayer graphene, paving the way for graphene-based nonlinear photonics. It has high electron mobility and optical transparency, in addition to flexibility, robustness and environmental stability (Bonaccorso *et al.*, 2011). It is found that to fully utilize graphene's remarkable optical properties, it needs to be integrated into planar photonic systems (Li *et al.*, 2012). Studies have shown that the behavior of light in graphene could be tuned electrically, and the converse may also be feasible (Keilmann, 2012). Since light is confined to nanocables with dimensions of a millionth of a millimeter, switching times could be reduced to less than picoseconds (Keilmann, 2012). Thus, integrating graphene with an optical waveguide can greatly increase the interaction length through the coupling between evanescent waves and graphene.

Following this possibility, a team of researchers in UC Berkeley built a tiny optical device that uses graphene to switch light on and off in a graphene/silicon hybrid waveguide structure (Liu *et al.*, 2011). This switching ability is the fundamental characteristic of a network modulator, which controls the speed at which data packets are transmitted. The faster the data pulses are sent out, the greater the volume of information that can be sent (Liu *et al.*, 2011). The speed of data transmission depends on how quickly the modulator can pulse light. Further, studies have shown that when the Fermi level of graphene is tuned, the optical absorption of graphene can be altered. Operating at 1.2 GHz without any temperature controller, such a graphene-integrated modulator has a broad bandwidth (from 1.3 to 1.6 μm) and a small footprint (~25 μm^2) (Liu *et al.*, 2011). The research found that a graphene modulator achieved a modulation speed of 1 GHz and could theoretically reach as high as 500 GHz (500 billion cycles a second) (Liu *et al.*, 2011).

A review of current literature shows that research on graphene is mainly focused on experimental evaluation. The ability to predict the performance of a device before its practical fabrication can be a key factor in the development of new and innovative technologies. In this regard, modeling and simulating a device by the use of a numerical method to predict its performance can lead to reduction in time, cost and constraints involved in experimentation as well as performance optimization. Numerical methods have experienced a resurgence expansion in all fields of engineering due to the exponential growth in the computational power currently available. Recently, results from the numerical characterization of a graphene based terahertz device have been reported. (Themistos *et al.*, 2014).

In this present work, we present results on the modal numerical analysis of various types of graphene cladded optical fibres. Such fibres may find use as nonlinear elements in linear pulse compression schemes.

Numerical Formulation

The key ideas in the finite element method are to:

- discretize the domain under investigation into sub-domains or elements. The accuracy of the method depends on the level of discretization. It is recommended that more elements be used in areas where the field is thought to have steep variations. It is also not advisable to use elements across physical boundaries or interfaces. For symmetrical domains, the mesh should follow the same type of symmetry.
- the functionals for which the variational principle should be applied for the elements are then derived. In deciding on the interpolation function, certain continuity conditions must be satisfied by the interpolation function across inter-element boundaries. These requirements are normally obvious from a physical examination of the problem. It is however also necessary that the function is an admissible member of the Ritz and Galerkin methods. It follows that the polynomial function must remain unchanged under a linear transformation from one co-ordinate system to the other.
- assemble all the element contributions to form a global matrix.
- solve the system of equations that is obtained, in this case a matrix equation.

Hence, instead of differential equations for the system under investigation, variational expressions are derived and the piecewise continuous function approximated by a piecewise continuous polynomial within each element. From the equivalent discretized model contribution from each element, an overall system is assembled. This can be regarded as a sub-class of the Ritz-Galerkin method in which the trial functions are replaced with polynomial functions.

Given the following Helmholtz equation

$$\nabla^2\phi + k^2\phi = 0 \qquad 1$$

as the governing equation in a waveguide problem, defined within the domain Ω, where ϕ is the electric or magnetic field component, ∇^2 is a Laplacian operator defined as

$$\nabla^2 = \frac{\partial^2}{\partial x^2} + \frac{\partial^2}{\partial y^2} + \frac{\partial^2}{\partial z^2} \qquad 2$$

and k^2 is a constant related to frequency, and given also that Γ_f and Γ_n are boundaries within the said domain, then the following boundary conditions may be defined:

$\phi = \hat{\phi}$ on the boundary Γ_f (Dirichlet boundary condition) 3

$\frac{\partial\phi}{\partial n} = \boldsymbol{n}\cdot\nabla\phi = \hat{\psi}$ on the boundary Γ_n (Neumann boundary condition) 4

where $\boldsymbol{n}$ is the outward normal unit vector. The gradient operator is defined by the following matrix differential operator

$$\nabla = \begin{bmatrix} \partial/\partial x \\ \partial/\partial y \\ \partial/\partial z \end{bmatrix} \qquad 5$$

in the Cartesian system of co-ordinates. Taking into consideration the stated boundary conditions, the functional for equation (1) could be written as (Koshiba, 1990)

$$F = \frac{1}{2}\iiint_{\Omega}\left[(\nabla\phi)^2 - k^2\phi^2\right]d\Omega - \int_{\Gamma_n}\phi\hat{\psi}\,d\Gamma \qquad 6$$

The stationary requirement of the above functional, $\delta F = 0$, coincides with the governing equation of the problem. The Neumann boundary condition is automatically satisfied in the variational procedure; as such it is referred to as the natural boundary condition. The Dirichlet boundary condition however needs to be imposed, and is therefore called the forced boundary condition. The functional for each of the elements of the region could then be written as

$$F_e = \frac{1}{2}\iiint_{e}\left[(\nabla\phi)^2 - k^2\phi^2\right]d\Omega - \int_{\Gamma_e}\phi\hat{\psi}\,d\Gamma \qquad 7$$

The functional for the whole of the domain can then be regarded as a summation of the element functions

$$F = \sum_e F_e \qquad 8$$

For the n nodes within each element, the field ϕ can be approximated as follows

$$\phi = \sum_{i=1}^{n} N_i \, \phi_i \qquad 9$$

where ϕ_i is the i^{th} nodal parameter of the element e and N_i is the interpolation or shape function. The above equation could be written in matrix form as follows:

$$\phi = \{N\}^T \{\phi\}_e \qquad 10$$

where the component of the vector $\{\phi\}_e$ is ϕ_i and that of the vector $\{N\}^T$ is the interpolation function N_i. T denotes a transpose, $\{\cdot\}$ and $\{\cdot\}^T$ denote a column and row vector respectively.

For convergence of the solution, the shape function N_i must satisfy certain conditions when the functional contains first order derivatives:

- the variable ϕ and its derivatives must include constant terms
- the variable ϕ must be continuous at the interface of two adjacent elements.

The first of the two conditions is also known as the completeness condition and is simple to satisfy provided complete polynomial expressions are used in each element. The second of the two conditions is called the compatibility condition.

For the accurate characterisation of general waveguides, a vector formulation with at least two field components is required. There are two main types of the full vector formulations, namely the **E**-field and **H**-field. The vector **E**-field approach was first applied by English and Young (1971). This formulation is suitable for generally anisotropic and loss-less problems. The natural boundary condition corresponds to a magnetic wall and as such it is essential to enforce the electric wall as the boundary condition (**n**x**E**=0). Such a condition is quite difficult to impose for an irregular structure. It also requires an additional integral to ensure the continuity of the fields at the dielectric interfaces. The **H**-field formulation, on the other hand, has as its natural boundary condition the electric wall, and the magnetic field is continuous everywhere. As such, it is suitable for dielectric waveguide problems, as no boundary conditions need to be imposed. This formulation is given as

$$\omega^2 = \frac{\int (\nabla \times \mathbf{H})^* \cdot \hat{\varepsilon}^{-1} \cdot (\nabla \times \mathbf{H}) d\Omega}{\int \mathbf{H}^* \cdot \mu^{-1} \cdot \mathbf{H} d\Omega} \qquad 11$$

The above formulation leads to non-physical or spurious solutions since the divergence condition $\nabla \cdot \mathbf{H} = 0$ is not satisfied. Various methods exist for detecting these spurious modes. A simple way is to examine the field profiles: since these modes are characterised by inconsistency and a random variation of the field, they are easy to identify. The mathematical idea underpinning the physical solution is that the condition $\nabla \cdot \mathbf{H} = 0$ is obeyed by the eigenvector. By calculating $\nabla \cdot \mathbf{H}$ for each eigenvector, it is possible to identify the true solutions from the spurious ones. The objective, however, is not simply to detect these modes, but to eliminate them or at least suppress them. The penalty-function method (Rahman and Davies, 1984) is one of the best established methods for eliminating these spurious solutions. The method includes an additional term α, the penalty term, a dimensionless number in the variational formulation, which now is written as:

$$\omega^2 = \frac{\int (\nabla \times \mathrm{H})^* \hat{\varepsilon}^{-1}(x,y)(\nabla \times \mathrm{H}) d\Omega + \alpha \int (\nabla \cdot \mathrm{H})^* (\nabla \cdot \mathrm{H}) d\Omega}{\int \mathrm{H}^* \cdot \hat{\mu} \cdot \mathrm{H} d\Omega} \qquad 12$$

In the above α is a dimensionless penalty term used to compensate for the divergence of the H field. ω defines the angular frequency, and the vector magnetic field at the various nodal points is defined through H. Equation (12) may be minimised with respect to the H field in the

various axial directions to yield a stationary solution, as in Katsriku (2000):

$$[A]\{x\} - \omega^2[B]\{x\} = 0 \qquad 13$$

As in [23], $[\square]$ is a Hermitian matrix of the complex type, $[B]$ is a positive definite real symmetric matrix, ω^2 and $\{x\}$ represent the eigenvalue and eigenvector respectively. Equation (13) can be solved using any standard matrix routine to obtain the field values at the nodes. In this work, required routines were developed using Fortran language.

Numerical Results and Discussion

The two configurations of an optical fibre considered are shown diagrammatically in Fig. 1A and Fig. 1B. In one of the configurations, Fig. 1A, the core of the fibre is cladded with graphene as the outer layer. In the second configuration, Fig. 1B, the graphene is sandwiched between an inner fibre core and an outer fibre cladding. In the simulations, the number of layers of the graphene was either one or two.

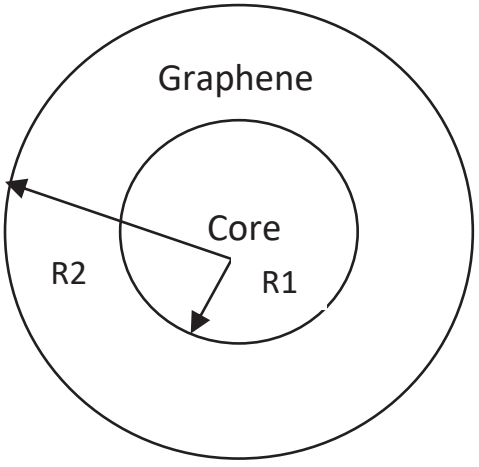

Fig. 1: A) A graphene cladded fibre with no outer cladding

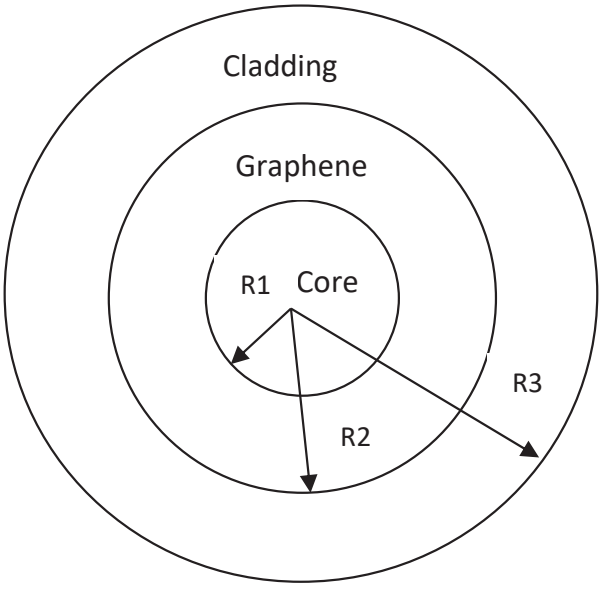

Fig. 1: B) Showing graphene sandwiched between the core and the cladding

In the simulations, the refractive index of the core region was assumed to be 1.49 and the complex refractive index of the graphene region is taken to be 3.51-i14.0 (Themistos *et al.*, 2014). A key issue with numerical simulation involving graphene is its atomic dimension, 3.5 angstrons, which is a thousandth smaller than the other regions. The numerical stability of the solutions was therefore initially tested and the results are depicted in Fig. 2.

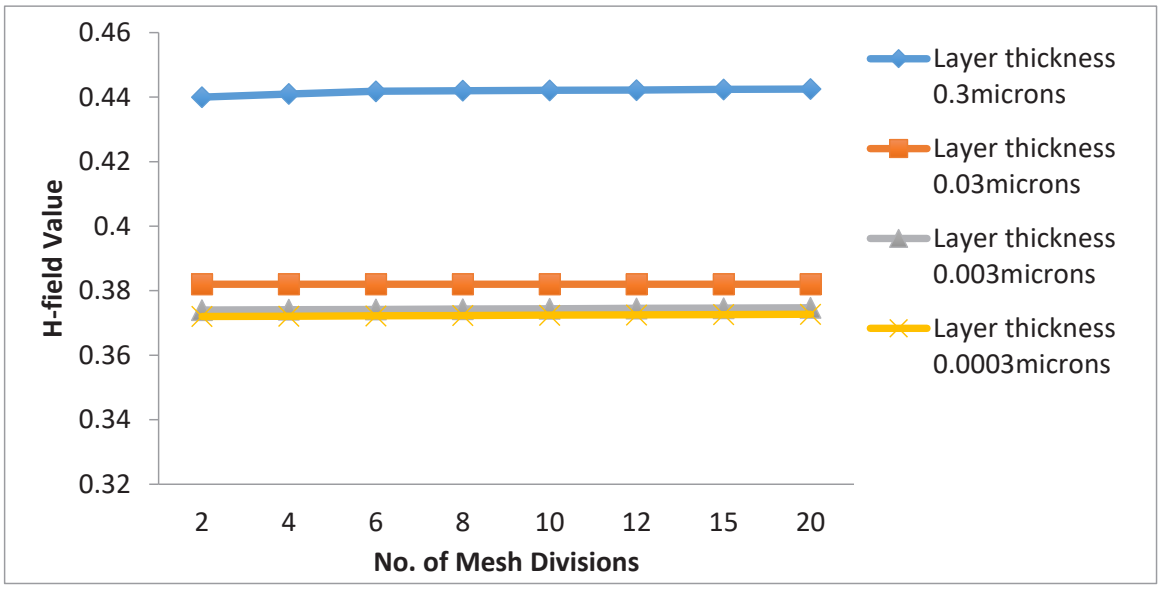

Fig. 2: Showing the stability of the numerical solution as mesh size is varied

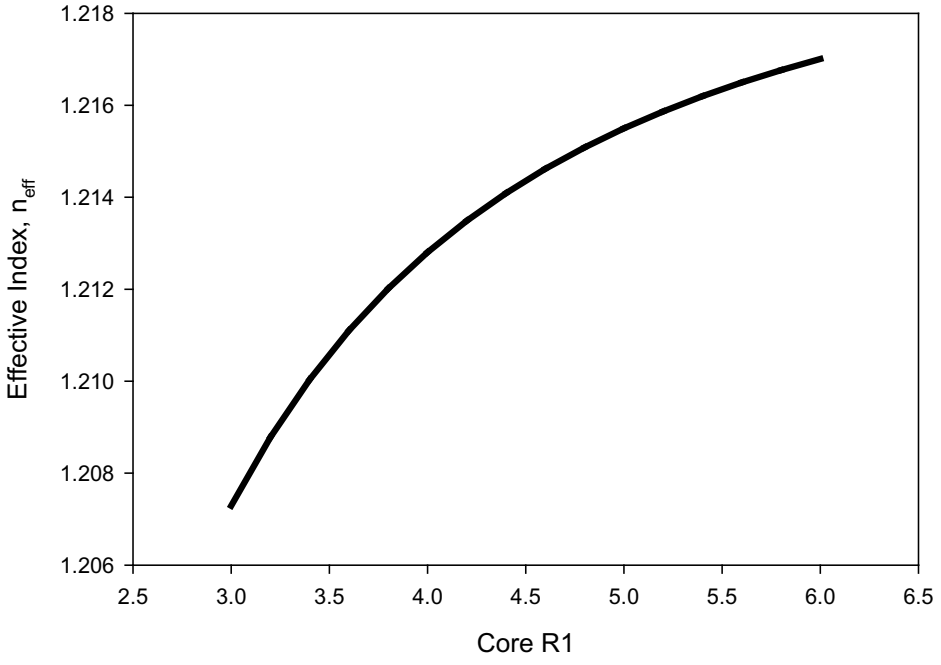

Fig. 3: Showing the dependence of the effective index on the core radius of the fibre

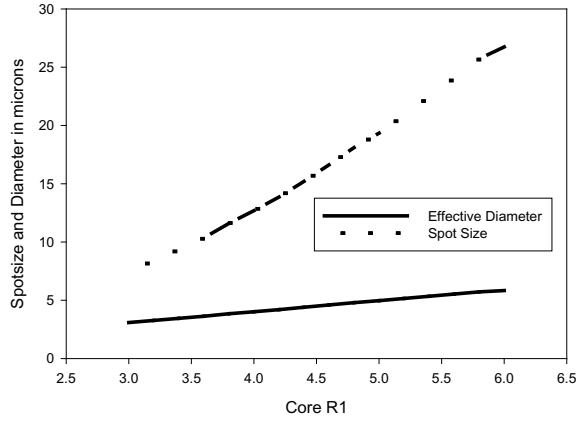

Fig. 4: A) Showing the dependence of the spot size and effective diameter on the width of the fibre core

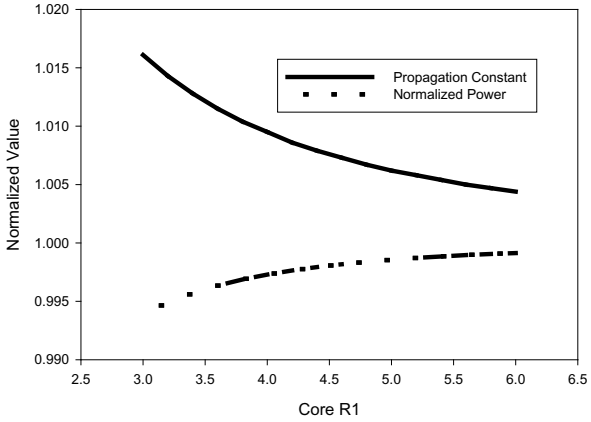

Fig. 4: B) Showing the dependence of the normalized values of power and propagation constant on core size

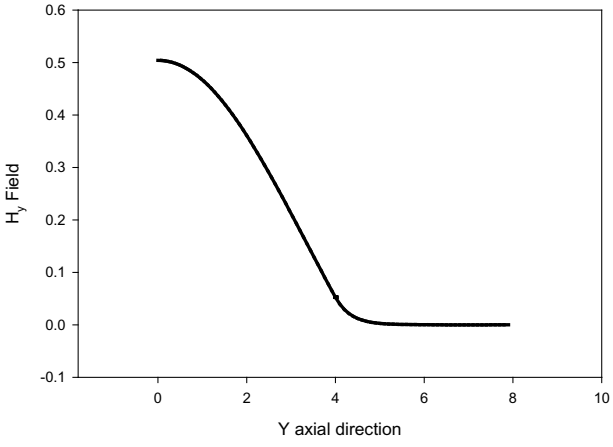

Fig. 5: A) H_y Field profile in the Y-axial direction

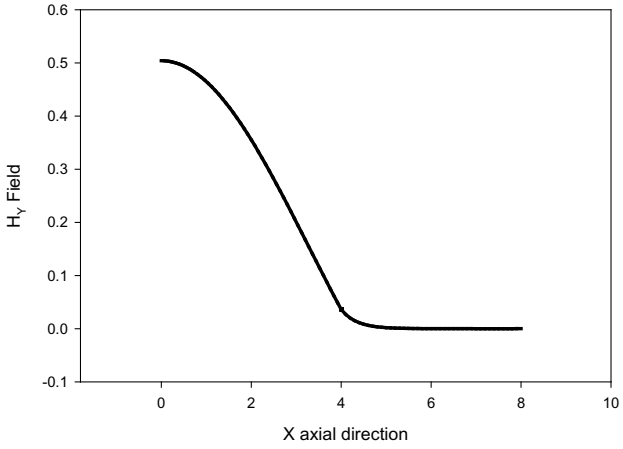

Fig. 5: B) H_y Field profile in the X-axial direction

Hypothetically large widths were chosen equivalent to a thousand layers, hundred layers, ten layers and a single layer of graphene. As can be seen, the results are numerically stable with increasing mesh divisions. In Fig. 3 shows the dependence of the effective index of the fundamental Hy mode of the fibre on the radius of the core dimension. In this, it is assumed that there is no outer cladding, i.e. the configuration of Fig. 1A is used. In Fig. 4A it is seen that as the fibre core is increased, the spot size and the width also increase. Fig. 4B shows the normalized values of power and propagation constant for varying core dimension. It can be seen that when the dimension of the fibre core is increased power also increases whilst the propagation constant decreases.

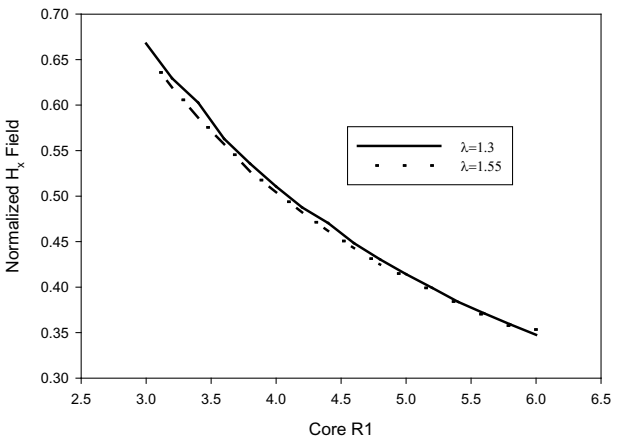

Fig. 6: Showing the normalized field profile as a function of the core radius

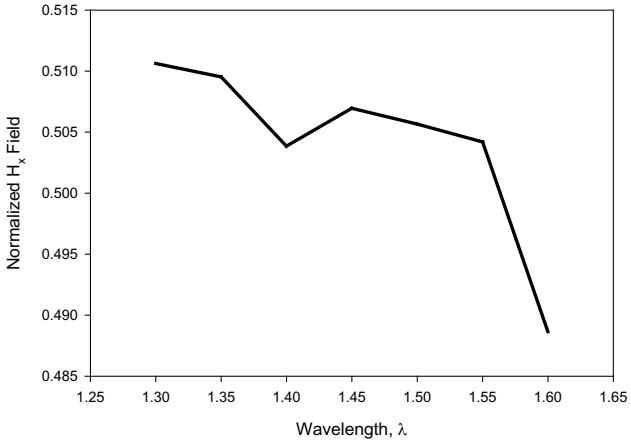

Fig. 7: Normalized H_y Field profile as a function of wavelength

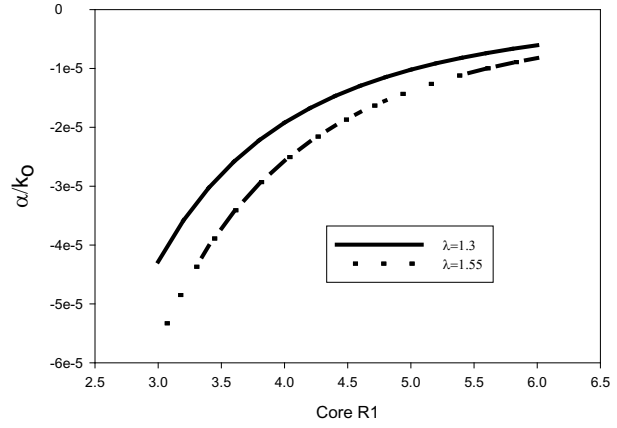

Fig. 8: A) Loss factor as a function of core radius at two different wavelengths

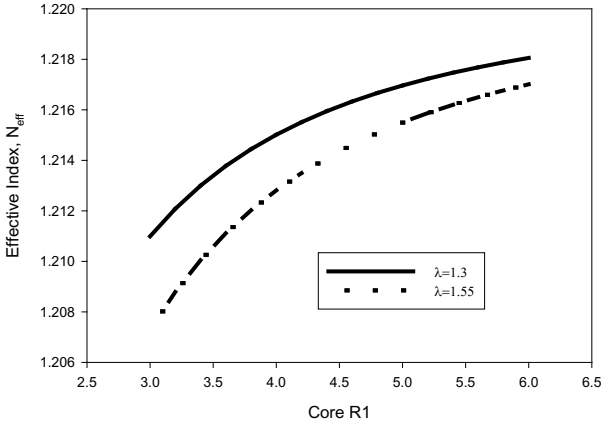

Fig. 8: B) Effective index as a function of core radius at two different wavelengths

Fig. 5 shows the profile of the field in both the x and y axial directions. As can be observed, a symmetrical profile is present in all directions. Such a profile ensures the integrity of the field. Figure 6 shows how the normalized field varies with the core radius of the fibre for two different wavelengths of interest. Fig. 7 on the other hand shows the dependence of the normalized Hx field profile on wavelength. It may be observed that the graph does not show a smooth dependence with sharp transitions. This may indicate that the field profiles are not uniformly confined at the various frequencies and should inform the design process. In Fig**.** 8 is shown the loss factor (Fig**.** 8A) and the effective index (Fig**.** 8B) for two different wavelengths as function of core radius. A parameter of interest is how the propagation constant and effective index will vary with wavelength. This is shown in Fig. 9. Fig. 9A shows the normalized propagation constant as a function of wavelength whilst Fig**.** 9B shows the effective index as a function of wavelength.

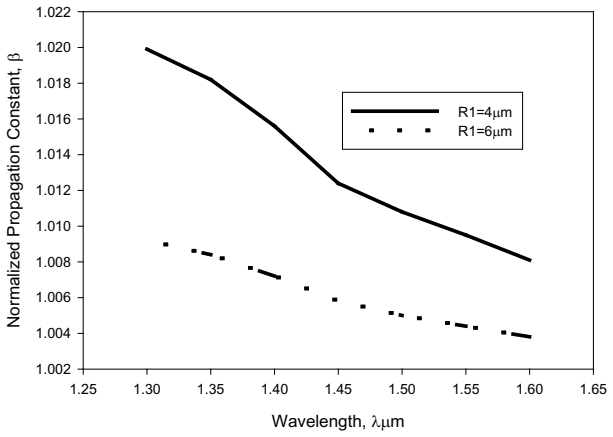

Fig. 9: A) Dependence of normalized propagation constant on wavelength for two different core sizes

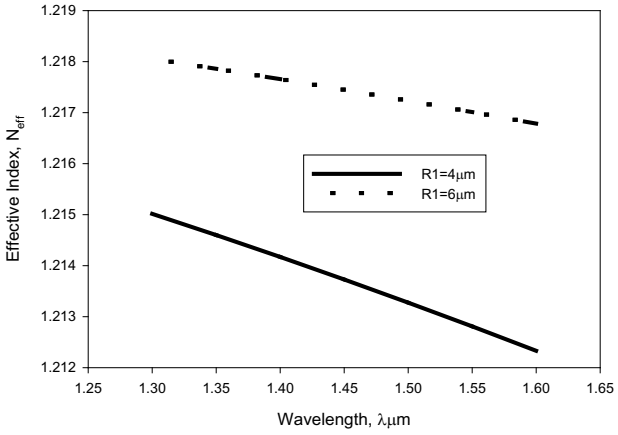

Fig. 9: B) Dependence of effective index on wavelength for two core radii

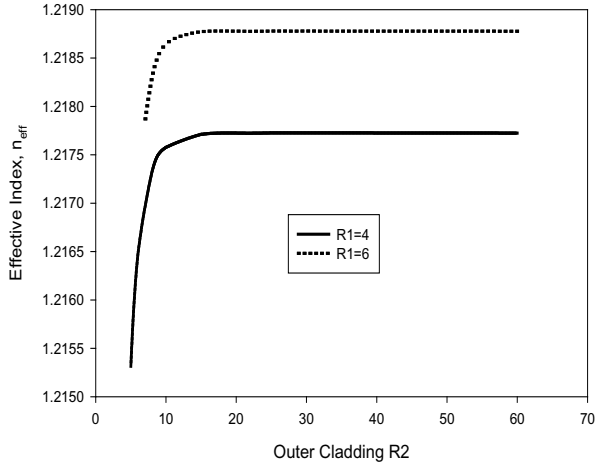

Fig. 10: A) Dependence of effective index on width of outer cladding for two different core sizes.

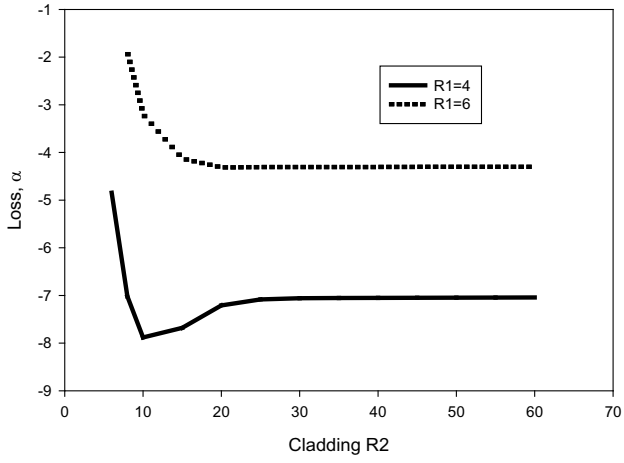

Fig. 10: B) Showing the loss factor for two different core sizes.

In each case, two different values of the core radius (R_1=4 μm and R_1=6 μm) are depicted. It can be observed that at a wavelength of λ=1.3 μm, for a core radius of 4 μm the normalized value of the propagation constant, β, is 1.020, and for a core radius of 6 μm, β=1.010, indicating a better confinement of the waves. On the other hand, the effective index of the smaller fibre core (R_1=4 μm) at the same wavelength of λ=1.3 μm is 1.215. For a core radius of R_1=6 μm, the value of the effective index is 1.218. This is entirely consistent with what is to be expected, since the higher the effective index, the better the waves will be propagated.

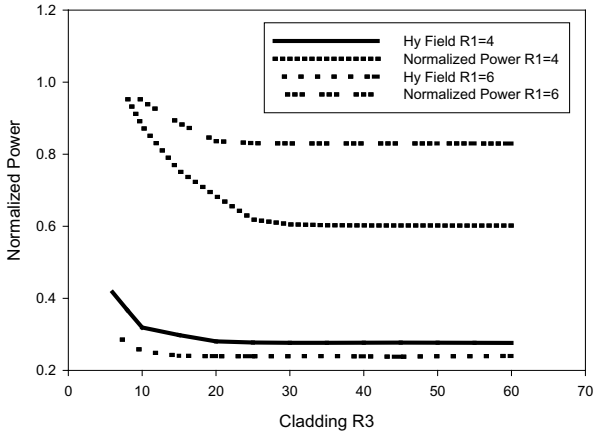

Fig. 11: A) Normalized values of power and field as function of outer cladding

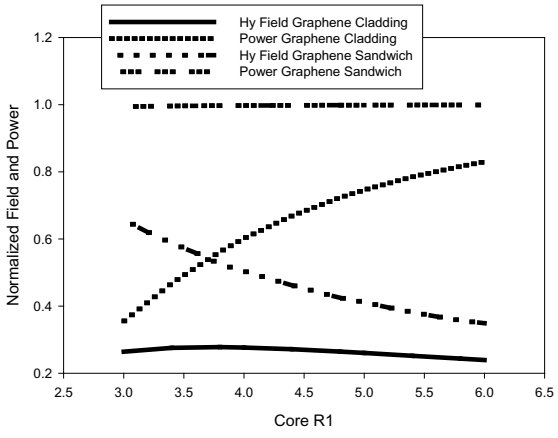

Fig. 11: B) Normalized values of power and field as a function of core diameter

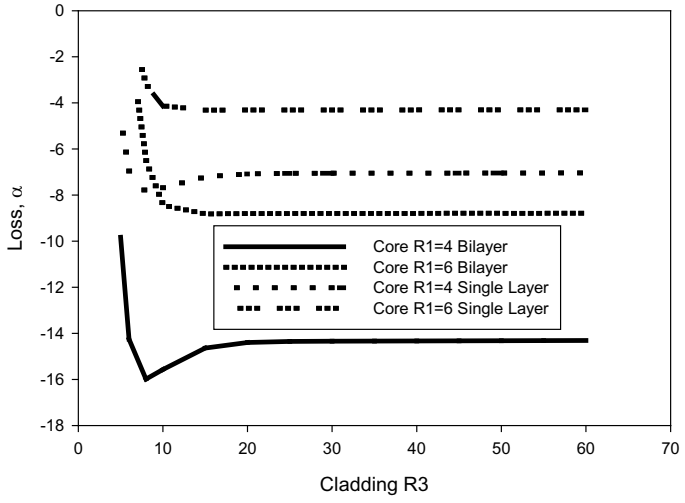

Fig. 12: Loss factor as a function of outer cladding for both single layer and double layer graphene

In the next simulations, an outer cladding is introduced to reflect the configuration of Fig. 1B. Figure 10 shows the results of the dependence of the effective index and the loss on the width of the outer cladding for two different core sizes. As will be expected, as the outer cladding is increased, the effective index also increases. However, beyond a certain point, in this case about 10 microns, any further increase in the cladding width does not impact on the results (Rahman and Davies, 1984). A sharp drop in loss factor at the point where the results become stable is worth noting. This drop may be attributed to transient instabilities.

Fig. 11A shows the normalized values for the H_y field and power for two different core sizes as the outer cladding is varied. Fig. 11B on the other hand shows the same parameters, but in this case, with the cladding width kept constant and the core size varied. In one case there is no outer cladding. With a constant value for the core region, we note that as cladding size is increased, the power within the core region decreases. However, if we keep the cladding constant and increase the core size, the power increases. This can be attributed to the fact that calculations for power are done within the core region, and the larger the core, the greater the power that is accounted for.

Results for Bilayer Configuration:

In some instances, it is found useful to use a number of layers of graphene (Hiura *et al.,* 2010). This may be due to the difficulty in obtaining a single sheet of the graphene. Usually, the maximum number of layers is assumed to be 3, as beyond this the material is no longer considered to be graphene (Miyazaki *et al.,* 2008; Pimenta *et al.,* 2007; Hiura *et al.,* 2010). In the next simulation, Fig. 12, it is shown how a two-layer graphene affects the simulation parameters. As in the previous simulations, two different core sizes are used, and the results or loss compared with that of a single layer configuration. It can be seen that the loss values for the bilayer devices are α=-15 for R_1= 6 and α=-9 for R_1=4. For the single layer α=-4 for R_1=6 and α=-8 for R_1=6. It may therefore be deduced that there is better confinement of the field in a double layer configuration.

Conclusion

Results for numerical analysis of a graphene cladded fibre have been presented. Two different structures were studied, a fibre core cladded with graphene but with no outer cladding and one in which there is an outer cladding. Single and double layer graphene structures have been investigated. Such a structure may find application as a nonlinear elements in pulse compression schemes. The results obtain show that it is possible to accurately model graphene cladded devices using the finite element method.

References

Bao, Q., Zhang, H., Wang, B., Ni, Z., Lim, C.H., Wang, Y., Loh, K.P. (2011). Broadband graphene polarizer, *Nature Photonics,* 5, 411-415.

Bao, Q., Zhang, H., Wang, Y., Ni, Z., Yan, Y., Shen, Z. X., Loh, K. P., Tang, D. Y. (2009). Atomic-layer graphene as a saturable absorber for ultrafast pulsed lasers. *Advanced. Functional. Materials*, 19, 3077-3083..

Bonaccorso F., Z. Sun, T. Hasan and A. C. Ferrari, (2010). Graphene Photonics and Optoelectronics, *Nature Photonics* 4, 611–622.

Themistos, C., Rahman, B.M.A., Markides, C, Uthman, M., Quadir, A. and Kejalakshmy, N. (2014). Characterization of graphene-based devices for THz systems, in Terahertz Physics, Devices, and Systems VIII: Advanced Applications in Industry and Defense, Mehdi F. Anwar; Thomas W. Crowe; Tariq Manzur, Editors, Proceedings of SPIE Vol. 9102 (SPIE, Bellingham, WA 2014), p. 91020F.

Miyazaki, H., Odaka, S., Sato, T., Tanaka, S., Goto, H., Kanda, A., Tsukagoshi, K., Ootuka, Y. and Aoyagi, Y. (2008). Inter-Layer Screening Length to Electric Field in Thin Graphite Film. *Appl. Phys. Express 1* (2008) 034007 -1-034007-3.

Hiura, H., Miyazaki, H. and Tsukagoshi, K. (2010). Determination of the Number of Graphene Layers: Discrete Distribution of the Secondary Electron Intensity Stemming from Individual Graphene Layers. *Applied Physics Express*, Volume 3, Number 9 , p.095101-1-095101-3

Huan Li, Yoska Anugrah, Steven J. Koester, and Mo Li, (2012). Optical absorption in graphene integrated on silicon waveguides, *Appl. Phys. Lett.* 101 (11) 111110-1-111110-5.

Inoue, T. and Namiki, S. (2008). Pulse compression techniques using highly nonlinear fibers, *Laser Photon. Rev*. 2, 83–99.

Katsriku, F.A. (2000). 'Finite element study of the second order (X^2) non-linear process of second harmonic generation in optical waveguides.' PhD Thesis, City University, London.

Keilmann, (2012). Trapping light in a carbon net, *Graphene Research*, Ludwig-Maximilians-Universitat Munchen. Available at https://www.en.uni-muenchen.de/news/newsarchiv/2012/2012_keilmann.html. Accessed 17th November 2017.

Kim, J.T. and Choi, S.Y. (2011). Graphene-based plasmonic waveguides for photonic integrated circuits, *Optics Express*, Nov. 21, 19(24), 24557-62.

Liu, M., Yin, X. and Zhang, X. (2012). Double-Layer Graphene Optical Modulator, *Nano Letters*, March 14, 12(3), 1482-5.

Liu, M., Yin, X., Ulin-Avila, E., Geng, B., Zentgraf, T., Ju, L., Wang, F. and Zhang, X. (2011). A graphene-based broadband optical modulator, *Nature*, 474, 64-67.

Novoselov, K.S., Jiang, Z., Zhang, Y., Morozov, S.V., Stormer, H.L., Zeitler, U., Geim, A.K. (2007). Room-Temperature Quantum Hall Effect in Graphene, Science, 315(5817), p. 1379.

Huang, P.L., Lin, S.C., Yeh, C.H., Kuo, H.H., Huang, S.H., Gong-Ru Lin, Cheng, W.H. (2012). Stable mode-locked fiber laser based on CVD fabricated graphene saturable absorber Optics Express 20 (3), 2460-2465.

Pimenta, M. A., Dresselhaus, G., Dresselhaus, M. S., Cancado, L. G., Jorio, A., Saito, R. (2007). Studying disorder in graphite-based systems by Raman spectroscopy. *Phys. Chem.* 9 (11), 1276 -1291.

Pumera, M. (2011), Graphene in Biosensing, *Materials Today*, 14(7-8), 308-315.

Rahman, B.M.A. and Davies, J.B. (1984). Penalty function improvement of waveguide solution by finite element. *IEEE Transactions on Microwave Theory Techniques MTT*-32 (8), 922-928.

Sensale-Rodriguez, B., Yan, R., Kelly, M. M., Fang, T., Tahy, K., Hwang, W. S., …Xing, H. G. (2012). Broadband graphene terahertz modulators enabled by intraband transitions, *Nature Communications*, 3 (780) 1-7.

Sun, Z., Hassan, T., Torrisi, F., Popa, D., Privitera, G., Wang, F., … Ferrari, A.C. (2010). Graphene mode-locked ultrafast laser, ACS Nano, 4, 803-813.

Sun, Z., Popa, D., Hasan, T., Torrisi, F., Wang, F., Kelleher, E.J.R, Ferrari, A.C. (2010). A Stable, Wideband Tunable, Near Transform-Limited, Graphene-Mode-Locked, Ultrafast Laser, Nano Research, 3(9): 653-660.

Thomas, M., Fengnian, X. and Phaedon, A. (2010). Graphene photodetectors for high-speed optical communications, *Nature Photonics*, 4, 297-301.

Zhang, H., Tang, D. Y., Zhao, L. M., Bao, Q. L., Loh, K. P. (2009). Large energy mode locking of an erbium-doped fiber laser with atomic layer graphene. *Opt. Express*, *17*, 17630–17635.

Zhu, S., Quarterman, A.H., Wonfor, A., Penty, R.V. and White, I.H. (2014) *Generation of 140 fs pulse train with widely tunable repetition rate through cascaded fibre compression techniques.* IET Optoelectronics, 8. 108-112

Performance Evaluation of Chromatic Dispersion Compensation Techniques in Single Mode Fibre for Radio over Fibre Applications

Isaac Dankwa[1], Ferdinand A. Katsriku[1*], Andy B. Amewuda[1], Grace G. Yamoah[1], J-D Abdulai[1]

[1]Department of Computer Science, University of Ghana
***Corresponding author:** fkatsriku@ug.edu.gh

ABSTRACT

With the increasing growth and high demand for data, fiber optic transmission, especially radio over fibre (RoF), has become a viable option for data and wireless communication. In such systems however, dispersion is a huge limiting factor in achieving the high data transmission rates. This work reviews current dispersion systems and proposes a system of dispersion compensation with fibre grating. Simulations are conducted using Optisystem 7.0 at varied data rates of 10, 20 and 40Gbps over a 200km transmission distance. The output is analyzed on parameters such as bit error rate (BER), Q-factor and eye height. It is shown that data rate exceeding 10 GB/s is achievable over a 200km distance.

Keywords: Radio over Fibre, LTE, Wimax, single mode fiber, 3G

Introduction

Long Term Evolution (LTE) and Worldwide Interoperability for Microwave Access (WiMAX) have emerged as platforms of choice in future generation wireless platforms for broadband communications, where the focus is more on multimedia services than on voice services. The spectral region best placed to provide such broadband capability is a millimetre frequency band of up to 300GHz.

WiMAX as a digital wireless data communication system was designed to provide high speed broadband services to large geographical areas. Under line of sight conditions, it is capable of achieving transmission speeds of up to 1Gbps for fixed systems and can cover distances of up to 50 km. WiMAX is an access technology with standards defined for both fixed and mobile coverage. It supports different modulation techniques such as Binary Phase Shift Keying (BPSK), Quadrature Phase Shift Keying (QPSK), 16-QAM and 64- QAM. The use of Orthogonal Frequency Division Multiplexing (OFDM) at the physical layer provides immunity to signal multipath. A major disadvantage of WiMAX is that it cannot support both high bit rates and large distances simultaneously. The bit error rate increases substantially at the maximum operating distance. Additionally, to utilize the full functionality of WiMAX, specialized equipment with dedicated antennae are required. Performance is further compromised because of shared bandwidth among users.

Long term Evolution (LTE) is the next big step beyond High Speed Packet Access (HSPA) in the development of 3rd Generation Partnership Project (3GPP) technologies. Supporting and promoting the most important aspects of mobile telephony and broadband, namely unparalleled mobility and coverage, LTE has an increased focus on quality and operational efficiency in the explosive growth of data service usage (Opatic, 2009)

The transmission impairments of the wireless medium however do pose significant challenges. To provide efficient coverage at such high transmission frequencies

will require the use of small cell sizes, which leads to higher implementation costs.

Radio-over-Fibre (RoF) techniques have been a subject of intensive research over the last few decades and have found applications in optical signal processing, radar systems, millimetre-wave and photonic up- and down-converting links for applications such as broadband wireless access networks (Opatic, 2009). Radio over Fibre does offer a medium term solution and seeks to integrate LTE and WIMAX with existing fibre communications infrastructure. Radio over Fibre depends on the use of the best attributes of two technologies, both of which are well developed and offer great advantages. RoF utilises the great bandwidth, order of THz and low loss, less than 0.5 dB/km offered by optical fibre, to send radio signals to remote antennas. The strength of a radio signal is its ability to provide tetherless connection to users. In proposed RoF systems, the remote antennas only have to perform optical to electrical conversion and all the other signal processing is done in a central office (CO). This greatly simplifies the design of the remote antennas. A RoF system is therefore one which distributes radio signals from a CO to remote antennas using optical links. The important optical parameters that require modulation are the amplitude, frequency and phase of the optical field. The basic architecture of an RoF system is therefore made up of a central office (CO) and remote antennas, connected by optical links or a network. In Global System for Mobile Communication (GSM) systems, the mobile switching centre can serve as the CO and the base stations as the antennas. An important application area for RoF systems is for use in extending the range and capacity of radio signals to large indoor places such as shopping malls where there are high concentrations of people. RoF also provides an ideal solution for delivering broadband access to the last mile, in particular the network connection between the carrier's Central Office (CO) and the subscriber's location.

The use of optical fibre links to distribute telecommunication signals is the more successful application of RoF technology, usually known as hybrid fibre-radio (HFR) networks (Opatic, 2009). RoF networks have been deployed in the last decade due to the increasing demand for high-bitrate communication services in today's access network. This demand is based on the steady market introduction of services requiring the transmission of massive data quantities, like high-definition movie distribution, on-line gaming and rich Internet experience. The RoF concept applied to the enhancements of community antenna television (CATV) networks reflected in the so-called hybrid-fibre coax (HFC) network, in which a combination of digital and analogue channels is distributed from a central location to many users distributed geographically (Shukla 2012, Darcie *et al.,* 1991). In HFC networks the last mile connection is provided through coaxial cable whilst in HFR networks the last mile connection is always a wireless link. This is not a minor difference, as the wireless environment is much more hostile than cable, imposing restrictive RoF link performance requirements. Figure 1 provides a schematic view of RoF and shows a typical RF signal (modulated by analogue or digital modulation techniques) being transported by an analogue fibre optic link. The RF signal may be baseband data, modulated IF, or the actual modulated RF signal to be distributed. The RF signal is used to modulate the optical source in a transmitter. The resulting optical signal is launched into an optical fibre. At the other end of the fibre, we need an optical receiver that converts the optical signal back to RF. The generated electrical signal must meet the specifications required by the wireless application, be it GSM, UMTS, wireless LAN, WiMax or other. By delivering the radio signals directly, the optical fibre link avoids the necessity to generate high frequency radio carriers at the antenna site. Since antenna sites are usually remote from easy access, there is a lot to gain from such an arrangement. Usually a single fibre can carry information in one direction only (simplex), which means that we usually require two fibres for bidirectional (duplex) communication. However, recent progress in wavelength division multiplexing makes it possible to use the same fibre for duplex communication using different wavelengths (Spirit *et al.,* 1994). Wavelength Division Multiplexing (WDM) can be used to combine several wavelengths together to send them through a fibre op-

tic network, greatly increasing the use of the available fibre bandwidth and maximizing total data throughput in order to meet future wireless bandwidth requirements (Bhowik 2012).

In optical signal propagation, individual wavelength components of light pulse experience different propagation times due to the fact that the transport medium has different effective refractive indices for different wavelength, hence components or models receive the fibre terminals at different times. This phenomenon is known as dispersion. Dispersion increases along the fibre length and thus, limits the ultimate data rate supported by the fibre (Kalon *et al.,* 2014, Verma *et al.,* 2013). This causes intersymbol interference as pulse travels beyond its allocated bit slot to such an extent that it overlaps with the adjacent bits and it is no longer possible to determine whether or not a specific bit contains a 1 or 0. The focus of this paper therefore is on chromatic dispersion, which is dominant in Single Mode Fibre (SMF) and can be compensated using Dispersion Compensated Fibre (DCF) and Fibre Bragg Grating (FBG). Using the Optisystem, we demonstrate new ways of improving upon dispersion in fibre over long distances.

Chromatic Dispersion (CD)

Chromatic dispersion (CD) is the broadening of the input signal as it travels down the length of the fibre (Kaur, 2015, Kumar *et al.,* 2013). Chromatic dispersion is the second derivative of optical phase with respect to optical frequency and may be represented as follows:

$$\text{Chromatic Dispersion} = \frac{\partial^2 \emptyset}{\partial \omega}$$

Where Ø = optical phase and ω = optical frequency.

The dispersion-induced spectrum broadening would be very important even without nonlinearity.

Dispersion plays an important role in signal transmission over fibres (Udayakumar *et al.,* 2013). The interaction between dispersion and nonlinearity is an important issue in light wave system design. There exist some other fibres whose characteristics have been modified to give them a dispersion profile different from pure silica. They include Zero dispersion (DSF, Dispersion Shifted Fibre) or small dispersion (NZ-DSF, Non-Zero Dispersion Shifted Fibre) and Constant dispersion over a large window (DFF, Dispersion Flattened Fibre) around 1.55μm. The main advantage of NZ-DSF is a reduction of the nonlinear effects that require phase matching, like Four Wave Mixing (FWM).

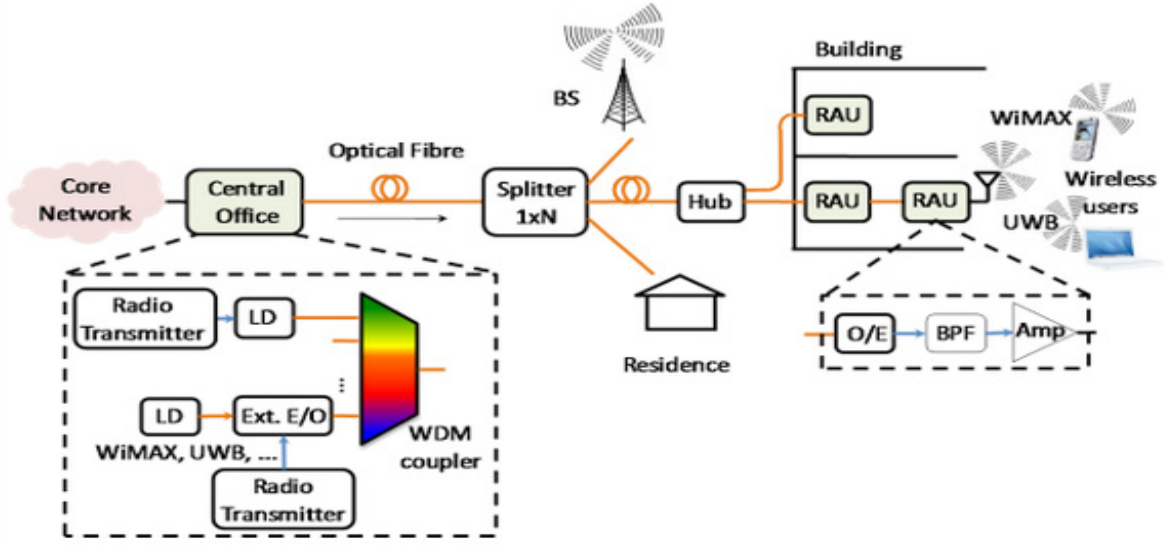

Fig. 1: Simplified schematic diagram of a RoF system

The use of dispersion compensation fibre is an efficient way to upgrade installed links made of standard single mode fibre (Bhowik 2012). According to relative positioning of Dispersion Compensated Fibre (DCF) and single mode fibre in Fig. 2, post-compensation, pre-compensation and symmetrical/mixed compensation can be made. A DCF Pre-compensation scheme achieves dispersion compensation by placing the DCF before a certain conventional single-mode fibre, or after the optical transmitter. A post compensation scheme achieves dispersion compensation by placing the DCF after a certain conventional single-mode fibre, or after the optical transmitter. A symmetrical/mixed compensation scheme consists of post-compensation and pre-compensation. Different locations on the system will generate different nonlinear effects (Riant *et al.,* 1999).

The simulation setup for each compensation technique is shown below:

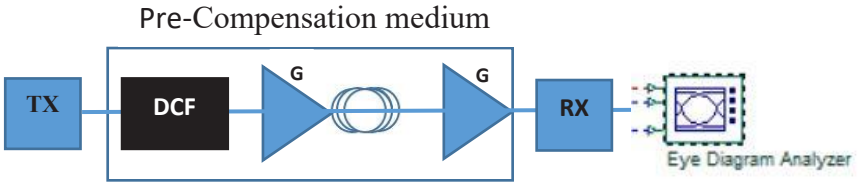

A. Pre-Compensation

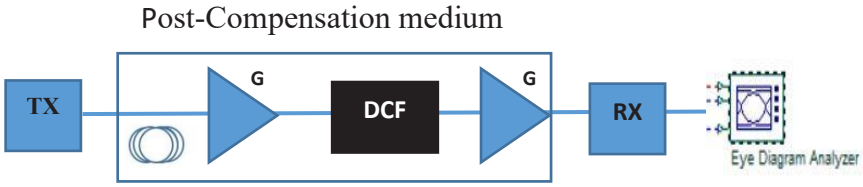

B. Post–Compensation

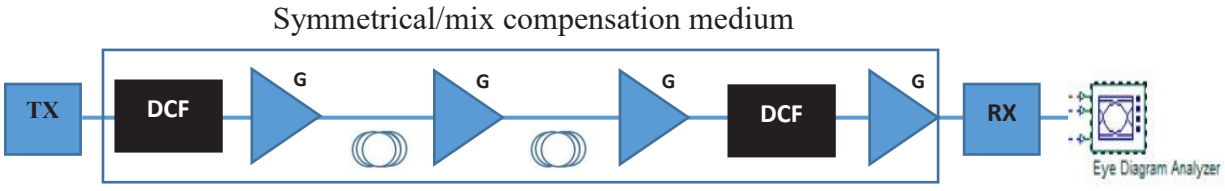

C. Symmetrical /mix compensation

Fig. 2: Three Dispersion Compensation Schemes, A) pre-compensation B) post-compensation C) symmetrical /mixed compensation.

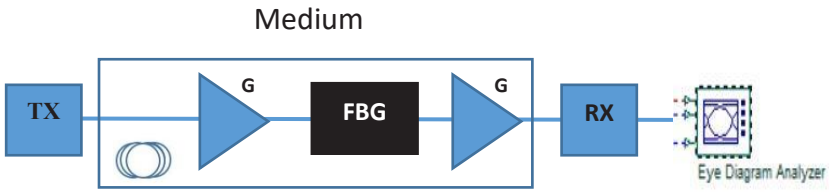

Fig. 3: Simulation Setup for FBG: Main System Simulation

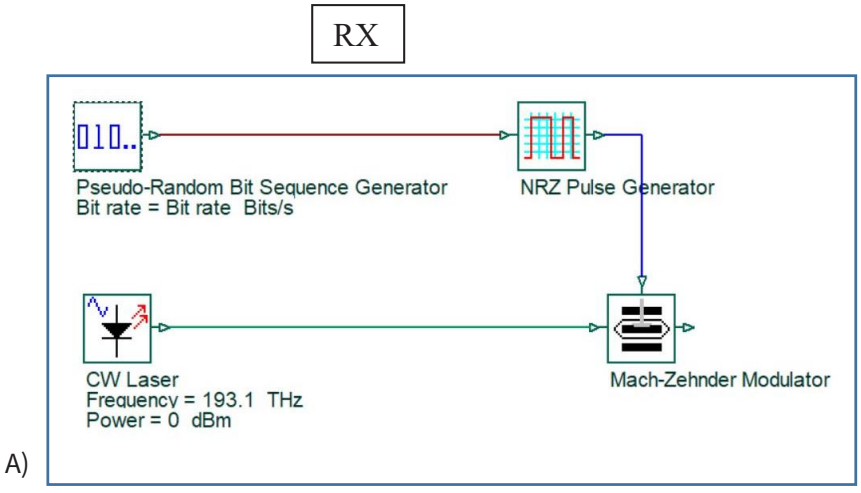

A)

TX

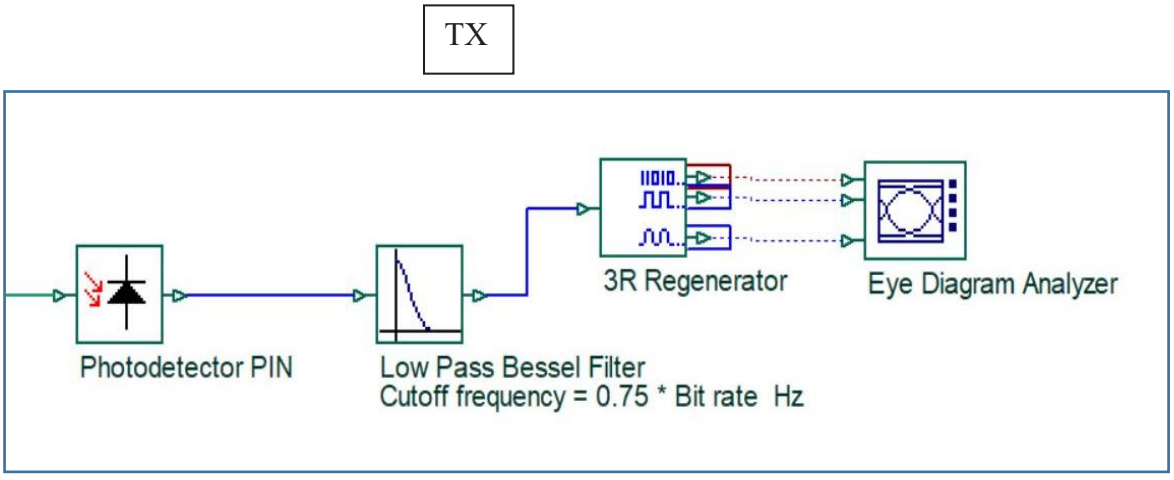

B)

RX

Fig. 4: Detailed implementation of RX and TX in simulations: A) RX B) TX

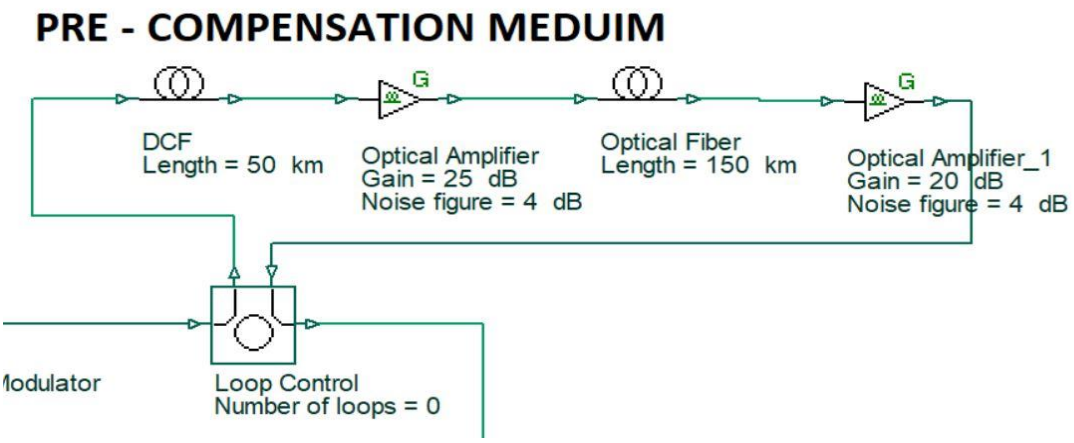

Fig. 5: A) The implementation for Pre-Compensation medium

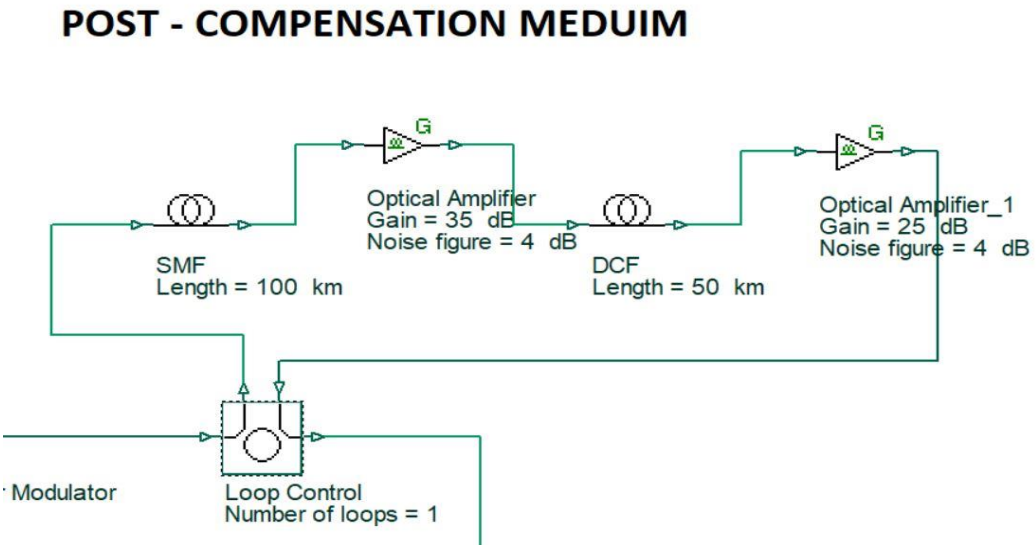

Fig. 5: B) The implementation for Post-Compensation medium

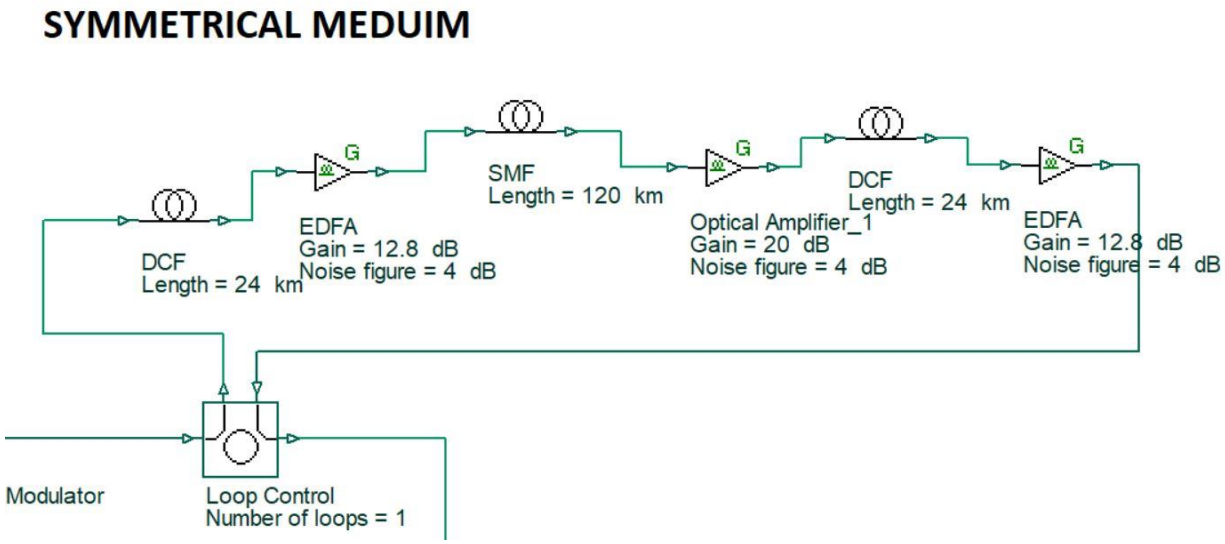

Fig. 5: C) The implementation for Symmetrical medium

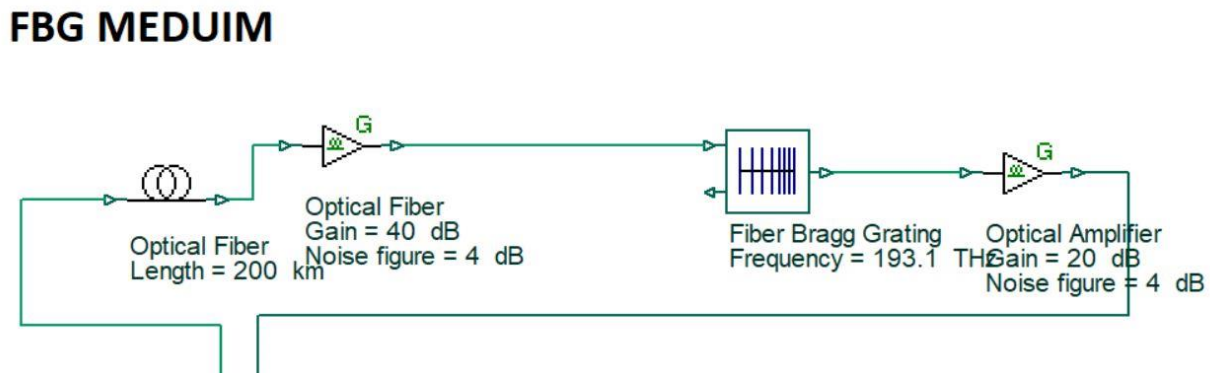

Fig. 5: D) The implementation for FBG medium

Structure of Refractive Index change in FBG

FBG structure varies with respect to the refractive index, or the grating period. The grating period can be uniform or graded, and either localized or distributed in a superstructure.

Chirped Fibre Bragg Grating: Here, the refractive index profile of the grating may be modified to add other features, such as a linear variation in the grating period, called a chirp. The reflected wavelength changes with the grating period, broadening the reflected spectrum. A grating possessing a chirp has the property of adding dispersion— which means that different wavelengths reflected from the grating will be subject to different delays (Gnanagurunathan *et al.,* 2010; Islam *et al.,* 2012).

A *Tiled Fibre Bragg Grating* refractive index is at an angle to the optical axis, which is quite different from the Chirped Fibre Bragg Grating. The angle of tilt in a

Tiled Fibre Bragg Grating has an effect on the reflected wavelength, and on bandwidth.

Another structure type is the *Long-Period Grating*, which is designed to achieve a broader response than the standard FBG. They typically have grating periods on the range of 100 micrometres to a millimetre, and are therefore much easier to manufacture. For standard grating, a Bragg wavelength reflects at 1550 nm, with a grating period of 500 nm using an effective refractive index of 1.5.

Methodology

Using Optisystem 7.0 simulator software, the simulation for each dispersion compensation techniques is considered. The first simulation setup is for DCF as dispersion compensator, followed by FBG. The simulation consists of a transmitter, which is made up of a data source, a modulator driver (NRZ driver), a laser source and a Mach-Zehnder modulator. The data source produces a pseudorandom sequence of bits at a rate of 10Gbit/s. The output of the data source is given to the modulator driver which produces an NRZ format pulse. CW Laser source output power is 10dBm at an ideal frequency of 193.1 THz. MZM has an excitation ratio of 30db. The loop control system has one and two loops for DCF and one FBG respectively. The total transmission distance for the SMF is 200 km. EDFA is deployed to restrict the effect of optical loss. The receiver side consists of a PIN photodetector which has a responsivity of 1A/W and a dark current of 10 nA. The electrical signal obtained is filtered by a low pass Bessel filter and a 3R regenerator. Their results are analyzed against parameters such as BER, Q-factor, and eye diagram.

Results and Analysis

Simulation for DCF as Dispersion Compensator

As already noted, DCF as a compensator can be implemented in three flavors (Pre-compensation, post-compensation and symmetrical compensation). Table 1 provides detailed information on the parameters used in simulating the three DCF placements in the setup.

The simulation setup for each compensation technique is shown in the diagrams in Fig. 3. The detailed implementation of RX and TX is shown in diagrams in Fig. 4. Figure 5 shows detailed implementation diagrams for the various medium used in each of the compensation schemes and our proposed scheme.

Table 1: Simulation Parameters for DCF

SMF Parameters	Values
Reference wavelength	1550 nm
Length	150 km
Attenuation	0.2 db/km
Dispersion	17.25 ps/nm/km
Dispersion slope	0.08 ps/nm^2/km
PMD coefficient	3 ps/km
Differential group delay	0.2 ps/km

DCF Parameters	Value
Reference wavelength	1550
Length	50 km
Attenuation	0.2 db/km
Dispersion	-80ps/nm/km
Dispersion slope	0.085ps/nm^2/km
PMD coefficient	3ps/km
Differential group delay	0.2ps/km

Simulation for FBG as Dispersion Compensation

FBG is post-compensated in this simulation. The simulation parameters used are shown in Table 2. The eye diagrams shown in Fig. 6 are for each type of DCF compensator at 10 gb/s over 200 km. As can be observed from the results obtained, the eye diagram for symmetrical compensation is wider and well organized, indicating that the signal received is of higher quality

with little attenuation. Post-compensation performed better than pre-compensation. The Q-factor values obtained and shown in Table 3 confirm these results. The table compares the Q-factor, Min BER and Eye height for the three different compensation schemes that were used. From the table, it can be seen that symmetrical compensation has a huge Q-factor with considerable Min BER. Even though post-compensation has very little BER, its Q-factor has very little influence on the signal quality. Pre-compensation performed the worst, with the least eye height and Q-factor.

A)

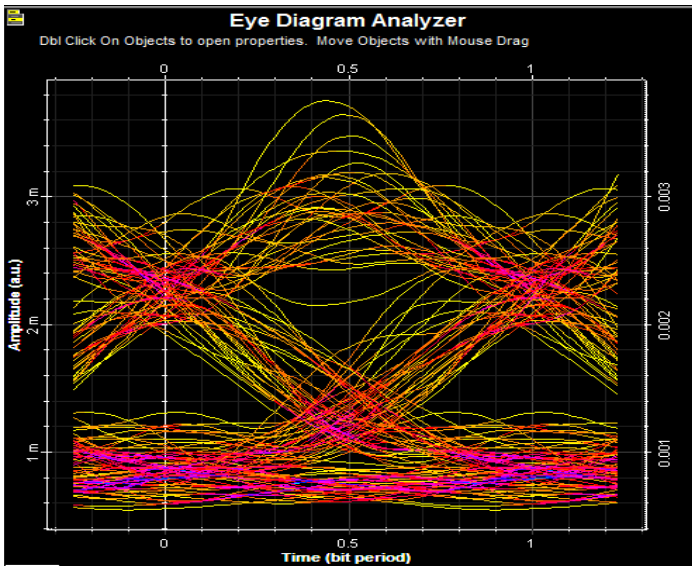

Pre-Compensation eye diagram

B)

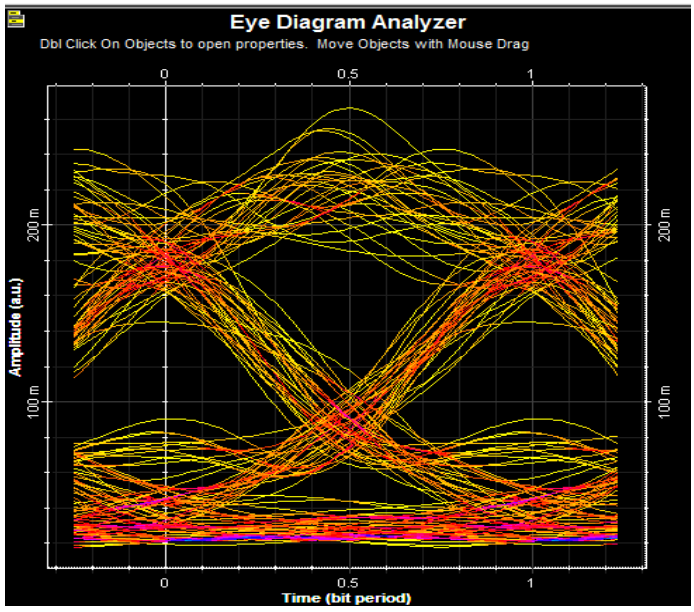

Post-Compensation eye diagram

C)

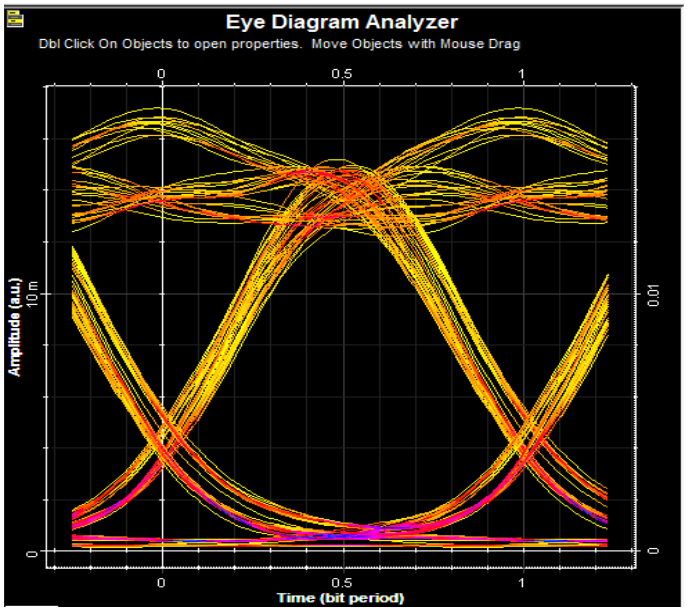

Symmetrical Compensation eye diagram

Fig. 6: Eye diagrams for DCF compensator at 10gb/s over 200km

Table 2: FBG Simulation Parameters used in the experiments

FBG Parameters	Values
Dispersion	17.25 ps/nm/km
Attenuation	0.2
Dispersion Slope	0.08 ps/nm^2/km
Fiber length	200 km
Frequency	193.1 (THz)
Effective Refractive Index	1.45
Length of Grating	80 mm
Apodization function	Than
Chirp function	Linear

Table 3: Q-factor, BER and Height for DCF compensators

	Pre Compensation	Post Compensation	Mix Compensation
Q-factor	2.75398	3.23806	15.2922
Min BER	0.00250132	0.000574932	4.03595e – 053
Eye Height	-0.00160187	0.0114179	0.0105176

A Fibre Bragg Grating (FBG) is used as a compensator in our next simulation. The eye diagram for each FBG compensator is shown in Figure 7. The FBG compensator performs well to reduce dispersion in fibre optic communication. It can be observed that the eye diagram is wider, with a considerable eye height. With this clarity, it can be said that received signal will be readable.

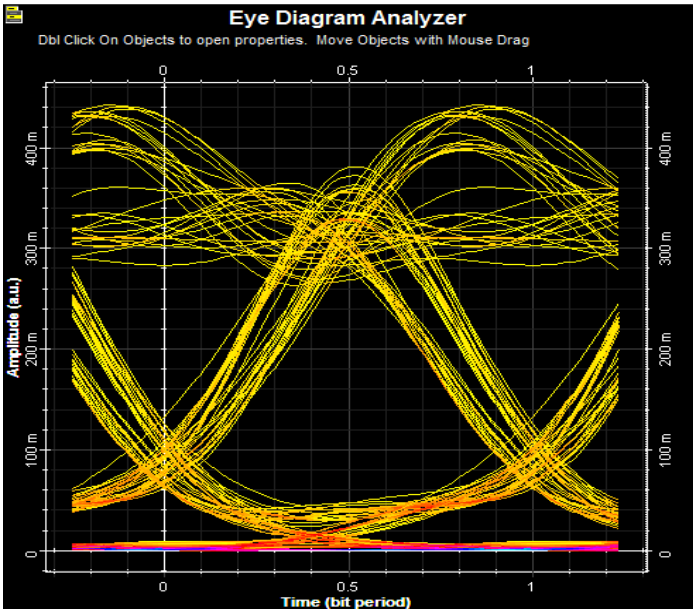

Fig. 7: Eye diagram for FBG compensator

Table 4: shows the values for Q-factor, Min BER and Eye height for the FBG as a compensator.

Q-factor	7.83208
Min BER	2.26553e-015
Eye Height	0.184665

Table 4 Q-factor, Min BER and Eye Height values for FBG

Comparing the above simulation results and findings, it can be clearly stated that from the eye diagram and Q-factor, DCF symmetrical compensation performs better than all the studied dispersion compensators. Increasing the data rate from 10 GB/s to 20 GB/s, and holding the same parameters, the following results were achieved.

Fig. 8 shows the eye diagram for the DCF symmetrical compensation scheme when the data rate is increased from 10 GB/s to 20 GB/s over a 200 km distance.

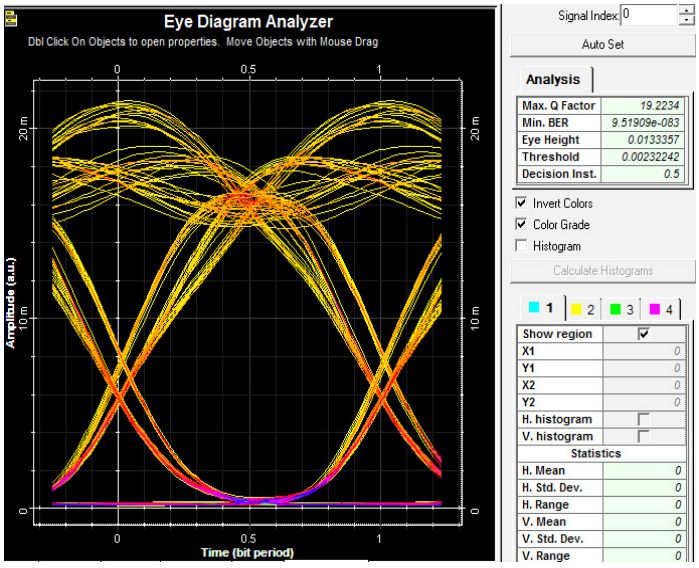

Fig. 8: DCF Symmetrical compensation at 20 GB/s at 200 km

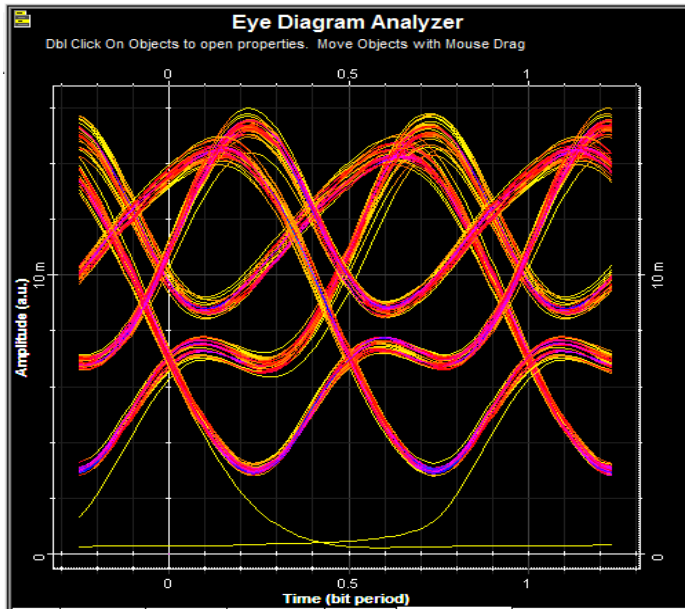

Fig. 9: DCF Symmetrical Compensation at 40 GB/s over 200 km

From the eye diagrams obtained for all the compensators, together with their parameter values, it was observed that DCF symmetrical compensation performed better, despite its BER value. The worst of them at 20 Gb/s over 200 km is FBG whose values were not even available due to huge signal dispersions. Figure 9 shows the eye diagram for the DCF symmetrical compensation scheme when the data rate is increased to 40 GB/s over a 200 km distance. It can be seen that at 40 GB/s dispersion increased considerably, indicating that higher bandwidth leads to greater dispersion. The results obtained confirm that as data rate increases, dispersion also increases.

Conclusions

Chromatic dispersion is a disturbing phenomenon in optical communication. In this paper, the various kinds of dispersion compensation were studied, with particular focus on DCF and FBG. Their performance in reducing dispersion in a long haul transmission system was analyzed. From the simulations performed using Optisystem 7.0 simulator, it has been shown that such dispersion can be compensated for by use of a symmetrical DCF as a compensator in the optical transmission fibre and this performs better than FBG and other DCF (pre- and post-compensation).

References

Bhowik, K., Ahmed, M. and Momim, A. (2012). Reduction of dispersion in optical communication by fiber bragg grating and optical phase conjugation techniques. *International Journal of Mobile Network Communications & Telematics* (IJMNCT) 2 (3), 49-58.

Darcie, T.E., Bodeep, G.E. and Saleh, A.A.M. (1991). Fiber-reflection induced impairment in Lightwave AM-VSB CATV system. *IEEE J. Lightwave Technology,* 9 (8), 991-995.

Galle, M.A., (2007). Single-arm-3-wave interferometer for measuring dispersion in short length of fiber. *Optics Express*, 15(25), 16896-16906.

Gnanagurunathan, G., and Rahman, F.A. (2006). Comparing FBG and DCF as dispersion compensators in the long haul narrowband WDM systems. *International Conference on Wireless and Optical Communications Network 2006*, Bangalore, India, p4.

Islam, J., Islam, S. and Rahman, M. (2012). Dispersion Compensation in Optical Fiber Communication Using Fiber Bragg Grating. *Global Journal of researches in Engineering Electrical and Electronics Engineering*, 12(2), 25-29.

Jamaludin, Z., Abas, A.F., Noor, A.S.M. and Abdullah, M.K. (2005). Issues on Polarization Mode Dispersion (PMD) for high speed fiber optics transmission, *Suranaree Journal Science Technology* 12(2), 98-106.

Kalon, N.K and Kaur, G. (2014). Various Dispersion compensation techniques for optical system: A survey. *Open journal of communications and software*, 1(1), 1-5.

Kaur, M., Sarangal, H. and Bagga, P. (2015). Dispersion Compensation with Dispersion Compensation Fiber (DCF). *International Journal of Advanced Research in Computer and Communication Engineering*, 4(2), 354-356.

Kumar, S., Jaiswal, A.K., Kumar, M., and Saxena, R. (2013). Performance Analysis of Dispersion Compensation in Long Haul Optical Fiber with DCF. *IOSR Journal of Electronics and Communication Engineering* (IOSR-JECE), 6(6), 19-23.

Riant, I., Gurib, S., Gourhant, J., Sansonetti, P., Bungarzeanu, C. and Kashyap, R. (1999). Chirped Fiber Bragg Gratings for WDM Chromatic Dispersion Compensation in Multispan 10-Gb/s Transmission, *IEEE Journal Of Selected Topics In Quantum Electronics*, 5(5), 1312-1324.

Shukla A. (2012). *Elements Of Optical Communication and Opto Electronics*. New Delhi: University of Science Press.

Spirit, D.M., Ellis, A.D. and Barnsley, P.E. (1994) Optical Time Division Multiplexing: Systems and Networks, *IEEE Communications Magazine*, 32(12), 56-62.

Udayakumar, R., Khanaa, V. and Saravanan, T. (2013). Chromatic Dispersion Compensation in Optical Fiber Communication System and its Simulation. *Indian Journal of Science and Technology*, 6(6s), 4763-4766.

Verma, A.S, Jaiswal, A.K. and Kumar, M. (2013). An Improved Methodology for Dispersion Compensation and Synchronization in Optical Fiber Communication Networks. *International Journal of Emerging Technology and Advanced Engineering*, 3(5), 769-775.

Automatic Satellite Dish Positioning for Line of Sight Communication using Bluetooth Technology

Robert A. Sowah[1*], Godfrey A. Mills[1], Joseph Y. Nortey[1], Stephen K. Armoo[1] and Seth Y. Fiawoo[1]
[1] Computer Engineering Department, Legon, University of Ghana
Corresponding author: rasowah@ug.edu.gh

ABSTRACT

Satellite dishes are used to receive beams of signals from satellites and other broadcasting sources which are then focused onto an antenna. The dish needs to be adjusted to get the desired azimuth and elevation for maximum signal reception. To overcome the difficulty of adjusting it manually, it would be beneficial to have a system that aligns the satellite receiver by mechanical means while allowing the user to interact with the system remotely to achieve a line of sight communication with the satellite source of interest. This paper proposes the design and development of a system which receives user specifications from an Android application via Bluetooth by either specifying the direction of orientation of the dish or selecting a satellite of interest. A control system interacting with the developed user interface achieves this. It employs a microcontroller, a GPS device, a compass and two servo motors to manage the orientation of the dish on its horizontal and vertical axes. The Smartphone utilizes its Bluetooth socket to communicate with the Bluetooth module interfaced to the microcontroller. A database containing information on available satellites is included in the Android application which is transferred to the microcontroller for computation of azimuth and elevation angles when the GPS coordinates and compass headings are obtained from their respective devices. Tests carried out showed positive results for control of the orientation of the satellite dish in various directions over a 50m radius. The automatic adjustment functionality provided precise direction for line of sight communication when users chose their satellite of focus.

Keywords: Line of Sight, Satellite Dish Positioning, Bluetooth technology, remote control and communication

Introduction

Satellites form an essential part of communication systems worldwide because they carry large amounts of data, telephone traffic and television signals. The use of satellites in everyday life is evident in the many homes and offices that are equipped with various forms of antennas which are used to receive signals from satellites located farther away from the earth. Satellites are positioned farther away from the earth because the gravitational pull of the earth is weaker at relatively higher levels and stronger at lower levels, so that communication satellites are usually mounted about 36,000 km away from the earth (Cheruku, 2010). Since about 42% of the earth's area is visible from a satellite, satellite communication has an edge over other means of communication (Vaneli-Corali, A. *et al.,* 2007). To prevent satellites fr--om swaying from their positioned orbits, some form of stabilization is required. Attitude control provides such stabilization through the orientation of the satellite with a system that keeps it moving evenly through its orbits (Galactics, 2016). With geostationary satellites, the satellite can receive or transmit messages to any transmitter or transceiver that is within a fixed geographical area visible to the satellite at all times.

Communication between observers on the earth and satellites in space is made possible by means of antennas. A satellite dish is a type of antenna designed to focus on a specific broadcast source which receives information by reflecting signal beams and focusing them into a relatively narrow beam that hits its parabolic surface and

then passes the signal on to the feed horn, from where it is further transmitted to the receiving equipment (Nice & Harris, 2000).

The art of remote communication between users of devices and their corresponding systems is becoming more and more complex daily, with diverse ways such as electrical wires, component cables, storage media, computer buses, radio signals and infrared beams, and an even greater variety of connectors, plugs and protocols (Franklin & Layton, 2000).

Wired communication is used to describe any type of communication process that relies on the direct use of cables and wiring to transmit data. Examples of wire-based communication technologies include telephone networks and fiber-optic communication (Tatum, 2016).

This notwithstanding, wireless technologies have changed how people and devices everywhere in the world can correspond with each other, where user or device location is not expected to be fixed for communication, with a great migration from wired to wireless technologies in many instances of life (Dutta, 2015, Adewusi, 2000). .

Wireless communication technologies are of varying types, ranging from Infrared (IR) to Bluetooth. The distance between communicating devices is widely dependent on the type of wave involved in communication, which allows the transmission of data from within a few meters to thousands of kilometers. Bluetooth was developed in 1994 at Ericsson and operates in the unlicensed industrial, scientific and medical (ISM) band from 2.4 to 2.485 GHz, using a spread spectrum, frequency hopping, full-duplex signal at a rate of 1600 hops/sec. It is one popular method of wireless communication between devices (Rappaport, 2002). This method of data communication uses short-range radio links to replace cables between computers and their connected units (Sairam *et al.,* 2016). The power consumption associated with Bluetooth communication is minimal and its range of communication between devices ranges from 1 to 100 meters, depending on the class of the Bluetooth device (Rappaport, 2002; Franklin & Layton, 2000).

Many smart phones today can communicate using Bluetooth. This makes useful systems that need some form of wireless communication protocol with users, ranging from home automation to industries, offering substantial benefits to wireless network operators. Android, which is open-sourced and backed by Google, has statistics in its favour, indicating the increasing popularity of their devices on the market, providing more incentives to develop applications for Android over closed and PC operating systems (Jackson, 2011).

The system developed in this paper takes advantage of the fast-growing popularity of Android and Bluetooth technologies to develop an Android application that would use permission from users' Bluetooth.

With very little error in misalignment that could lead to a complete loss of a signal from a satellite source, the coordination of the dish is very instrumental to the strength of signal received from the transmitting satellite (Giangrandi, 2016). A dish must therefore be positioned at a particular elevation and azimuth to achieve the strongest possible signal. Users will be allowed to select a satellite dish from a predefined database with essential parameters for a two-dimensional automatic orientation of their satellite dishes, allowing the achievement of a line of sight communication with the broadcasting source.

Satellite Dish Positioning Systems

Various studies and researches have been done over the years on the design and development of satellite dish positioning systems through remote means. *Kyaw Oo et al.* developed Satellite Dish Positioning Control by DC Motor Using Infra-red (IR) Remote Control which sought to allow a user to position a satellite dish remotely through Infra- red (IR) communication (Me *et al.,* 2006). In their system, rotation of the dish was allowed on its horizontal axis. This consisted of a PIC 16F877A microcontroller to provide intelligence, and relay drivers and a DC motor to effect motion. The use of IR technology allowed a marginal distance between the user and the dish, promoting flexibility.

Commercial dish positioning systems have been developed to aid in positioning and general installation of satellite dishes. Infra-red (IR) communication has been the preferred choice of communication between the user and the satellite.

Edgefx Technologies designed and developed the Remote Alignment of 3D Dish Positioning by Android Application. Remote operation of the system was achieved by any device running the Android operating system with a Graphical User Interface based touch screen operation. Components employed included an 8051-series microcontroller, a Bluetooth device, motor drivers and DC motors.

Wilkinson and Swenson (1999) published a paper on the design of a satellite tracking station for remote operation and multi-user observation. The paper discusses the design of a satellite ground station at Utah State University to maintain multiple satellites by remote operation over the internet (Wilkinson & Swenson, 1999). This system allowed various users to remotely position the dish of the ground station via a Java interface to monitor low-orbiting satellites based on their locations in reference to the ground station. A server daemon design running on Sun Solaris 2 provided connections to the users via an internet connection to the hardware drivers. This hardware part of the system was made up of a Tattletale 8 microcontroller for receiving and computing position information of the satellite dish, a UNIX workstation for tracking station users over an internet connection, optical encoders for the relative positions of azimuth and elevation, and two DC motors for providing motion to the dish.

Voormansik (2009) carried out satellite signal strength measurements using the International Space University Ground Station and the University of Tartu Ground Station for satellites in Low Earth Orbits (LEO) (Voormansik, 2009). This required an antenna that points to the orbits in focus and an operator that has access to the ground station to communicate with its satellite to measure satellite signal strengths.

Rafael *et al.* published a development of an automated system for maneuvering parabolic dish antennas used in satellite communication (Rafael, Gonçalves & Leite do Prado, 2012). In this work, the key steps required to manually maneuver an antenna dish were automated. A 3.2 meter diameter antenna dish, a digital satellite receiver and a GPS were employed to capture signals from the satellite source and focus them onto the antenna, decode the channels of the satellite and determine the position of the antenna respectively. User-guided-interfaces developed with Java programming language for use on a computer were also provided that offered information about the movement of the antenna toward the reference position, the spatial position of the antenna and the carrier-to-noise ratio. After the antenna reached the reference position, the system monitored the quality of the reception through the carrier-to-noise ratio obtained, with a minimum value of 8 dB guaranteeing good reception (Ha, 1986).

Based on the reviewed literature in consonance with the need in developing countries, we proposed a cost-effective Satellite Positioning System with added functionalities. The system adapts the portable nature of Android devices and the growing market for their Bluetooth communication capability to provide an interface for users' interaction with their systems for remote orientation of the satellite dish for line of sight communication. An on-board unit made up of a microcontroller, a GPS module, a Bluetooth module, a compass module and servo motors is assembled and attached to the support of the satellite dish receiver. The microcontroller receives parameters based on the user's choice of satellite from the Android device via Bluetooth communication. Computation for the desired azimuth and elevation angles is made when the compass module provides the horizontal angle of direction of the dish and the GPS module provides position and altitude information from the receiver to the microcontroller. The microcontroller then sends the processed values of azimuth and elevation to the motors to effect movement and orientation for maximum signal reception.

System Design and Development

System Architecture

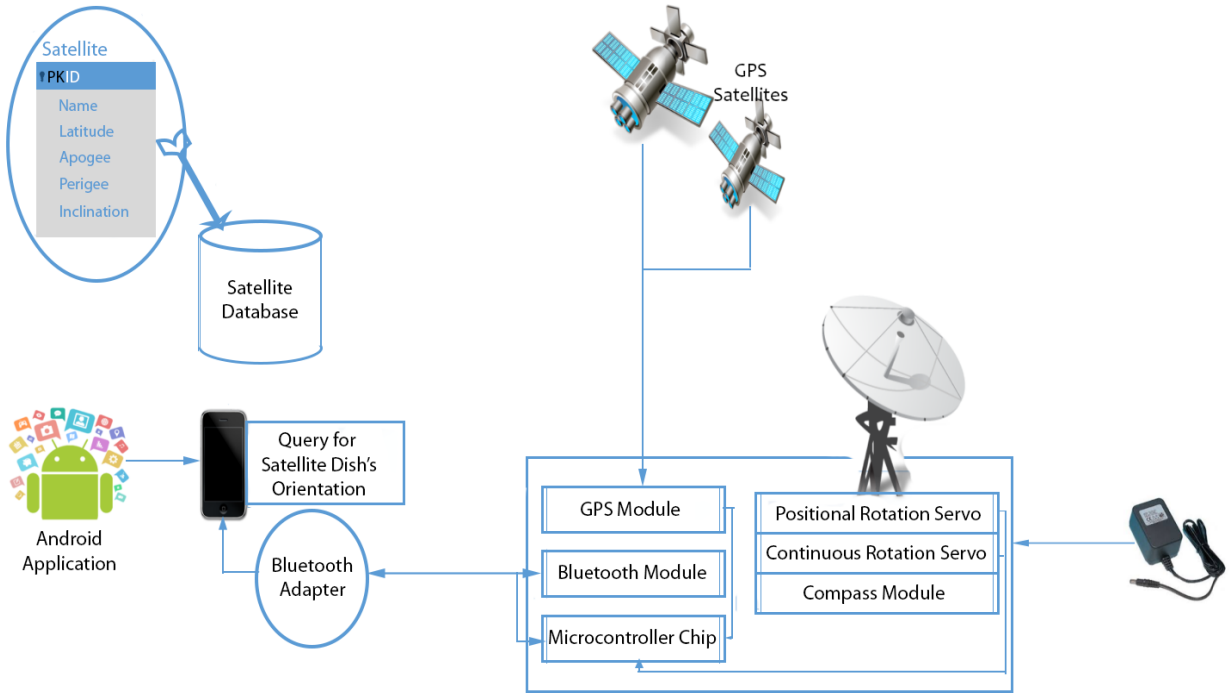

Fig. 1: System Design and Architecture

The overall system design and architecture is depicted in Figure 1 and shows the various developed hardware and software modules and their corresponding integration. It consists of an Android application running on a smartphone equipped with the Bluetooth adapter which interfaces with the hardware modules (Positional Rotation Servo, Continuous Rotation Servo and Compass)

System Modules

Android User Interface

The Android Application provides the interface by which users of the satellite dish interact with the dish. With Bluetooth technology, the application needs to access the Bluetooth adapter of the Android device, scan for available devices and allow pairing and a connection to occur on request. If the user is authorized to access the Bluetooth module of the dish, he/she will be allowed to activate an 'auto-orient' feature, whereby a satellite source will be chosen from a database for the system to automatically position itself. The user will also be allowed to change the orientation of the dish along its vertical and horizontal axes by pressing directional buttons corresponding to their respective commands.

The Android application has the following requirements:

1. Application should have a perceptive user interface.
2. Application should allow users to search for available Bluetooth devices, select their preferred device's corresponding module identity (satellite dish's Bluetooth module) and connect to it.
3. Users should go through an authorization stage where a password is verified for security reasons

before access to the control features of the application is granted.

4. Users should be able to align the dish to left, right, upward or downward positions using directional buttons.
5. Users should be able to select a preferred satellite from a list of satellites available in the application.
6. Users should be able to command the dish to position itself automatically through the application.
7. The flowchart for the operation of the Android application is depicted in Figure 2 (A).

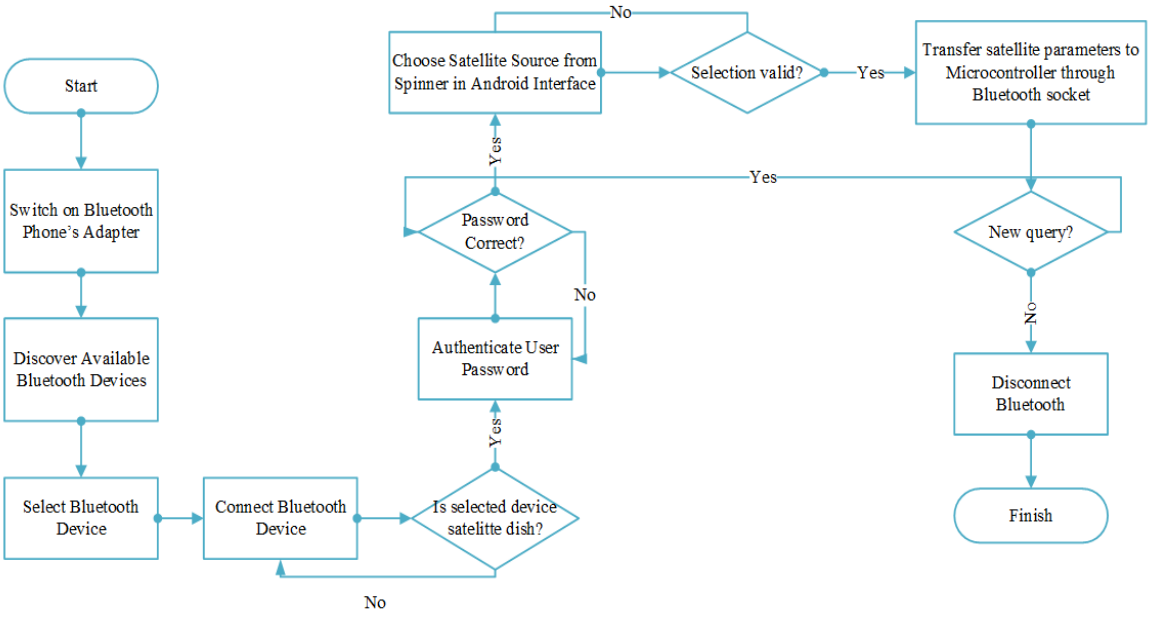

Fig. 2: A) Operation of Android Application

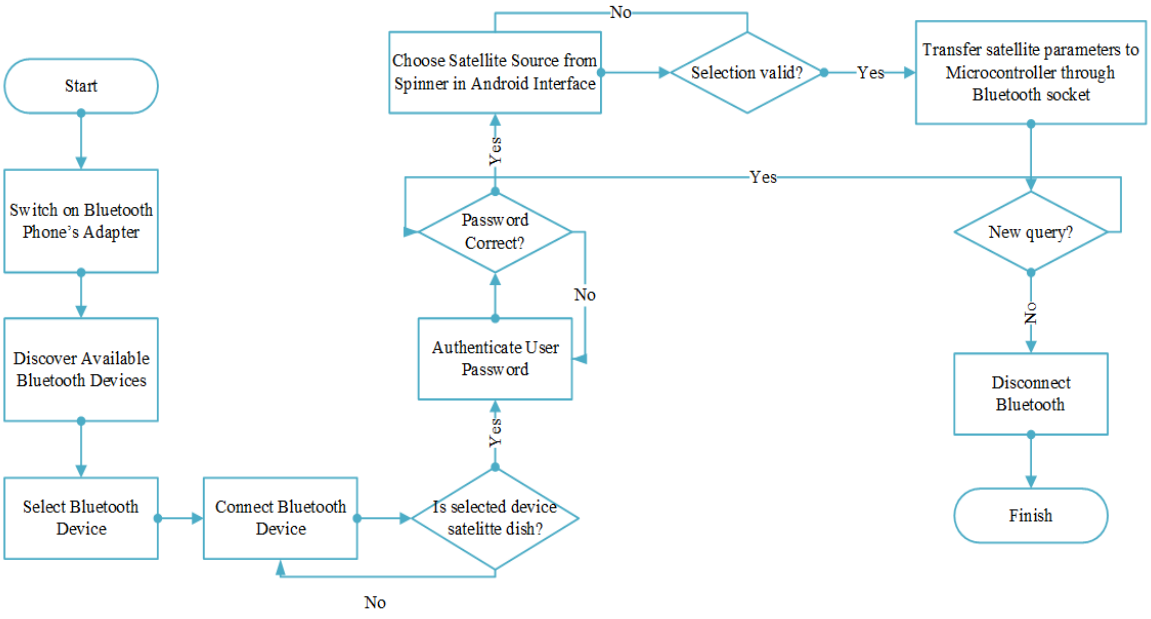

Fig. 2: B) Operation of Satellite Mount System

Satellite Database

The database is a predefined one and contains two tables: *sqlite_sequence* and *satellite Info*. The *sqlite_sequence* is an automatically generated table within the database which is used to implement the automatic increment functionality of the *satelliteInfo* ID attribute. The *satelliteInfo* table contains information such as the satellite's name, perigee, apogee, longitude and inclination. Upon selecting a desired satellite from a spinner in the developed Android interface, an activity is launched to ensure that the satellite information selected is retrieved from the database and then used to compute the corresponding elevation and azimuth of the satellite receiver dish for auto alignment.

Satellite Dish Mount System

The power supply unit is the essential subsystem which provides power to the various components of the entire system: the microcontroller, servos, GPS device, Bluetooth and compass modules. With the exception of the Bluetooth and compass modules which needed 3.3V, all other components and the microcontroller needed an average of 5V direct current supply.

The requirements of the subsystem comprising the mount are:

1. System should allow communication with the user by allowing an open and dedicated connection.
2. System should receive positional commands from the user and effect them with the help of the corresponding actuators.
3. System should compute and readily present GPS coordinates for computation at any given time.
4. System should provide the compass heading with respect to the earth's magnetic north to enable tracking of the azimuth of the satellite dish receiver.
5. The flowchart for the operation of the Satellite Mount module is depicted in Figure 2(B).

The microcontroller is the unit containing all the information that controls all the hardware components which are interfaced with it. The positional rotation

servo is used to alter the elevation of the dish whilst the continuous rotation servo is used to allow change in azimuth of the dish. The Bluetooth module is responsible for the communication between the Android application and the dish where the commands are sent from the device and received by the module, then transferred serially to the microcontroller to effect corresponding commands.

The compass and GPS module are especially responsible for the auto-orientation functionality of the system. The compass is responsible for providing the heading information for the dish, allowing it to keep track of its azimuth in relation to the earth's magnetic north pole. The GPS module provides the position coordinates of the dish's location which are used to compute the elevation and azimuth of the dish with respect to that position. The SkyNav SKM53 Series was the preferred choice because of its capabilities in harsh GPS visibility environments and a tracking sensitivity of –165 dBm, which give it a wide extension of position coverage. It is also proficient in environments of temperature ranging from 40 to 85°C. Bluetooth modules come in a variety of classes - 1, 2 and 3 - which determine their range of operation. The class 1 Bluetooth module allows communication with other Bluetooth devices within a radius of 100m, which is the maximum area for Bluetooth devices. The HC-05 Bluetooth module was employed because of the wider range it provided at a cheaper cost. The HMC6352 compass module has multiple operating modes that balance the use of power with query acquisitions and rapid heading updates.

The scope of the system required a 2-dimensional rotation in the vertical and horizontal axes. This demanded that two different motors be utilized. The elevation angle was required to be controllable from 0° to 90° and the azimuth controllable from 0° to 360°. Continuous rotation servos do not provide feedback to the system; nonetheless, they allow a maximum degree of rotation about the pivot. Positional rotation servos allow rotation from 0° to 180° with feedback to the system, which is a much preferable option for control systems. Since elevation positioning did not require a full range of operation, a positional rotation servo was required for that functionality, with limited motion within a 90° range and a continuous rotation servo for the azimuth positioning functionality. The HS-133 and the HSR1425-CR which are positional and continuous rotation servos respectively were selected.

System Design

A flow diagram showing the operation of the system is shown below:

A flow diagram showing the overall operation of the system is shown below in Figure 3. When the system starts, it selects the satellite Bluetooth device and connects it. Querying the satellite dish for new satellite position and aligning them to user's specified choices and customizations. After that operation, it finishes the setup and waits for new user preferences by going through the same cyle.

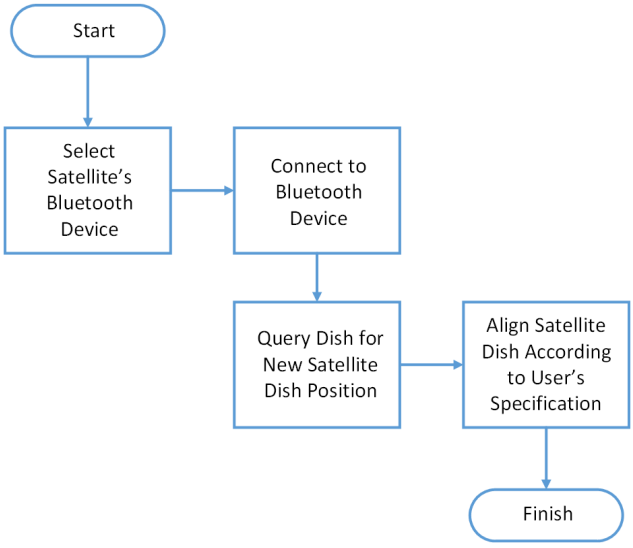

Fig. 3: Flow Chart for System Operation

System Implementation and Testing

The implementation of the system involved the development of the Android application, creating and populating the database containing satellite information, building the power supply, programming of individual components and the integration and testing of the entire system, the components of which are taken singly as incremental modules. The various implementation processes of the subsystems comprising the overall system are discussed in the following subsections.

Android Application Development

The layout interface of an Android application was defined in an XML file instead of the particular *.java* file implementing that activity. This was done to make it more manageable. The function of the main activity of the application is to allow a connection to other classes within the Android project. To enable discovery of available Bluetooth devices, a class within the Android project is first called with the option given for a user to choose one of the devices to connect to. This activity automatically checks the state of the Bluetooth adapter on the device. If the device does not have a Bluetooth adapter, it means that the application cannot locate and control other Bluetooth devices and the application closes; otherwise, the Bluetooth adapter is automatically switched on and allowed to discover other Bluetooth devices in its radius of view. On selection of an available Bluetooth device, its name, its MAC address and bond status are saved. With the MAC address' correspondence with the satellite dish's Bluetooth module, authentication of user's access is made by means of a password before adjustment functionality of the dish is allowed. A *.java* class is responsible for the mutator (setter) and accessor (getter) methods of the satellite parameters from the database. The mutator method is used to set the values of the records in the database during insertion at the initialization of the application and the accessor method is used to retrieve queried records. The developed interface for system user authentication and the Android's application activity control is shown in Fig. 4A and 4B below.

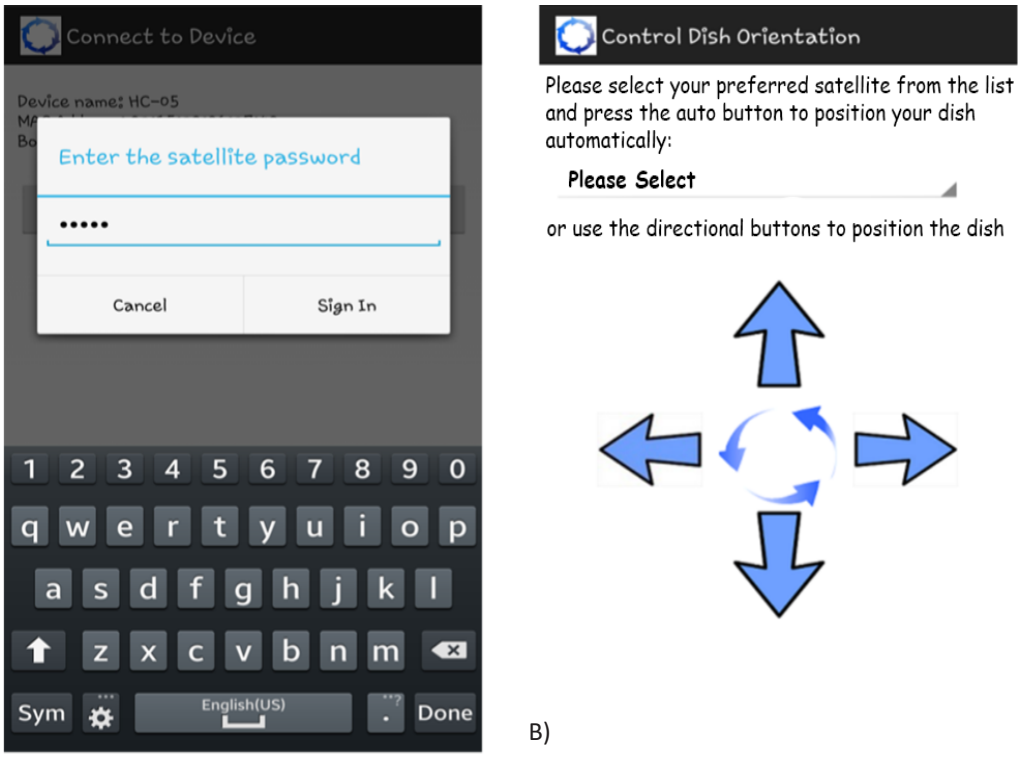

Fig. 4: A) User Authentication Dialog Interface and B) Android's Application Control Activity

Development of Satellite Database in SQLite

Creating and using databases in Android involves one of two approaches: dynamically creating the database at runtime or having a predefined database with data already stored in it. The first approach is of great use in applications that involve storing data for applications which could be constantly updated by a user. The second approach is essential when the data to be used in the application is known and of a large size, which might otherwise slow down the application in case of access of data items from the database, were the earlier approach used. Since the database of satellite information required numerous records which had predefined parameters, the second option was brilliant. The *SQLite*Database created was moved to the assets folder of the Android project which copies it into the system database path of the application. The *SQLiteDatabase* API then opens and accesses it normally.

Calculation of Elevation and Azimuth Angles

The angles for the elevation and azimuth of any satellite dish receiver are dependent on the geographical coordinates and altitude of the dish relative to that of the satellite in terms of its sub-satellite point and height. In the computation of the angle of elevation of the satellite dish in relation to the satellite in focus, triangular trigonometry was used. The assumption made was that the earth is a perfect sphere with an origin (0,0,0) and an even radius, R=6371000 m.

For the computation of distance *d*, the user coordinates and sub-satellite points are converted to Cartesian

coordinates *(x,y,z)* and the straight line distance (SLD) computed between them for the calculation of angle *e* from the triangle obtained.

Assuming the sub-satellite point position, $pos(\theta_1,\emptyset_1)$ and the coordinates of the user position, $pos(\theta_2,\emptyset_2)$,

$$xpos_1 = R\cos(\theta_1)\cos(\emptyset_1) \quad (1)$$

$$ypos_1 = R\cos(\theta_1)\sin(\emptyset_1) \quad (2)$$

$$zpos_1 = R\sin(\theta_1) \quad (3)$$

Similarly,

$$xpos_2 = R\cos(\theta_2)\cos(\emptyset_2) \quad (4)$$

$$ypos_2 = R\cos(\theta_2)\sin(\emptyset_2) \quad (5)$$

$$zpos_2 = R\sin(\theta_2) \quad (6)$$

The SLD between them is computed as

$$SLD = \sqrt{(x_{pos_1} - x_{pos_2})^2 + (y_{pos_1} - y_{pos_2})^2 + (z_{pos_1} - z_{pos_2})^2} \quad (7)$$

$$where -90° \le \theta \le 90° (latitude)$$
$$and \quad 0 \le \emptyset \le 360\ (longitude)$$

With the SLD computed, the cosine rule is again used to find the angle *e*, which is employed to find the angle *r*.

From the cosine triangle,

$$(R + h_s)^2 = (R + h_a)^2 + d^2 - 2(R + h_a)(d)\cos(r) \quad (10)$$

$$r = \cos^{-1}\left(\frac{(R + h_a)^2 + d^2 - (R + h_a)^2}{2(R + h_a)(d)}\right) \quad (11)$$

$$ElevationAngle = r - 90°$$
$$whereR = Radius\ of\ the\ Earth$$
$$h_a = Altitude\ of\ satellite\ dish$$
$$h_s = Altitude\ of\ satellite$$

From spherical trigonometry, with a spherical triangle drawn on the surface of the earth;

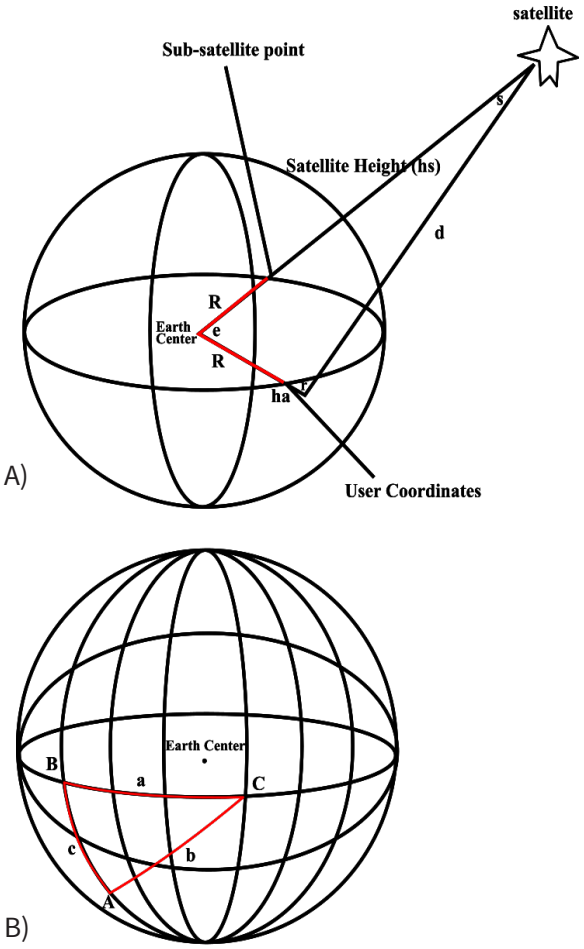

Fig. 5: Calculation of A) Azimuth and B) Elevation Angle

Azimuth refers to the rotation of the whole antenna around a vertical axis.

From the laws of cosines,

$$\cos(b) = \cos(a)\cos(c) + \sin(a)\sin(c)\cos(B) \quad (12)$$
$$where\ B = lon_2 - lon_1$$
$$and\ c = 90° - lat_1$$
$$and\ a = 90° - lat_2$$
$$b = \cos^{-1}(\cos(a)\cos(c) + \sin(a)\sin(c)\cos(B))$$

From the sine rule,

$$\frac{\sin(A)}{a} = \frac{\sin(B)}{b} = \frac{\sin(C)}{c} \quad (13)$$
$$\Rightarrow A = \sin^{-1}(a\frac{\sin(B)}{b})$$

Programming of Individual Hardware Components

The Bluetooth module was first set in AT mode to configure some modifications to selected default properties of the module, such as its name, for easy identification by the satellite dish receiver and a baud rate of 9600 for communication with the microcontroller. It was then programmed to receive ASCII characters from the Bluetooth device of the Android mobile. Available ASCII were now converted to characters in the microcontroller with *switch()* statements implementing their respective conditions where 'a' meant an automatic positioning, '*u*' referred to an upward signal, '*d*' to a downward signal, '*l*' to movement in the left direction and '*r*' to movement towards the right. Since the microcontroller received characters from the Bluetooth socket of the mobile device serially, there was the need for concatenation and then conversion into floating point variables corresponding to the height and longitudes of selected satellites.

With the positional servos, the shaft producing the output rotates 180º both clockwise and anti-clockwise, with stops placed in the gear mechanism to prevent turning beyond these limits. Given their limited range of rotation, it was preferred that they be used in the control of the elevation of the satellite dish. The servo was programmed to respond to the commands corresponding to upwards and downwards movements. In cases where the maximum elevation is reached, the servo motor does not respond to upward commands; the same applies to downward commands for minimum elevation.

Since continuous rotation servos allow rotation in either direction indefinitely, they were the preferred choice for rotation along the horizontal axis. With continuous rotation servos, the control signal sets the speed and direction of the servo— either clockwise or anticlockwise— rather than its position. When positional rotation servos are instructed to move, they will move to the position and hold it. The *servo.writeMicroseconds()* function was used to control the servo by pulse width modulation (PWM). A value greater than 1500 allowed the servo to move in the clockwise direction whilst a value less than that allowed the servo to be moved in the opposite direction. With 1500 in the function, the servo's neutral position is achieved. A delay was introduced after each movement to determine the duration of the pulse, determining the angle of rotation. Since continuous rotation servos do not have feedback control, a count variable was used to keep track of the azimuth of the dish, which had a maximum value of 359 and a minimum of 0 with a modulus operand.

The GPS module was required to provide the microcontroller with three parameters for the computation of the dish's azimuth and elevation - the latitude, longitude and height of the dish. Due to the limited capability of the ports of Arduino Mega to support interrupts, only specific ports had the capacity to perform serial reception of data. The TX and RX pins of the GPS module were therefore assigned to ports 51 and 53 of the Arduino board respectively. The GPS module was assigned a baud rate of 9600. Functions defined in the *TinyGPS* header were used in the code to obtain the current latitude, longitude and altitude of the dish.

The compass module had the basic task of tracking the heading of the satellite dish in relation to the Earth's magnetic north. It was required that the RX and TX pins of the compass module be connected to the data (SDA) and clock (SCL) lines (20 and 21 respectively) of the Arduino board.

Hardware and System Integration

With the testing of the functionalities of the individual components completed, it was useful to integrate the individual components to form the hardware subsystem.

Embedded Unit Circuitry Test

The testing of the unit circuitry was done to ensure that it met the voltage and current requirements of each component and the entire unit. Supplying a lesser voltage will cause certain components of the system not to respond to certain query signals. With the 5V 65mA power requirement not met, GPS transmission was not possible. The compass demanded voltage levels between 2.7 and 5.2 V. The Bluetooth module ideally demanded voltage of 3.3V but had allowance and worked normally up to 6V. The microcontroller board requires a voltage of 5V, while there was the possibility of frying the chip with voltages in excess of that. The unit employed a power circuit which rectified the 220V AC supply to ~11.7V DC. Due to power fluctuations during the testing phase, a 5V DC regulator was employed to create the expectation that the output of the DC regulator will always be in the region of 5V. Tests conducted produced the same voltage at the output of the DC regulator.

System Testing and Results

Once the hardware integration and power requirements tests were complete, it was necessary to test the entire hardware system with the Android application. The Android application was installed and started on a Samsung Galaxy Note 3 SM-N9005 which required user authorization for the application to access and turn on the system's Bluetooth adapter (if previously off) and begin discovery of available Bluetooth devices. On selection of the satellite dish's Bluetooth device from the list, the option was given for pairing and connecting to it with a successful authentication. A blank field or wrong password entry presented an alert and prevented further use of the application by the user till a correct entry was made. With approved credentials, access was gained to the Android activity that allowed the control of the satellite dish receiver.

The directional buttons were first tested to ensure their correspondence to the various directions they represented. In the initialization state, the elevation of the dish is set to 0° - in parallel with the horizontal, with no response to input indicating further movement downwards. The button with an arrow moving upwards produced a corresponding shift in position, increasing the elevation from its original position to a maximum elevation angle of 90°. The buttons which issued commands to allow for clockwise and anticlockwise rotation allowed unlimited change in azimuth angles in both directions.

When the auto-rotation functionality of the application was triggered without the selection of any satellite source, a prompt issued an alert that a broadcasting source be selected for that feature to execute. Various satellite sources were selected for the auto-rotation functionality of the application to transmit satellite information to the microcontroller for computation and allow orientation of the dish in computed values of azimuth and elevation. The main aim of this test is to measure the difference in the values obtained from the system azimuth and elevation calculations and alignment in contrast to the expected values. The automatic alignment process involves the following stages: parameters of satellite selected by user are received by Bluetooth module and sent to microcontroller; microcontroller performs computation for azimuth and elevation and rounds it off to the nearest integer; system positions itself in accordance to resulting computation as shown in Figure 6. Since the servo motors only allowed rotational changes with no decimal places, there was a little allowance for error.

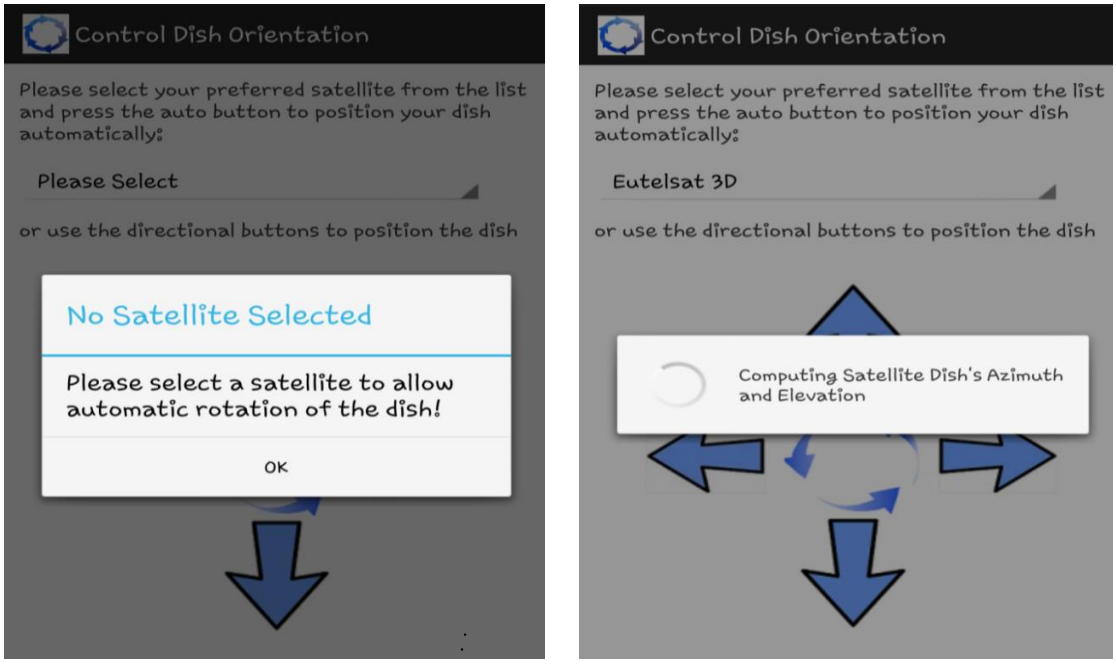

Fig. 6: Results of Android interface testing for satellite dish positioning system

Table 1: Comparison between Expected and System's Azimuth and Elevation for 7 different satellites

Expected Azimuth	265.41	102.64	138.43	101.31	108.72	100.19	112.78
System's Azimuth	264	102	138	102	108	100	112
Expected Elevation	31.58	61.57	81.14	58.76	69.91	55.96	73.17
System's Elevation	32	62	81	59	70	56	73

Table 1 above shows the results of tests with 7 satellites selected showed an error margin ranging from -0.0068% to 0.00692%, which is satisfactory as satellite dish receivers will maintain a line of sight communication with sources from the computation. Satellites sources not in the range of view of the satellite dish were also selected for testing with a negative response from the system.

Conclusion

The design procedures for both the hardware and software components were realized. The developed system was successfully tested and deployed. After successful completion of this research and subsequent deployment, the following benefits are realized by users of the system: (1) ease of control of system (2) remote control of system (3) automatic alignment for line of sight communication with satellite source.

Acknowledgements

The authors would like to acknowledge the technical and nurturing environment provided by the staff and faculty of the Department of Computer Engineering, University of Ghana.

References

A Look at the Basics of Bluetooth Technology. (2015, April 12). BluetoothFacts. Retrieved from https://www.bluetooth.com/Pages/Basics.aspx

Adewusi A. A., (2000, May). *Wireless communication: Today's Need Tomorrow's Promise*. Paper presented at the meeting of Electrotechnical Conference, Lemesos

Cheruku, D. (2010). *Satellite communication*. New Delhi: I.K. International Publishing House.

Dutta, P. (2015). *What Are the Advantages of Wireless Communication? | eHow. eHow*. Retrieved 11 April 2015, from http://www.ehow.com/facts_4885908_what-advantages-wireless-communication.html

Fast Facts. FastFacts. (2015). Retrieved 12 April 2015, from https://www.bluetooth.com/Pages/Fast-Facts.aspx

Franklin, C. & Layton, J. (2000). *How Bluetooth Works. HowStuffWorks*. Retrieved 26 March 2015, from http://electronics.howstuffworks.com/bluetooth.htm

Galactics. (2016). *Satellite antenna bearing calculator. Giangrandi.ch*. Retrieved 22 April 2015, from http://www.giangrandi.ch/electronics/satcalc/satcalc.shtml

Ha, T. (1986). *Digital satellite communications*. New York: Macmillan Publishers.

Jackson, W. (2011). *Android apps for absolute beginners*. [Berkeley, California.]: Apress Publishers.

Me, O., Chaw, N., & Hla, T. (2006). Satellite Dish Positioning Control by DC Motor Using IR Remote Control. *International Journal of Electronics and Computer Science Engineering*, 3, 119-207.

Nice, K. & Harris, T. (2002). *How Satellite TV Works. HowStuffWorks*. Retrieved 21 October 2014, from http://electronics.howstuffworks.com/satellite-tv.htm

Rafael, C., Gonçalves, B., & Leite do Prado, P. (2012). *Development of an Automated System for Maneuvering Parabolic Dish Antennas Used in Satellite Communication*. Paper presented at the meeting of ABCM Symposium Series in Mechatronics, 5, 69-78.

Rappaport, T.S. (2002). *Wireless Communications: Principles and Practice, Edition 2. Upper Saddle River, New Jersey. Prentice Hall Publisher.*

Satellites - Attitude Control: Overview. (2016). *Satellites. spacesim.org*. Retrieved 26 March 2015, from http://satellites.spacesim.org/english/anatomy/attitude/index.html

Satellite Communication. (2007). Retrieved 17 December 2014, from http://www.scatmag.com/technical/Satellite%20Communication_aug07.pdf

Sairam, K., Gunasekaran, N., & Redd, S. (2002). Bluetooth in Wireless Communication. *IEEE Communications Magazine*, (6), 90-96.

Tatum, M. (2016). *What are Wired Communications? (with pictures). wiseGEEK*. Retrieved 11 April 2015, from http://www.wisegeek.com/what-are-wired-communications.htm

Voormansik, K. (2009). *Satellite Signal Strength Measurements with the International Space University Ground Station and the University of Tartu Ground Station* (Master's Thesis). University of Tartu, Faculty of Science and Technology, Institute of Physics.

Wilkinson, M., & Swenson, C. (1999). *Design of a Satellite Tracking Station for Remote Operation and Multi-User Observation*. Paper presented at the meeting of 13th Annual AIAA/USU Conference on Small Satellites, IIb, 1-16.-

INSTRUCTION FOR AUTHORS

SCOPE

Science and Development – *the Journal of Basic and Applied Science* will publish original research articles, reviews and short communications in all scientific fields spanning agricultural, biological, engineering and physical sciences, with strong emphasis on promoting the link between science and development agenda. The journal aims to publish high quality articles rapidly and make these freely available to researchers world-wide through an open access policy.

Instructions to authors for submission of Research Article

On submission, authors will be required to agree to the Author's Declaration confirming that:

- the work as submitted has not been published or accepted for publication, nor is being considered for publication elsewhere, either in whole or substantial part.
- the work is original and all necessary acknowledgements have been made.
- all authors have read the submitted version of the manuscript and approve its submission.
- all persons entitled to authorship have been so included.

Title page

The title page should:

- present a concise title that captures the essence of the work presented;
- list the full names, institutional addresses and email addresses for all authors;
- indicate the corresponding author.

Abstract

The abstract should not exceed 300 words. The use of abbreviations should be minimized and do not cite references in the abstract. The abstract must provide context and purpose of the study, brief description of methods used and study area (where relevant), the main findings and brief summary and potential implications.

Keywords

Five to eight keywords representing the main content of the article.

MAIN PAPER

Introduction

The introduction should explain the background to the study, its aims, a summary of the existing literature and why this study was necessary.

Methods

The methods section should include sampling, experimental design and setting of the study, a clear description of all analytical and experimental methods, processes, interventions and the type of statistical analysis used. When proprietary brands are used in research, include the brand names in parentheses.

Results

This should comprise the findings of the study including, if appropriate, results of statistical analysis which must be included either in the text or as Tables and Figures.

Discussion

For research articles, this section should discuss the implications of the findings in context of existing research and highlight limitations of the study. For study protocols and methodology manuscripts, this section should include a discussion of any practical or operational issues involved in performing the study and any issues not covered in other sections

Conclusions

This should state clearly the main conclusions and provide an explanation of the importance and relevance of the study to the field.

Sections numbering

You may number the various sections/sub-sections of your article (excluding the abstract) using the format: 1, 2.. (then 1.1, 1.2; 1.1.1, 1.1.2, ...) etc. The subsections may be given a brief heading, with each heading appearing on a separate line.

Presentation

Font, Times New Roman, 11; 1.5 spacing, maximum of 15 pages (including References but excluding Figures and Tables).

Declarations (if any)

List of abbreviations

If abbreviations are used in the text they should be defined in the text at first use.

Ethics approval and consent to participate

Manuscripts reporting studies involving human participants, human data, human tissue or animals, must:

- include a statement on ethics approval (even where the need for approval was waived) and consent (in case of human subjects);
- include the name of the ethics committee that approved the study and the committee's reference number if appropriate.

Referencing

The APA (American Psychological Association) references style must be used. For detailed information, please see the Publication Manual of the American Psychological Association, 6th edition, http://www.apastyle.org/ and http://blog.apastyle.org/. or the Taylor and Francis Summary given here. http://www.tandf.co.uk/journals/authors/style/reference/tf_APA.pdf

Preparing figures

When preparing figures, please follow the formatting instructions below.

- Figures should be provided as separate files, not embedded in the main manuscript file (maximum five figures).
- Each figure of a manuscript should be submitted as a single file that fits on a single page in portrait format. Each figure should be closely cropped to minimize the amount of white space surrounding the illustration.
- Multi-panel figures (those with parts a, b, c, d etc.) should be submitted as a single composite file that contains all parts of the figure.
- Figures should be numbered in the order they are first mentioned in the text, and uploaded in this order.
- Figures should be uploaded in the correct orientation.
- Figure titles (max 15 words) and legends (max 150 words) should be provided in the main manuscript, not in the graphic file.
- Figure keys should be incorporated into the graphic, not into the legend of the figure.
- Individual figure files should not exceed 10 MB. If a suitable format is chosen, this file size is adequate for extremely high quality figures.
- **Please note that it is the responsibility of the author(s) to obtain permission from the copyright holder to reproduce figures (or tables) that have previously been published elsewhere.** In order for all figures to be open access, authors must have permission from the rights holder if they wish to include images that have been published elsewhere in non open access journals. Permission should be indicated in the figure legend, and the original source included in the reference list.

Figure file types

We accept the following file formats for figures:

- PDF (suitable for diagrams and/or images)
- Microsoft Word (suitable for diagrams and/or images)
- PowerPoint (suitable for diagrams and/or images, figures must be a single page)
- TIFF (suitable for images)
- JPEG (suitable for photographic images, less suitable for graphical images)
- PNG (suitable for images)
- BMP (suitable for images)
- CDX (ChemDraw - suitable for molecular structures)

Figure size and resolution

Figures are resized during publication detailed below.

Figures on the web:

- width of 600 pixels (standard), 1200 pixels (high resolution).

Figures in the final PDF version:

- width of 85 mm for half page width figure
- width of 170 mm for full page width figure
- maximum height of 225 mm for figure and legend
- image resolution of approximately 300 dpi (dots per inch) at the final size

Figures should be designed such that all information, including text, is legible at these dimensions. All lines should be wider than 0.25 pt when constrained to standard figure widths. All fonts must be embedded.

Preparing Tables

When preparing Tables, please follow the formatting instructions below.

- Tables should be numbered and cited in the text in sequence using Arabic numerals (i.e. Table 1, Table 2 etc.).
- Larger datasets, or tables too wide for A4 or Letter landscape page can be uploaded as additional files.
- Table titles (max 15 words) should be included above the table, and legends (max 150 words) should be included underneath the table.
- Tables should not be embedded as figures or spreadsheet files, but should be formatted using
- 'Table object' function in your word processing program.
- Tables should NOT be submitted as figures but should be included in the main manuscript file
- Colour and shading may not be used in tables. Parts of the table can be highlighted using superscript, numbering, lettering, symbols or bold text, the meaning of which should be explained in a table legend.
- Commas should not be used to indicate numerical values.

BIOLOGICAL SCIENCES

PHYSICAL SCIENCES

CBAS
College of Basic and Applied Sciences
University of Ghana

DigiBooks

ISSN 2550-3421